UNIVERSITEIT VAN PRETORIA
UNIVERSITY OF PRETORIA
YUNIBESITHI YA PRETORIA

VIBRATION EFFECTS ON NATURAL CONVECTION IN A POROUS LAYER HEATED FROM BELOW WITH APPLICATION TO SOLIDIFICATION OF BINARY ALLOYS

by

Johnathan John Vadasz

Submitted in partial fulfilment of the requirements for the degree

PHILOSOPHIAE DOCTOR (Mechanical Engineering)

in the

Faculty of Engineering, the Built Environment and Information Technology

UNIVERSITY OF PRETORIA

Pretoria

Supervisor: **Professor Josua P. Meyer**

Co-Supervisor: **Dr Saneshan Govender**

2014

© University of Pretoria

ABSTRACT

Title: **Vibration effects on Natural convection in a porous layer heated from below with application to solidification of binary alloys**

Author: **Johnathan John Vadasz**

Supervisor: **Professor Josua P. Meyer**

Co-Supervisor: **Dr. Saneshan Govender**

Department: **Mechanical and Aeronautical Engineering**

University: **University of Pretoria**

Degree: **Philosophiae Doctor (Mechanical Engineering)**

Directional solidification has a wide interest due to its importance to the iron and steel industry. Examples of further application can be found in the aerospace industry regarding the manufacture of turbine blades and the semiconductor industry regarding single-crystal growth applications. Solute convection in the solidification process results in channel formation, which has a freckle-like appearance in cross-section and has a critical effect on the mechanical strength of a casting. For a solidification process that occurs via planar solidification from a solid boundary, one may consider the presence of three distinct regions often identified as horizontal layers, i.e. a fluid binary mixture (the melt), the solid layer and a two-phase (fluid-solid) mushy layer, separating the other two. The mushy layer is practically a porous medium consisting of an interconnected solid phase having its voids filled with the melt binary fluid. Channelling in the mushy layer and the creating of freckles are being considered the main reasons for non-homogeneous solidification and production of defects in the resulting solid product. The production of defects adversely affects the mechanical properties of the solid product leading to undesirable constraints on its industrial use.

The purpose of this study is to evaluate the effect the vibrations have on the heat transfer during the solidification process as well as on the average density of the solid product and void formation. Experimental as well as theoretical investigations related to the solidification process were undertaken.

© University of Pretoria

Two effects that have been observed in previous experimental studies when metals and metal alloys are vibrated during solidification are a decrease in dendritic spacing, which directly affects density, and faster cooling rates and associated solidification times. Because these two effects happen simultaneously during solidification it is challenging to determine the one effect independently from the other. Most previous studies were on metals and metal alloys. In these studies, the one effect, i.e. the decrease in dendritic spacing, might influence the other, i.e. the faster cooling rates, and vice versa. The direct link between vibration and heat transfer has not yet been studied independently. The purpose of this study was to experimentally investigate the effect of vibration only on heat transfer and thus solidification rate. Experiments were conducted on paraffin wax, because it had a clearly defined macroscopic crystal structure consisting of mostly large straight-chain hydrocarbons. The advantage of the large straight-chain hydrocarbons was that the dendritic spacing was not affected by the cooling rate. Experiments were done with paraffin wax inside hollow plastic spheres of 40 mm diameter with 1 mm wall thickness. The paraffin wax was initially in a liquid state at a uniform temperature of 60°C and then submerged into a thermal bath at a uniform constant temperature of 15°C, which was approximately 20°C below the mean solidification temperature of the wax. Experiments were conducted in approximately 300 samples, with and without vibration at frequencies varying from 10 – 300 Hz. The first set of experiments were conducted to determine the solidification times. In the second set of experiments, the mass of wax solidified was determined at discrete time steps, with and without vibration. The results showed that paraffin wax had vibration independent of solid density contrary to other materials, eg. metals and metal alloys. Enhancement of heat transfer resulted in quicker solidification times and possible control over the heat transfer rate. The increase in heat transfer leading to faster solidifcation times was observed to first occur, as frequency increased and then to decrease.

Experimental results showed that paraffin wax had vibration independent of solid density contrary to other materials, eg. metals and metal alloys. Enhancement of heat transfer resulted in quicker solidification times and possible control over the heat transfer rate. The increase in heat transfer leading to faster solidifcation times was observed to first occur, as frequency increased and then to decrease. Theoretical results of heat convection

© University of Pretoria

in a porous layer heated from below and subject to vibrations are presented by using a truncated spectral method in space. The partial differential equations governing the mass, momentum, heat, and solute transport were tranformed into a set of ordinary differential equations via a truncated modal expansion. Then the resutling equations were solved to identify the variety of regimes, and transitionbetween them, i.e. from steady convection, via periodic and quasi-periodic convection, towards chaotic or weak turbulent convection. The theoretcial results show that the heat convection subject to vibration is generally reduced when compared with the corresponding convection without vibrations. The exception for a certain frequency range shows about a 10% enhancement in the weak turbulent regime of convection, however, a 10% enhancement is still lower than the heat transfer prior to the transition to weak turbulence. Therefore, the heat transfer mechanism can be excluded as the main reason behind the improvement in solidification when vibrations are applied. Both experimental and theoretical results show an enhancement in heat transfer which correlate qualitatively.

KEYWORDS: *vibration, solidification, mushy layer, porous media, natural convection.*

© University of Pretoria

Acknowledgements

I would like to thank *Professor Josua Meyer* as my supervisor for his support with conference attendance and experimental work funding as well as constant guidance with journal and conference publications. I would also like to thank *Professor Saneshan Govender* as my co-supervisor for assistance in my PhD thesis research. Specifically for supplying me with some Journal paper publications and other relevant literature to my research. I would like to thank Prof. G. Ziskind and Prof. A. Levi whom had a lot of input with the experimental part and supplied the equipment and facilities.

© University of Pretoria

Publications in Journals and Conferences

Articles in refereed journals

1. VADASZ, J.J., MEYER, J.P., GOVENDER, S.: "*Vibration effects on weak turbulent natural convection in a porous layer heated from below*", *International Communications in Heat and Mass Transfer,* **Vol 45**, pp. 100-110, 2013.
2. VADASZ, J.J., MEYER, J.P., GOVENDER, S.: "*Chaotic and Periodic Natural Convection for Moderate and High Prandtl Numbers in a Porous Layer subject to Vibrations*", *Transport in Porous Media Journal*, **Vol 103, issue 2,** pp. 279-294, 2014.
3. VADASZ, J.J., MEYER, J.P., GOVENDER, S., ZISKIND, G.: "*Heat Transfer Enhancements using Vibration during Solidification of Paraffin*", *Manuscript UEHT-2014-0072*, *Experimental Heat Transfer Journal,* accepted 11 September 2014.

Articles in refereed international conference proceedings

1. VADASZ, J.J., MEYER, J.P., GOVENDER, S., ANDRICK M., CARTER W., EBRAHIM H., NAIDOO A., NGUBANE I., OGLE M.: "Experimental evidence of density and mechanical properties enhancements of binary alloys by solidification subject to vibrations". *Proceedings of the 6th HEFAT international conference, heat transfer, fluid dynamics and thermodynamics*, Pretoria, South Africa, June 30 – July 2, 2008.
2. VADASZ, J.J., MEYER, J.P., GOVENDER, S., ANDRICK, M., CARTER, W., EBRAHIM, H., NAIDOO, A., NGUBANE, I., OGLE, M.: "Experimental evidence of density and mechanical properties enhancements of binary alloys by solidification subject to vibration". *Proceedings of the IMECE 2008 ASME international mechanical engineering congress and exposition,* Boston, MA, USA, November 2-6, 2008.
3. VADASZ, J.J., MEYER, J.P., GOVENDER, S., ANDRICK, M., CARTER, W., EBRAHIM, H., NAIDOO, A., NGUBANE, I., OGLE, M.: "Experimental evidence of density and mechanical properties enhancements of binary alloys by solidification subject to vibration". *Proceedings of the Summer Heat Transfer 2009 ASME conference,* San Fransisco, CA, USA, July 19-23, 2009.
4. VADASZ, J.J., MEYER, J.P., GOVENDER, S.: "Heat transfer enhancements using vibration during solidification of paraffin". *Proceedings of the 14th international heat transfer conference*, Washington, DC, USA, August 8-13, 2010.

© University of Pretoria

5. VADASZ, J.J., MEYER, J.P., GOVENDER, S., ZISKIND, G.: "Vibration effects on heat transfer during solidification of paraffin" *Proceedings of the ASME 2011 International Mechanical Engineering Congress and Exposition*, Denver, CO, USA, November 11-17, 2011.
6. VADASZ, J.J., MEYER, J.P., GOVENDER, S., ZISKIND, G.: "Vibration effects on heat transfer during solidification of paraffin" *Proceedings the 9th HEFAT international conference, heat transfer, fluid dynamics and thermodynamics*, Malta, July 16 – 18, 2012.

© University of Pretoria

UNIVERSITEIT VAN PRETORIA
UNIVERSITY OF PRETORIA
YUNIBESITHI YA PRETORIA

TABLE OF CONTENTS

	page
ABSTRACT	i
ACKNOWLEDGEMENTS	iv
PUBLICATIONS IN JOURNALS AND CONFERENCES	v
LIST OF FIGURES	ix
LIST OF TABLES	xvi
NOMENCLATURE	xvii
1. Introduction	1
1.1 Background	1
1.2 Motivation for the study	2
1.3 Purpose of the study	4
1.4 Literature survey	4
1.5 Organisation of the study	10
2. Experimental Method and Results	11
2.1 Objectives of the experiments	11
2.2 Description of experimental set-up	11
2.3 Experimental results	14
2.3.1 Problem formulation	14
2.3.2 Heat transfer enhancement	15
2.3.2.1 Densities	15
2.3.2.2 Solidification times	16
2.3.2.3 Effect of vibration on solidification times	17
2.4 Experimental conclusions	22
3. Problem Formulation - Theoretical	24
3.1 Objective of the theoretical analysis	24
3.2 Assumptions	24
3.3 Governing equations	24
3.4 Transformation into the spectral equations in space	29

© University of Pretoria

3.5 Summary 37

4. Theoretical Method of Solution and Presentation 38

4.1 Numerical solution evaluated using Fortran 38

4.2 Graphical representation of the results 38

4.3 Lyapunov exponents 45

4.4 Heat flux and Nusselt number 46

4.5 Summary 49

5. Theoretical Results and Discussion 50

5.1 Results for the amplitudes subject to varying Rayleigh numbers and frequency 50

5.2 Results for the Lyapunov exponents 77

5.3 Results for the average heat flux in terms of Nusselt number 89

5.4 Summary 93

6. Summary, Conclusions and Recommendations 95

6.1 Summary 95

6.2 Conclusions 97

6.3 Recommendations for future work 99

REFERENCES 101

© University of Pretoria

LIST OF FIGURES: page

Figure 1.1: (a) Directional solidification by cooling from below, (b) directional solidification by cooling from above, (c) a porous layer heated from below and subject to vibrations. 6

Figure 2.1: Picture and schematic of experimental set-up showing the thermal bath, vibration exciter, test sample location, and cantilever system attached to the rigid frame. 12

Figure 2.2: Mass of solid paraffin wax formed versus time for no vibration and vibration frequency of 100 Hz for five samples of each. 18

Figure 2.3: Average mass of solid paraffin wax formed versus time for no vibration and vibration frequency of 100 Hz. 19

Figure 2.4: Solidified paraffin wax samples cut in half after 5 min for 0 Hz (no vibration) and 100Hz (with vibration), with the blue outline indicating the average wall thickness of the solidified paraffin wax and the centre void, and the red outline indicating the air gap. 20

Figure 2.5: Solidified paraffin wax samples cut in half after 10 min for 0 Hz (no vibration) and 100Hz (with vibration), with the blue outline indicating the average wall thickness of the solidified paraffin wax and the centre void, and the red outline indicating the air gap. 21

Figure 2.6: Solidified paraffin wax samples cut in half after 20 min for 0 Hz (no vibration) and 100Hz (with vibration), with the blue outline indicating the average wall thickness of the solidified paraffin wax and the centre void, and the red outline indicating the air gap. 21

Figure 2.7: Solidified paraffin wax samples cut in half after 30 min for 0 Hz (no vibration) and 25 minutes for 100Hz (with vibration), with the blue outline indicating the void geometry formed, and the red outline indicating the air gap. 22

Figure 3.1: A two-dimensional rectangular domain heated from below (or cooled from above) subject to accelerations due to gravity and imposed vibrations. 28

© University of Pretoria

Figure 3.2: Bifurcation diagrams representing the fixed points (Vadasz, 2001). 34

Figure 4.1: The trajectory of the solution $X = \sin(t)$, $Y = \cos(3t)$, $Z = \cos(t)$ on a three-dimensional phase diagram. 39

Figure 4.2: Projections of the trajectory of the solution $X = \sin(t)$, $Y = \cos(3t)$, $Z = \cos(t)$ on the $X - Y$, $X - Z$, and $Y - Z$ planes. 40

Figure 4.3: The trajectory of the solution $X = \sin(t)$, $Y = \cos(t)$, $Z = \cos(2t)$ on a three-dimensional phase diagram. 41

Figure 4.4: $X = \sin(t)$, $Y = \cos(t)$, $Z = \cos(2t)$ on the $X - Y$, $X - Z$, and $Y - Z$ planes. 42

Figure 4.5: A torus on which the trajectory is allowed to move. 43

Figure 4.6: A closed trajectory of a motion on a torus representing periodic motion. 44

Figure 4.7: A trajectory that cannot close on a torus representing quasi-periodic motion. 44

Figure 5.1: Graphical description of the solutions for $\omega = 0$, $R = 25$: (a) The amplitude X in the time domain, i.e. X versus t, (b), (c), and (d). The solution on a phase diagram: projections of the solution on the $X - Y$, $X - Z$, and $Y - Z$ planes, respectively. The data points are not connected. 51

Figure 5.2: Graphical description of the solutions for $\omega = 0$, $R = 25$: (a) The amplitude X in the time domain, i.e. X versus t, (b), (c), and (d). The solution on a phase diagram: projections of the solution on the $X - Y$, $X - Z$, and $Y - Z$ planes, respectively. The data points are connected. 52

Figure 5.3: Graphical description of the solutions for $\omega = 1$, $R = 25$: (a) The amplitude X in the time domain, i.e. X versus t, (b), (c), and (d). The solution on a phase diagram: projections of the solution on the $X - Y$, $X - Z$, and $Y - Z$ planes, respectively. (e) Zoom into the time domain $180 \leq t \leq 200$, X versus t. 53

© University of Pretoria

Figure 5.4: Graphical description of the solutions for $\omega = 5$, $R = 25$: (a) The amplitude X in the time domain, i.e. X versus t, (b), (c), and (d). The solution on a phase diagram: projections of the solution on the $X - Y$, $X - Z$, and $Y - Z$ planes, respectively. (e) Zoom into the time domain $180 \leq t \leq 200$, X versus t. 55

Figure 5.5: Graphical description of the solutions for $\omega = 6.5$, $R = 25$: (a) The amplitude X in the time domain, i.e. X versus t, (b), (c), and (d). The solution on a phase diagram: projections of the solution on the $X - Y$, $X - Z$, and $Y - Z$ planes, respectively. (e) Zoom into the time domain $200 \leq t \leq 210$, X versus t. 56

Figure 5.6: Graphical description of the solutions for $\omega = 7$, $R = 25$: (a) The amplitude X in the time domain, i.e. X versus t, (b), (c), and (d). The solution on a phase diagram: projections of the solution on the $X - Y$, $X - Z$, and $Y - Z$ planes, respectively. 57

Figure 5.7: Graphical description of the solutions for $\omega = 8$, $R = 25$: (a) The amplitude X in the time domain, i.e. X versus t, (b), (c), and (d). The solution on a phase diagram: projections of the solution on the $X - Y$, $X - Z$, and $Y - Z$ planes, respectively. 58

Figure 5.8: Graphical description of the solutions for $\omega = 8.1325$, $R = 25$: (a) The amplitude X in the time domain, i.e. X versus t, (b), (c), and (d). The solution on a phase diagram: projections of the solution on the $X - Y$, $X - Z$, and $Y - Z$ planes, respectively. 60

Figure 5.9: Graphical description of the solutions for $\omega = 10$, $R = 25$: (a) The amplitude X in the time domain, i.e. X versus t, (b), (c), and (d). The solution on a phase diagram: projections of the solution on the $X - Y$, $X - Z$, and $Y - Z$ planes, respectively. 61

Figure 5.10: Graphical description of the solutions for $\omega = 13.5$, $R = 25$: (a) The amplitude X in the time domain, i.e. X versus t, (b), (c), and (d). The solution on a phase diagram: projections of the solution on the $X - Y$, $X - Z$, and $Y - Z$ planes, respectively. 62

© University of Pretoria

Figure 5.11: Graphical description of the solutions for $\omega = 20$, $R = 25$: (a) The amplitude X in the time domain, i.e. X versus t, (b), (c), and (d). The solution on a phase diagram: projections of the solution on the $X-Y$, $X-Z$, and $Y-Z$ planes, respectively. 63

Figure 5.12: Graphical description of the solutions for $\omega = 0$, $R = 75$: (a) The amplitude X in the time domain, i.e. X versus t, (b), (c), and (d). The solution on a phase diagram: projections of the solution on the $X-Y$, $X-Z$, and $Y-Z$ planes, respectively. 65

Figure 5.13: Graphical description of the solutions for $\omega = 5$, $R = 75$: (a) The amplitude X in the time domain, i.e. X versus t, (b), (c), and (d). The solution on a phase diagram: projections of the solution on the $X-Y$, $X-Z$, and $Y-Z$ planes, respectively. 66

Figure 5.14: Graphical description of the solutions for $\omega = 6.5$, $R = 75$: (a) The amplitude X in the time domain, i.e. X versus t, (b), (c), and (d). The solution on a phase diagram: projections of the solution on the $X-Y$, $X-Z$, and $Y-Z$ planes, respectively. 67

Figure 5.15: Graphical description of the solutions for $\omega = 8$, $R = 75$: (a) The amplitude X in the time domain, i.e. X versus t, (b), (c), and (d). The solution on a phase diagram: projections of the solution on the $X-Y$, $X-Z$, and $Y-Z$ planes, respectively. 68

Figure 5.16: Graphical description of the solutions for $\omega = 25.2$, $R = 75$: (a) The amplitude X in the time domain, i.e. X versus t, (b), (c), and (d). The solution on a phase diagram: projections of the solution on the $X-Y$, $X-Z$, and $Y-Z$ planes, respectively. 69

Figure 5.17: Graphical description of the solutions for $\omega = 26$, $R = 75$: (a) The amplitude X in the time domain, i.e. X versus t, (b), (c), and (d). The solution on a phase diagram: projections of the solution on the $X-Y$, $X-Z$, and $Y-Z$ planes, respectively. 70

Figure 5.18: Graphical description of the solutions for $\omega = 28.5$, $R = 75$: (a) The amplitude X in the time domain, i.e. X versus t, (b), (c), and

© University of Pretoria

(d). The solution on a phase diagram: projections of the solution on the $X-Y$, $X-Z$, and $Y-Z$ planes, respectively. 71

Figure 5.19: Graphical description of the solutions for $\omega = 28.515$, $R = 75$: (a) The amplitude X in the time domain, i.e. X versus t, (b), (c), and (d). The solution on a phase diagram: projections of the solution on the $X-Y$, $X-Z$, and $Y-Z$ planes, respectively. 72

Figure 5.20: Graphical description of the solutions for $\omega = 44$, $R = 75$: (a) The amplitude X in the time domain, i.e. X versus t, (b), (c), and (d). The solution on a phase diagram: projections of the solution on the $X-Y$, $X-Z$, and $Y-Z$ planes, respectively. 73

Figure 5.21: Graphical description of the solutions for $\omega = 45.9$, $R = 75$: (a) The amplitude X in the time domain, i.e. X versus t, (b), (c), and (d). The solution on a phase diagram: projections of the solution on the $X-Y$, $X-Z$, and $Y-Z$ planes, respectively. 74

Figure 5.22: Graphical description of the solutions for $\omega = 46$, $R = 75$: (a) The amplitude X in the time domain, i.e. X versus t, (b), (c), and (d). The solution on a phase diagram: projections of the solution on the $X-Y$, $X-Z$, and $Y-Z$ planes, respectively. 75

Figure 5.23: Graphical description of the solutions for $\omega = 100$, $R = 75$: (a) The amplitude X in the time domain, i.e. X versus t, (b), (c), and (d). The solution on a phase diagram: projections of the solution on the $X-Y$, $X-Z$, and $Y-Z$ planes, respectively. 76

Figure 5.24: Graphical description of the solutions for $\omega = 6.5$, $R = 14$: (a) The amplitude X in the time domain, i.e. X versus t, (b), (c), and (d). The solution on a phase diagram: projections of the solution on the $X-Y$, $X-Z$, and $Y-Z$ planes, respectively. 78

Figure 5.25: Graphical description of the solutions for $\omega = 6.5$, $R = 17$: (a) The amplitude X in the time domain, i.e. X versus t, (b), (c), and (d). The solution on a phase diagram: projections of the solution on the $X-Y$, $X-Z$, and $Y-Z$ planes, respectively. 79

© University of Pretoria

Figure 5.26: Graphical description of the solutions for $\omega = 6.5$, $R = 20$: (a) The amplitude X in the time domain, i.e. X versus t, (b), (c), and (d). The solution on a phase diagram: projections of the solution on the $X-Y$, $X-Z$, and $Y-Z$ planes, respectively. 80

Figure 5.27: Graphical description of the Lyapunov exponents for $\omega = 6.5$. 81

Figure 5.28: Graphical description of the Lyapunov exponents for $\omega = 0$. 83

Figure 5.29: Graphical description of the Lyapunov exponents for $\omega = 8$. 84

Figure 5.30: Graphical description of the Lyapunov exponents for $\omega = 26$. 85

Figure 5.31: Graphical description of the Lyapunov exponents for $\omega = 28.5$. 86

Figure 5.32: Graphical description of the Lyapunov exponents for $\omega = 46$. 87

Figure 5.33: Graphical description of the Lyapunov exponents for $\omega = 100$. 88

Figure 5.34: Graphical description of the average heat flux in terms of the Nusselt number for forced vibrations at a frequency of $\omega = 1$ (and forcing vibration amplitude $\delta = 1$) in comparison with the average heat flux in the absence of forced vibrations, i.e. $\omega = 0$, $\delta = 0$. 90

Figure 5.35: Graphical description of the average heat flux in terms of the Nusselt number for forced vibrations at a frequency of $\omega = 6.5$ (and forcing vibration amplitude $\delta = 1$) in comparison with the average heat flux in the absence of forced vibrations, i.e. $\omega = 0$, $\delta = 0$. 91

Figure 5.36: Graphical description of the average heat flux in terms of the Nusselt number for forced vibrations at a frequency of $\omega = 25.2$ (and forcing vibration amplitude $\delta = 1$) in comparison with the average heat flux in the absence of forced vibrations, i.e. $\omega = 0$, $\delta = 0$. 92

© University of Pretoria

Figure 5.37: Graphical description of the average heat flux in terms of the Nusselt number for forced vibrations at a frequency of $\omega = 46$ (and forcing vibration amplitude $\delta = 1$) in comparison with the average heat flux in the absence of forced vibrations, i.e. $\omega = 0$, $\delta = 0$. 93

© University of Pretoria

LIST OF TABLES: page

Table 2.1: Measured weight of PCM at different times for no vibration and vibration at frequency of 100 Hz. 16

Table 2.2: Measured mass of solidified paraffin wax at different times under no vibration for five samples. 17

Table 2.3: Measured mass of solidified paraffin wax at different times under a vibration frequency of 100 Hz for five samples. 17

Table 2.4: Average calculated mass of solidified paraffin wax at different times for no vibration and vibration at frequency of 100 Hz. The results are the average results in the last columns of Tables 2.2 and 2.3. 18

Table 4.1: The four types of attractors in a system of order three and their Lyapunov exponents. 46

© University of Pretoria

NOMENCLATURE

Latin Symbols

a = amplitude

f = frequency

g = gravity

Gr = Grashof number

k = permeability of the porous domain

m = mass

r = inner radius of plastic container

Da = Darcy number defined by k/l^2

Pr = Prandtl number defined by υ/α

Nu = Nusselt number

Ra = Rayleigh number

R = rescaled Rayleigh number defined by $Ra/\pi^2\theta^2$

R_v = enhancement ratio $Gr_v/Gr = a\omega^2/g$

T_C = coldest wall temperature

T_H = hottest wall temperature

a_{v^*} = acceleration due to vibration

h = length or diameter (depending on geometry)

t = time

$t_\Delta = (t_S - t_{SV})/t_S$

t_S = dimensional solidification time

t_{S100Hz} = dimensional solidification time at 100 Hz vibration frequency

K = permeability

$V_{paraffin_wax}$ = volume of solid paraffin wax in plastic container

V_{Total} = total volume of plastic container

V_{water} = volume of water

u = horizontal x component of the velocity

v = horizontal y component of the velocity

w = vertical component of the velocity

© University of Pretoria

X = rescaled amplitude A_{11}, equation (53)

Y = rescaled amplitude B_{11}, equation (54)

Z = rescaled amplitude B_{02}, equation (55)

Greek Symbols

υ = kinematic viscosity

β = volumetric thermal expansion coefficient

ω_* = angular velocity

$\tilde{\omega}$ = dimensionless vibration frequency

μ = dynamic viscosity

φ = porosity

α_e = effective thermal diffusivity

γ = a parameter defined by equation (60)

θ = a parameter defined by equation (61)

ΔT_c = characteristic temperature difference

A_{υ^*} = vibrational acceleration amplitude

δ = dimensionless vibrational amplitude

ψ = stream-function

λ = Lyapunov exponents

ρ = density

Subscripts

* = dimensional values

V = vibrational

C = related to the coldest wall

H = related to the hottest wall

S = solidification without vibration

SV = solidification under vibration

V = vibration

water = water at 15°C

© University of Pretoria

CHAPTER 1

INTRODUCTION

1.1 Background

In the solidification process of binary alloys, there exist three distinct regions (layers), namely a fluid binary mixture, the solid layer and a two-phase (fluid-solid) mushy layer. The mushy layer is practically a porous medium consisting of an interconnected solid phase with voids occupied by the melted binary fluid. Although many researchers have studied the effect of vibrations on solidification theoretically and experimentally, there is no clear understanding of a precise mechanism improving the mechanical properties of the cast. This is because the solidificaiton process is very complex and involves a great number of phenomena linking fluid mechanics to mass and heat transfer with phase change. Natural convevtionis considered as the dominant mechanism of heat transfer in the solidification in open literature. Therefore, the objective of this thesis is to investigate the effect of heat transfer alone on a porous mushy layer subject to vibration and to study whether the thermal resonance may or may not enhance the heat transfer.

It appears that ultrasonic vibration for metallurgical applications aiming at improving the cast metal quality dates back to 1878, as indicated by Jian et al. (2005). This suggests that the “injection of ultrasonic energy into molten alloys brings about nonlinear effects such as cavitation, acoustic streaming, emulsification, and radiation pressure, which are used to refine microstructures, reduce segregation, and improve secondary phase formation and distribution.”

In general, there is a large volume of both theoretical as well as experimental work attempting to investigate the effect of vibrations on the solidification process. An attempt in linking experimental results and theory was presented, for example, by Li et al. (2007). Mathematical modelling of convection-induced oscillatory structure formation in peritectic alloys was presented by Mazumder et al. (2000). This solved the convection equations numerically and predicted a band structure for the solid composition oscillating between two distinct values. Controlling the microstructure that results from the casting process is considered one of the main contemporary challenges of the foundry industry. Promoting fine microstructures in the cast is desirable because of its resulting favourable mechanical properties of strength, ductility, low susceptibility of micro porosity and crack formation.

© University of Pretoria

Chirita et al. (2009) indicate that mechanical, sonic and ultrasonic vibrations may promote "grain refinement, increased density, degassing, low shrinkage porosities, and changing the shape, size and distribution of the second phase". Chirita et al. (2009) investigated the influence of vibrations on aluminium-silicon alloys. Their experimental results show that mechanical properties were substantially affected by the level of applied frequency. Consequently, the tensile strength was improved for low vibration frequencies but decreased for high frequencies, as compared with gravity castings without vibration. Chirita et al. (2009) mention that "a heat-transfer mechanism, that is acceleration dependent, seems to be responsible for the shift in mechanical properties' response to the vibration effect".

Jian et al. (2005) indicate that "ultrasonic treatment of aluminium alloys, in general, has been studied extensively and it has been shown that the introduction of high intensity ultrasonic vibration into the melt can eliminate columnar dendritic structure, refine the equiaxed grains, and under some conditions, produce globular non-dendritic grains".

Mechanisms for grain refinement under ultrasonic vibrations have been proposed, for example, by Eskin (1994) and Abramov et al. (1998). "They are related to ultrasonically induced cavitations, which produce large instantaneous pressure and temperature fluctuations in the melt. These pressure and temperature fluctuations are likely to induce heterogeneous nucleation in the melt. They are also likely to promote dendrite fragmentation by enhancing solute diffusion through acoustic streaming." However, Jian et al. (2005) state that there is no convincing evidence as to which mechanism, i.e. heterogeneous nucleation or dendrite fragmentation, is more important for grain refinement under ultrasonic vibrations.

1.2 Motivation for the study

Despite the extensive work undertaken so far both experimentally as well as theoretically on the effect of vibrations on solidification, the conclusions from such studies are far from indicating a clear answer as to the precise mechanisms that are responsible for the improvement of mechanical properties of the cast (see, for example, Caram et al., 1991). It is evident from these studies that substantial improvement was accomplished. However, in taking advantage of it, one needs a consistent procedure that can be devised by first identifying which mechanism is responsible for which effect and then a consistent use of such a procedure in the solidification process.

© University of Pretoria

From the literature survey presented in the next section, it becomes quite evident that the probable reason for the lack of such consistency and clear answers is due to the fact that the solidification process is a very complex one and includes a large number of phenomena linking fluid mechanics with heat and mass transfer processes with phase change and transport phenomena in multiphase media. Due to the large number of phenomena, the resulting controlling parameters are extremely large too.

Therefore, the combined effect of these different phenomena on the solidification process and its control becomes extremely difficult to analyse leading to different results under different conditions. Even if one takes a separated effect of thermohaline convection in porous media that can be regarded as the fundamental process of double-diffusion with convection in a mushy layer, the latter although widely investigated still leaves much room for progress because of the difficulty of investigating strongly non-linear effects beyond the convection threshold, such as weak and strong turbulence.

It is therefore appealing to focus the investigation on one particular direction separating the solidification process into its different contributions. As such, the present work is divided into a small experimental part that aims at producing further evidence of how the solidification is affected by mechanical vibrations and an extensive theoretical part that analyses the hypothesis that such vibrations might affect substantially the heat transfer process via resonating the thermal convection in the mushy layer. Such resonance differs from the familiar resonance in linear systems because of the non-linearity of the convection process and the resulting consequences.

In order to avoid focusing on a very narrow parameter domain around the convection threshold, the mathematical model derived in the present work uses a spectral method similar to the one proposed by Lorenz (1963), (see also Sparrow, 1982) for natural convection in a fluid layer.

The advantage of using this approach is in gaining detailed insight on the effect of vibrations into the heat convection in porous media and the possibility of heat transfer enhancement if thermal resonance can yield such enhancement. This is by no means certain as some prior research results (Mladin and Zumbrunnen, 1995, Vadasz, 1998, Vadasz and Olek, 1999, 2000, Vadasz 1999 a,b, 2001) suggest that periodic convection may possibly even reduce rather than enhance the heat transfer.

The drawback in such an approach is in focusing on only one separate mechanism of the solidification process. The gain in detailed information on this one separate mechanism

© University of Pretoria

is countered by a lack of information on the mass transfer, phase change and other possible mechanisms as well as the lack of information about the interaction between these distinct mechanisms.

1.3 Purpose of study

Identifying regimes of enhancement in heat transfer is one of the aims and therefore the purpose of this study is to investigate the effect of heat transfer alone on a porous layer (representing the mushy layer in the solidification process) subject to vibration and particularly identifying thermal resonance occurrence and whether the thermal resonance may or may not enhance the heat transfer. A sufficiently wide parameter regime is to be considered, yet the work is to be undertaken via analytical or combined analytical-numerical methods in order to be able to draw qualitative as well as quantitative conclusions.

1.4 Literature survey

Experimental studies on solidification are often compared by using solidification of aqueous solutions of binary substances, e.g. ammonium chloride, because of the analogy the this holds with solidification of metal alloys (Nield and Bejan, 2006). Using such practices simplifies the experimental system as it allows the possibility of working at substantially lower temperatures.

Experimental studies were conducted among others by Choi and Viskanta (1993), and Matsumoto et al. (1993, 1995) for solidification produced by cooling a rectangular box from the side; by Cao and Poulikakos (1991 a, b) and Choi and Viskanta (1992), for solidification with cooling from above; and by Song et al. (1993), for solidification with cooling from below.

As natural convection is the dominant mechanism of heat transfer in solidification, the orientation of the thermal gradient imposed via the applied boundary conditions relative to the acceleration due to gravity becomes an essential contributing factor to the resulting fluid flow.

The process of solidification is represented graphically in Figure 1 (a), (b) where two orientations with respect to gravity are considered, namely cooling from below in Figure 1 (a), and cooling from above in Figure 1 (b).

© University of Pretoria

In the case of cooling from below presented in Figure 1 (a), the liquid solidifies as it cools down creating a mushy layer consisting of both solid as well as liquid phases. This mushy layer is actually a porous medium. The solidification fronts on both sides of the mushy layer move upwards in what is usually assumed to be a constant speed hence creating a typical directional solidification. Then, one may represent the governing equations in a system of coordinates linked to these constant-speed moving fronts.

Generally, the natural convection in such a configuration occurs due to the compositional gradient (mass transfer), which is larger on the top of the mushy layer than on its bottom side. The heating from above acts as a stabilising 'agent'. As a result of double-diffusive processes (thermal diffusion as well as molecular diffusion due to the composition component), quite a variety of flow regimes and flow patterns become possible during the natural convection.

On the other hand, when the cooling is applied from above, the solidification fronts move downwards as more of the melt liquid solidifies. In such a case, the heat transfer acts as a destabilising 'agent' while the mass transfer due to the composition in the mushy layer acts as a stabilising 'agent'. This occurs because the composition is larger at the bottom of the mushy layer than on the top next to the solidified material.

A typical configuration of heat transfer in a porous layer heated from below and subject to vibrations is presented schematically in Figure 1 (c).

© University of Pretoria

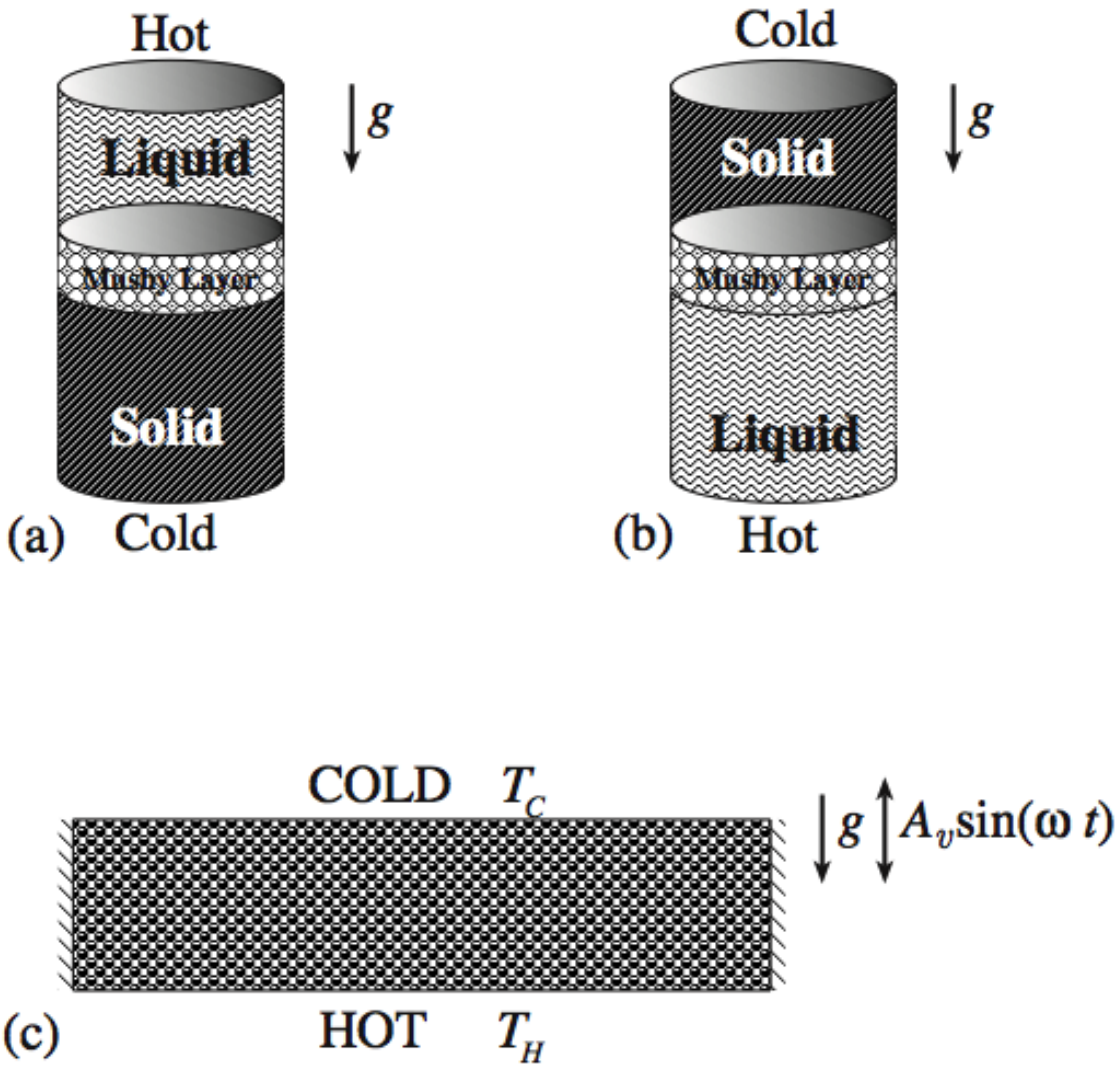

Figure 1.1: (a) Directional solidification by cooling from below, (b) directional solidification by cooling from above, (c) a porous layer heated from below and subject to vibrations.

The origin of freckles was initially suggested by Copey et al. (1970) followed by a large number of experiments including the use of ammonium chloride reported by Chen and Chen (1991), and Tait and Jaupart (1992), who investigated various modes of convection and their relation to the formation of freckles.

Fowler (1985) proposed a model for the mushy layer and analysed it for the limiting case of the mushy layer behaving as a non-reacting porous layer. Theoretical accounts of flow and heat transfer in a pure fluid layer (non-porous medium) subjected to vibrations have been reported among others by Gresho and Sani (1970) and Wadih and Roux (1988).

© University of Pretoria

Pillay and Govender (2005) investigated theoretically the stability of solutal convection in a gravity modulated mushy layer during solidification of binary alloys. The gravity modulation was accomplished via vibrations. They extended a model that was previously derived by Govender and Vadasz (2002 a, b, c) and Govender (2003), for solidification in a rotating mushy layer. The work focused on linear stability analysis and provided useful stability maps.

Their results were presented for both synchronous as well as sub-harmonic solutions and concluded that up to the transition point from synchronous to sub-harmonic regions in the parameter domain, increasing the vibration frequency rapidly stabilises the solutal convection. Beyond this transition point, increasing further the vibration frequency tended to gradually destabilise the solutal convection. They also showed that increasing the ratio between the Stefan number and the solid composition destabilised the solutal convection.

Weak non-linear solutions for the convection in the mushy layer, which are valid near the convection threshold, were derived by Amberg and Homsy (1993). As distinct from Fowler (1985), the mushy layer was decoupled from the liquid melt and the solid layer in Amberg and Homsy's (1993) model. Consequently, they applied perturbations to reintroduce the variations of permeability in the mushy layer in order to relax a too restricted resulting configuration that departs from reality.

An extension of Amberg and Homsy's (1993) model was introduced by Anderson and Worster (1995, 1996), which used a large Stefan number scaling and identified another oscillatory mode of convection different from the double-diffusive mode observed by Chen et al. (1994).

Linear stability analysis for moderate time scales applicable to moderate Stefan number convection in a rotating mushy layer was presented by Govender and Vadasz (2002a). The corresponding weak non-linear analyses for moderate Stefan number convection in a rotating mushy layer were presented by Govender and Vadasz (2002b), for oscillatory convection solutions and by Govender and Vadasz (2002c), for stationary convection solutions.

Govender (2004) presented a linear stability for natural convection in a vertically modulated porous layer subject to constant vertical stratification and obtained a Mathieu equation that was solved in terms of Mathieu functions.

© University of Pretoria

The analysis of the transition point from synchronous to sub-harmonic solutions was investigated by Govender (2005a).

Govender (2005b) showed that a vibrating fluid-saturated porous layer can be destabilised even when heated from above as the gravity modulation due to vibrations may on average overcome the opposite stabilising effect due to gravity (heating from above). As the results represent linear stability solutions, the amplitude of convection is not obtained.

To overcome the amplitude of convection Govender (2005c) presented results where the amplitude of convection may be evaluated using the assumption of a "frozen time", which might be applicable for large time scales and consequently small frequencies. In addition, weak non-linear solutions, which provide information about the amplitude convection near the convection threshold, were presented by Govender (2005d). A comprehensive review of all these results was presented by Govender (2008).

The theoretical results presented above usually correspond to a rectangular two-dimensional layer. As distinct from the rectangular geometries considered previously, a cylindrical vibrating porous layer was considered by Govender (2006) in producing results of linear stability, while the stability of solutal convection in a cylindrical mushy layer subject to vibrations was presented by Govender (2011). A combination of rotation and vibrations on convection in a porous layer far away from the axis of rotation was presented by Govender (2010).

Elhajjar et al. (2009) analysed the effect of small-amplitude and high-frequency vertical vibrations on the separation of a binary mixture saturating a shallow horizontal porous layer heated from below. They applied direct numerical simulations and linear stability analysis to the two-dimensional equations averaged over the period of the impressed vibrations.

The averaging method adopted by Elhajjar et al. (2009) can be justified for thermal vibrational convection in the limit of small-amplitude and high-frequency vibrations. The method is similar to the one adopted by Bardan and Mojtabi (2000), for investigating the convective instability in a porous layer subject to vertical vibration, or by Charrier-Mojtabi et al. (2007) dealing with Soret-driven convection in a horizontal porous layer.

Jounet and Bardan (2001) adopted a similar averaging method to investigate the onset of thermohaline convection in a rectangular porous cavity subject to vibrations. They

© University of Pretoria

performed a linear stability analysis, a weak non-linear analysis as well as a direct numerical simulation to confirm and illustrate their findings. They focused on the analysis of the stationary bifurcation, which as expected turned out to be of a pitchfork type. They also concluded that depending on the governing parameters, vibrations could delay or promote the onset of convection. An extensive review of computational heat convection in porous media with applications among others to alloy solidification was conducted by Vafai and Hadim (2000).

There are at least seven dimensionless parameters affecting the natural convection in solidification processes in a vibrating mushy layer. The gravity-related thermal Rayleigh number, $Ra_T = \beta_{T*} \Delta T_c g K_o l_c / \tilde{\alpha}_e \nu$; the vibrational thermal Rayleigh number, $Ra_v = \beta_{T*} \Delta T_c \omega^2 K_o l_c^2 / \tilde{\alpha}_e \nu$; the gravity related compositional (solute) Rayleigh number $Ra_C = \beta_{C*} \Delta C_c g K l_c / D_m \nu$; the Prandtl number, $Pr = \nu / \tilde{\alpha}_e$; the Schmidt number, $Sc = \nu / D_m$; or alternatively the Lewis number $Le = \tilde{\alpha}_e / D_m$; the Darcy number $Da = K_o / l_c^2$; and the Stefan number, $St = h_{fs} / (\rho c_p)_{eff} \Delta T_c$, the Stefan number representing the ratio of the latent heat h_{fs} to heat content or internal energy, are the dimensionless groups appearing in the solidification process.

Pillay and Govender (2005) also introduced a modified Froude number in the analysis. The symbols represent the thermal expansion coefficient β_{T*}; the solutal expansion coefficient β_{C*}; a characteristic temperature difference ΔT_c, such as the difference between the imposed hot and cold temperatures on the top and bottom boundaries; a characteristic composition difference ΔC_c; acceleration due to gravity g; a reference value of the permeability K_o; a characteristic length scale l_c, such as the height of the mushy layer; the effective thermal diffusivity $\tilde{\alpha}_e$; the fluid's kinematic viscosity ν; and the molecular diffusivity D_m.

The large number of dimensionless parameters identified and the large number of mechanisms that are coupled in the solidification process in the mushy layer make the attributing of a particular result to one single mechanism, or to limited coupled mechanisms, extremely difficult when analysing all these mechanisms together, whether the this is performed analytically, numerically or experimentally.

The studies carried out so far focused on very narrow parameter ranges in order to investigate the non-linear coupled effects and draw some conclusions. Linear stability and weak non-linear analyses are valid in the very close vicinity of the convection onset.

© University of Pretoria

Vadasz and Olek (1999, 2000) and Vadasz (1999 a, b, 2001) developed a spectral method of analysing heat convection problems beyond the neighbourhood of the convection onset. Essentially, the method uses the eigenfunctions obtained from the weak non-linear analysis to yield a truncated system of ordinary differential equations representing the dynamics of the convection process, i.e. its behaviour in time. This system was shown to be similar to the Lorenz system (Lorenz, 1963; Sparrow, 1982).
More recently Mahmud and Hashim (2010, 2011), and Roslan et al. (2011) showed that this system could be controlled by using feedback control methods in order to promote or delay the transition from laminar to weak turbulent convection. Their results were extended by Magyari (2010a) and Vadasz (2010), while Magyari (2010b) showed how this system could be seen as a system of coupled oscillators. This spectral method was adopted in the present work to allow the analysis beyond the convection onset and even investigate the transition to weak turbulence for the problem of heat convection in a porous layer heated from below and subject to vibrations.

1.5 Organisation of the study

The experimental part of the study is presented in Chapter 2, where the solidification of paraffin subject to vibrations was observed aiming at investigating how the heat transfer, average density of the solid product and void formation were affected by the vibrations. Chapter 3 introduces the theoretical part of the study, the problem formulation via the governing equations and their transformation into their spectral form in space. The theoretical method of solution is presented in Chapter 4, followed by the presentation of the results in Chapter 5. The conclusions are then presented in Chapter 6.

© University of Pretoria

CHAPTER 2

EXPERIMENTAL METHOD AND RESULTS

2.1 Objectives of the experiments

Observing the solidification process of paraffin subject to vibrations could possibly lead to conclusions on the effects the vibrations have on the heat transfer and the average density of the solid product. In order to accomplish this a set of experiments was run with and without vibrations and data were recorded at different time intervals during the solidification process. During these experiments, the total solid formed was measured and recorded for comparison. The objective was to observe how the vibrations affect the heat transfer, and whether such an effect would be enhancing or reducing the heat transfer. Further experiments were performed with the objective of achieving different average densities for the paraffin and checking the possibility of controlling the average density and void formation.

2.2 Description of experimental set-up

In this study, the paraffin wax (RT35) was selected as a medium on which to conduct experiments because it had a clearly defined macroscopic crystal structure consisting of mostly large straight-chain hydrocarbons. The advantage of the large straight-chain hydrocarbons was that the dendritic spacing was not affected by the cooling rate. The properties of the paraffin wax used were: a melting temperature of 29°C to 36°C; a solidification temperature of 36°C to 31°C (typically 35°C); with a density of 860 kg/m^3 at 15°C; and with a flashpoint of 167°C.

Experiments were conducted with spherical geometries because a comparison (although limited) could be made to work presented by Assis *et al*. 2008, which studied the numerical and experimental solidification of paraffin wax, however, without vibration. One of the diameters studied was the same as in this study and therefore used for verification purposes. The spherical samples were generated from pouring liquid paraffin wax into a plastic container with an inner diameter of 40 mm and a wall thickness of 1 mm. The geometries of the plastic container were measured with a vernier caliper.

© University of Pretoria

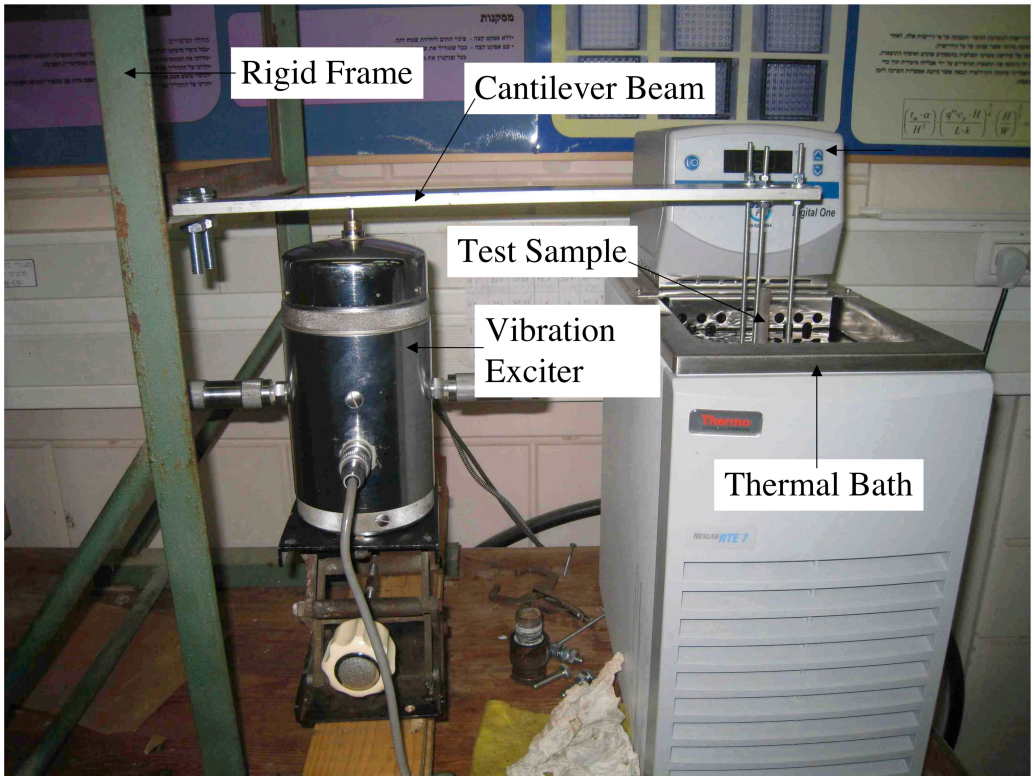

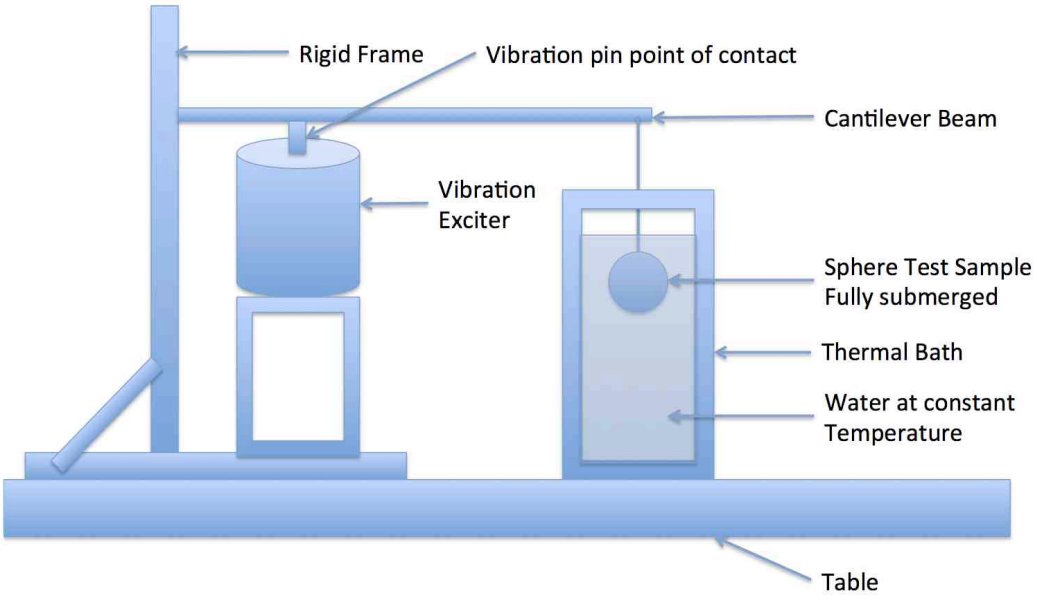

Figure 2.1: Picture and schematic of experimental set-up showing the thermal bath, vibration exciter, test sample location, and cantilever system attached to the rigid frame.

Figure 2.1 shows the experimental set-up that was developed on which paraffin wax solidification experiments can be conducted, with and without vibration. The set-up consisted of a frame, a thermal bath with deionized water in the tank, a digital scale for weight measurements, a hot plate for melting of the paraffin wax, a data logger

© University of Pretoria

thermometer with K-type thermocouple for temperature measurements of the ambient air and molten paraffin wax, and an infrared thermometer to measure the temperature of the solidified paraffin wax.

Liquid paraffin wax, heated to 60°C, was injected into the plastic spherical container. It was weighed to determine the mass and was suspended into the water in the thermal bath. The time from injection until it was placed into the water was less than 30 seconds. As the ambient temperature was constant at 19°C ± 2°C, the 30 seconds was negligible in comparison with the solidification time that was measured.

A thermal bath was used to cool the paraffin wax samples. The water temperature in the bath was maintained at 15°C ± 0.1°C. The digital scale was accurate up to 1/100th of a gram. The hot plate was a standard 1000 W kitchen appliance. A data logger thermometer was used with a thermocouple to measure the temperature of the paraffin wax with accuracy up to 0.1ºC. The infrared thermometer measured ambient temperature of 19ºC ± 2ºC.

The frame in Figure 2.1 was used to suspend the sample spheres inside the water tank of the thermal bath. The frame was also used to vibrate the samples by vibrating the cantilever beam, which suspended the samples. The cantilever beam was vibrated by a vibration exciter, which was placed underneath it and controlled by an amplifier and signal generator set at a frequency range between 10 – 300 Hz. The vibration exciter had a pin, which vibrated by means of electromagnetic forces pulling it back and forth. To avoid any slippage of the pin at the contact point with the cantilever beam, a small recess was drilled into the beam where the pin rested. A seismometer computer program measured the frequency and amplitude of the sample sphere by means of an accelerometer sensor, where the amplitude was always 7.95 mm ± 0.15 mm.

Two different sets of experiments were conducted. In both sets, after the samples were cut into two halves they were photographed.

The first set of experiments had the paraffin wax completely solidify. The solidification time for samples, without vibration and with vibration at each frequency, was determined by iteration. The samples were cut into two pieces and the temperature of the paraffin wax was measured. When the temperature was measured at 15°C ± 0.1°C, the solidification time was recorded. The mass of the solidified paraffin wax was measured. The average density was also determined after the paraffin wax completely solidified.

© University of Pretoria

The second set of experiments removed the samples at three time steps before the paraffin wax completely solidified. At each time step the sample was cut into two halves and the remaining liquid paraffin wax was poured out. The remaining paraffin wax was weighed and measurements of wall thickness and void size were recorded.

2.3 Experimental results

2.3.1 Problem formulation

To determine whether the vibration enhances or reduces the heat transfer rate, three variables including the average density of the paraffin wax, the Grashof number ratio and the solidification time improvement were investigated. After the liquid paraffin wax inside the plastic container was submerged in the thermal bath for a long enough period, the completely solidified paraffin wax samples were removed from the thermal bath. The average density of the paraffin wax completely solidified was then determined as:

$$\rho_{paraffin_wax} = \frac{m_{paraffin_wax}}{V_{paraffin_wax}} = \frac{m_{paraffin_wax}}{V_{Total} - V_{water}} = \frac{m_{paraffin_wax}}{\frac{4}{3}\pi r^3 - \frac{m_{water}}{\rho_{water}}} \quad (1)$$

The mass of the completely solidified paraffin wax, $m_{\text{paraffin_wax}}$, and water, m_{water}, which was poured into sample spheres to fill the void, were determined using the digital scale. The density of water, ρ_{water}, is known as 999.2 kg/m^3 Moran *et al*. (2011) at a temperature of 15°C.

The other variable that needs to be determined is the ratio between the vibration Grashof number, Equation 3, with vibration presented by Bardan and Mojtabi (2000), and the Grashof number, Equation 2, without vibration at the paraffin wax.

$$Gr = \frac{g\beta_T \Delta T h^3}{\nu^2} \quad (2)$$

$$Gr_V = \frac{a\omega^2 \beta_T \Delta T h^3}{\nu^2} \quad (3)$$

$$R_v = \frac{Gr_v}{Gr} = \frac{a\omega^2}{g} \quad (4)$$

The enhancement ratio, R_v, of the Grashof numbers in Equation 4 takes into consideration the enhancement of vibration on the Grashof number, Gr. If this enhancement is more than one, then it shows that vibration affected the heat transfer during solidification. The rate of heat transfer, which is represented in a non-

© University of Pretoria

dimensional form by the Nusselt number, is in general a function of the Reynolds number, Prandtl number and Grashof number. The Grashof number is in general the only non-dimensional group that is relevant in this study as it identifies a direct relation to the effects of vibration as presented in Equation 4 by the enhancement ratio. The enhancement ratio is directly proportional to the amplitude, a, and the square of the angular velocity, ω, which is directly related to the square of the frequency of vibrations. The solidification time improvement was determined as

$$t_{\Delta} = (t_S - t_{SV})/t_S \quad (5)$$

where t_s was the measured time to solidification without vibration, and t_{sv} the time to solidifcation with vibration.

2.3.2 Heat transfer enhancement

The results from experiments on approximately 300 samples are presented in three parts. The first part is to determine the density of the solidified paraffin wax. The second part is to determine the solidification times. The third part is to determine the effects the vibrations had on the solidification time. Additional experiments were also conducted to check repeatability.

2.3.2.1 Densities

The average densities of the samples versus frequency are shown in Table 1. It was found that for every sample of five experiments, the average densities of the experiments varied by less than 1%. The first set of samples at a frequency of 0 Hz shows the results for no vibration. The other six sets of samples show the frequency ranges from 10 Hz to 300 Hz. The Grashof number ratio assumes no affect on solidification for values less than 1, therefore at a frequency of 10 Hz where this occurs the results are not investigated further. The results show that as the enhancement ratio increased from 0 to 461, the average densities remained constant. The average density of all samples in Table 2.1 was calculated to be 859.93 kg/m^3, and the highest deviation was 1.2% from this average. Therefore, for the purpose of this study it was deduced that the density of the solidified paraffin wax was a constant. This value compares well with the 860 kg/m^3 provided by the supplier of the paraffin wax.

© University of Pretoria

Table 2.1: Samples showing the relationship between the enhancement ratio Gr_v/Gr and the average density of solidified paraffin wax. Every sample is the average of five samples.

Sample	Frequency (Hz)	$R_v = \frac{Gr_V}{Gr}$	Average Density [kg/m^3]
1	0	0	865.73
2	10	0.51	862.45
3	25	3.2	849.55
4	100	51	858.19
5	110	62	859.44
6	130	86.6	857.64
7	300	461	866.53

2.3.2.2 Solidification times

The solidification time of samples without vibration is shown in Table 2.2 and with vibration in Table 2.3. From Table 2.2, it can be concluded that the paraffin wax solidified mass increased at each of the four time steps for all five samples without vibration, and Table 2.3, with vibration frequency of 100 Hz.

Table 2.2 shows that all the samples of paraffin wax completely solidified at 30 minutes, and 25 minutes in Table 2.3. The experiments presented by Table 2.2 show the solidified paraffin wax was at 15ºC at it's centre where the time of 30 minutes was recorded, and similarly, 25 minutes was recorded in Table 2.3. An iterative process of experiments led to these results. The 100 Hz frequency, shown in Table 2.3, was found to be the optimum frequency where the vibration had most affected the solidification time. This was found when comparing a range of frequencies from 10 Hz to 300 Hz. This optimum frequency was used for all other experiments in the study. The solidification time result of 30 minutes without vibration shown in Table 2.2 compares well with the numerical and experimental results presented by Assis *et al*. (2008), where the solidification time shown for 40 mm paraffin wax samples without vibration was approximately 36 minutes. The difference of 6 minutes may be due to the paraffin wax that was used by Assis *et al*. (2008), having had a lower solidfication temperature than the one used in this study by a difference of about 7°C.

© University of Pretoria

Table 2.2: Measured mass of solidified paraffin wax at different times under no vibration for five samples.

Sample ➔	1	2	3	4	5	Average
Time (minutes)	Mass [g]	Mass [g]	Mass [g]	Mass [g]	Mass [g]	Mass [g]
5	15.45	15.65	15.61	15.52	15.67	15.58
10	17.75	17.77	17.98	17.68	17.97	17.83
20	19.88	19.84	19.90	19.68	19.70	19.80
30	21.18	21.22	21.35	21.40	21.30	21.29
Initial mass [g]	21.18	21.22	21.35	21.40	21.30	21.29

Table 2.3: Measured mass of solidified paraffin wax at different times under a vibration frequency of 100 Hz for five samples.

Sample ➔	1	2	3	4	5	Average
Time (minutes)	Mass [g]	Mass [g]	Mass [g]	Mass [g]	Mass [g]	Mass [g]
5	18.15	18.18	18.16	18.27	18.34	18.22
10	19.10	19.01	19.05	18.95	18.99	19.02
20	20.24	20.29	20.11	20.14	20.27	20.21
25	21.06	21.09	20.86	21.05	20.94	21.00
Initial mass [g]	21.06	21.09	20.86	21.05	20.94	21.00

2.3.2.3 Effect of vibration on solidification times

Each one of the five sets of samples, from Table 2.2 and Table 2.3, is shown in Figure 2.2. The mass of the samples without vibration (Table 2.2) and the samples with vibration (Table 2.3) each varied by less than 1%. Furthermore, the results show that the mass solidified with vibration was always higher then the mass solidified without vibration. The averaged results (in the last columns) from Table 2.2 and Table 2.3 are presented in Table 2.4.

© University of Pretoria

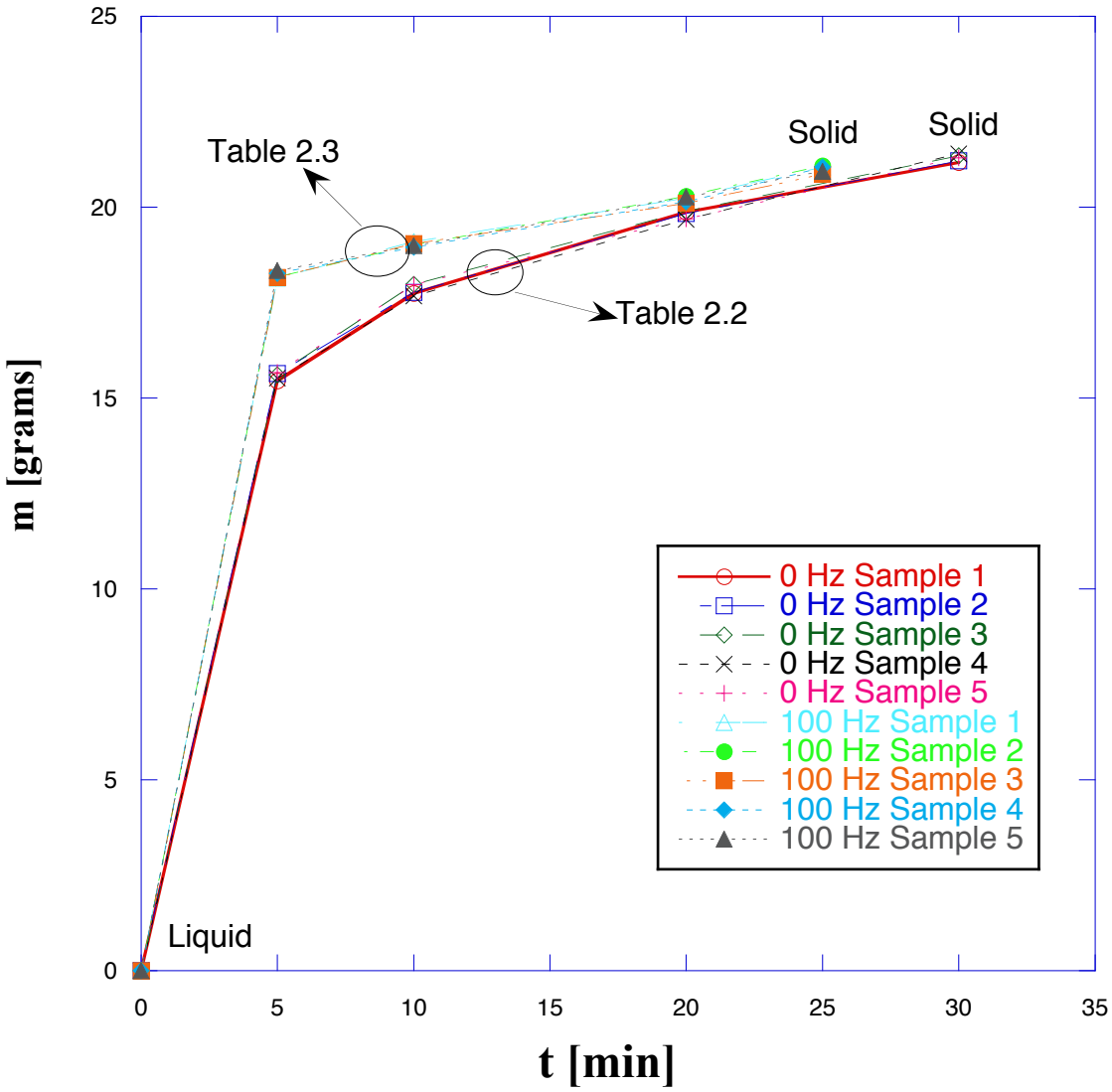

Figure 2.2: Mass of solid paraffin wax formed versus time for no vibration and vibration frequency of 100 Hz for five samples of each.

Table 2.4: Average calculated mass of solidified paraffin wax at different times for no vibration and vibration at frequency of 100 Hz. The results are the average results in the last columns of Tables 2.2 and 2.3.

Sample ➔	No vibration 0 Hz	Vibration at 100 Hz	Enhancement
Time (minutes)	Mass [g]	Mass [g]	Mass [g]
5	15.58	18.22	2.64 (17%)
10	17.83	19.02	1.19 (7%)
20	19.80	20.21	0.41 (2%)
25	-	21.00 (Solidified)	
30	21.29 (Solidified)	-	

© University of Pretoria

It is shown that at 5 minutes, more solidified paraffin wax was formed under vibration comparing the 18.22 g with the 15.58 g under no vibration. This result shows a 2.64 g of extra paraffin wax that solidified with a vibration frequency of 100 Hz at 5 minutes, which is 17% higher than that without vibration. Table 2.4 is presented on a graph in Figure 2.3, which also shows how the line for solidification under vibration frequency of 100 Hz is always above that of the line representing no vibration for each time step above 0 minutes and below 25 minutes.

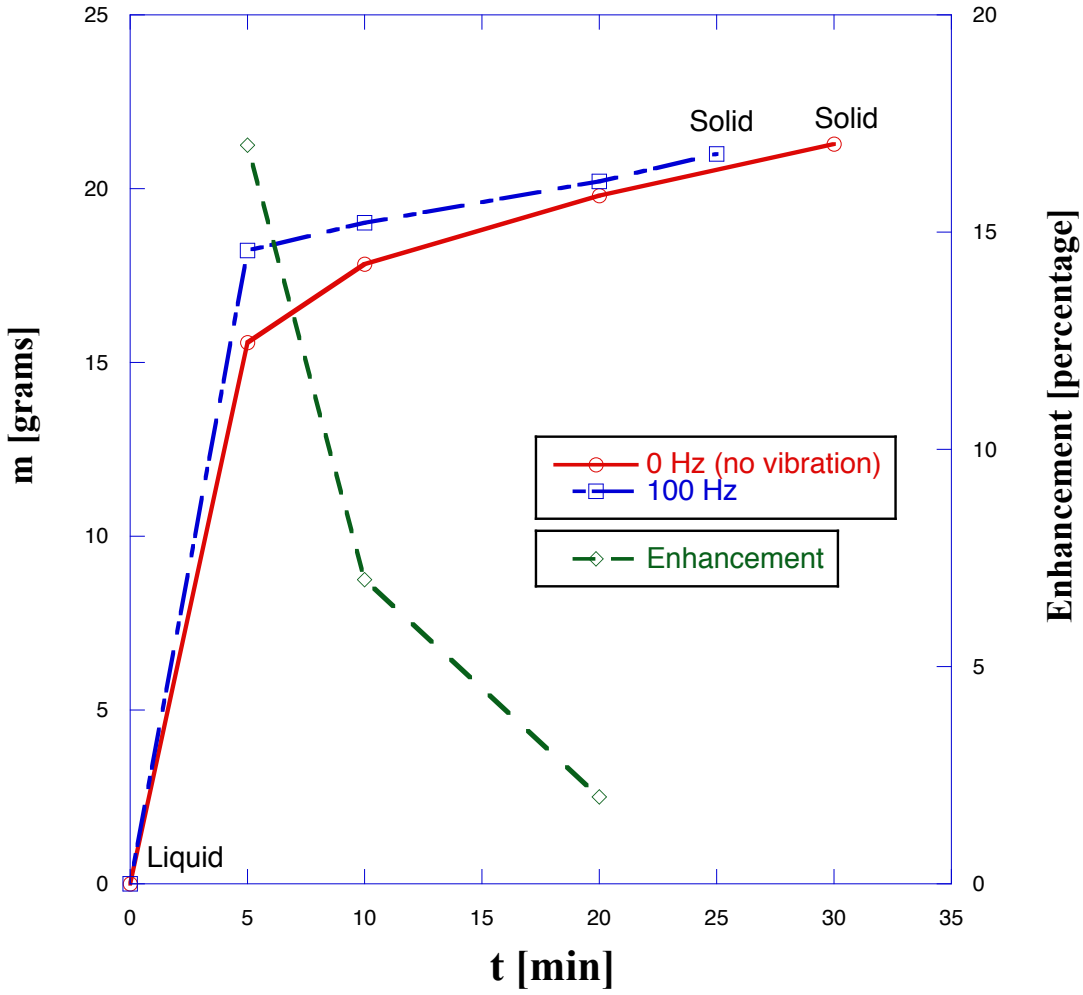

Figure 2.3: Average mass of solid paraffin wax formed versus time for no vibration and vibration frequency of 100 Hz.

In Figure 2.3, the enhancement line shows the difference between the mass formed with and without vibration, presented in the last column of Table 2.4. The results from Table 2.4 show there was more heat transfer with vibration, and an overall 17% improvement in solidification time calculated using Equation 5 and the final solidification times.

© University of Pretoria

In Table 2.4 it is also shown how the enhancement decreased per time step, which is also clear from Figure 2.3 because as the two lines representing solidification under vibration and without vibration get closer. The final difference between the two solidified masses of 21.29 g and 21.00 g, which is 0.29 g, shown in Table 2.4, is due to the initial amounts of liquid paraffin wax that were not exactly the same.

As the enhancement decays show in Table 2.4 and Figure 2.3, it never reaches zero. This means there is always more solidified paraffin wax formed under vibration than without. The significance of the decay may be attributed to the amount of liquid and solid in the sample. There are two suggested reasons for the decay. The first reason is because more solid was formed, the wall temperature had to be higher or equal than the thermal bath because it has only reached solid state, and also the liquid surface boundary was reduced, further decreasing heat transfer to the surroundings. The second considers the three layers during solidification, the solid, the liquid and the mushy layer. During solidification the solid layer increases, and thus the other two layers, the liquid and mushy layer, decrease. Since the effects of vibration happen in the liquid and mushy layer, it would make sense that as these layers get smaller the decay would also be affected.

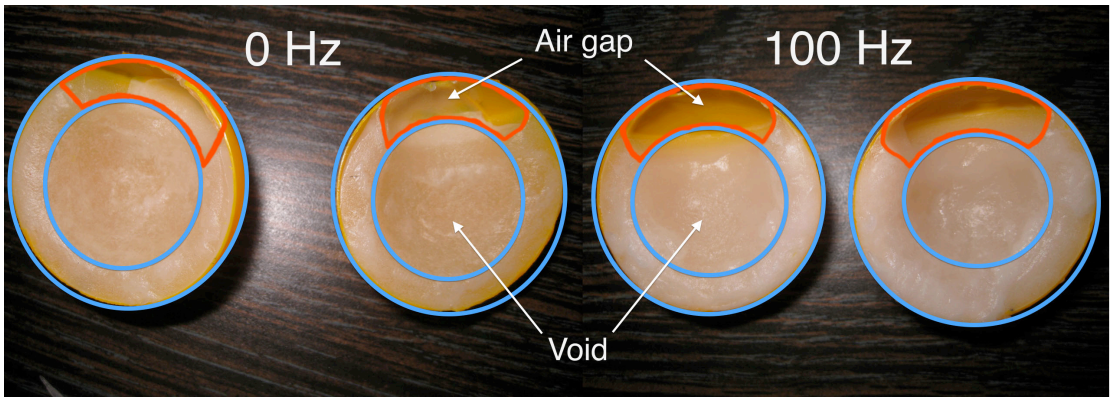

Figure 2.4: Solidified paraffin wax samples cut in half after 5 min for 0 Hz (no vibration) and 100Hz (with vibration), with the blue outline indicating the average wall thickness of the solidified paraffin wax and the centre void, and the red outline indicating the air gap.

Figure 2.4 shows the paraffin wax solidified after 5 minutes without vibration and with a vibration frequency of 100 Hz. The outside blue line indicates the plastic sphere boundary, and the inside blue line indicates the void in the centre. The paraffin wax

© University of Pretoria

solidified between the two blue lines is shown, excluding the air gap at the top identified with a red line. Measurements of the average wall thickness of the solidified paraffin wax were taken and the results show approximately 2 – 3 mm ± 0.1 mm difference between the two samples, with the larger average wall thickness being that of the vibrated sample at 100 Hz.

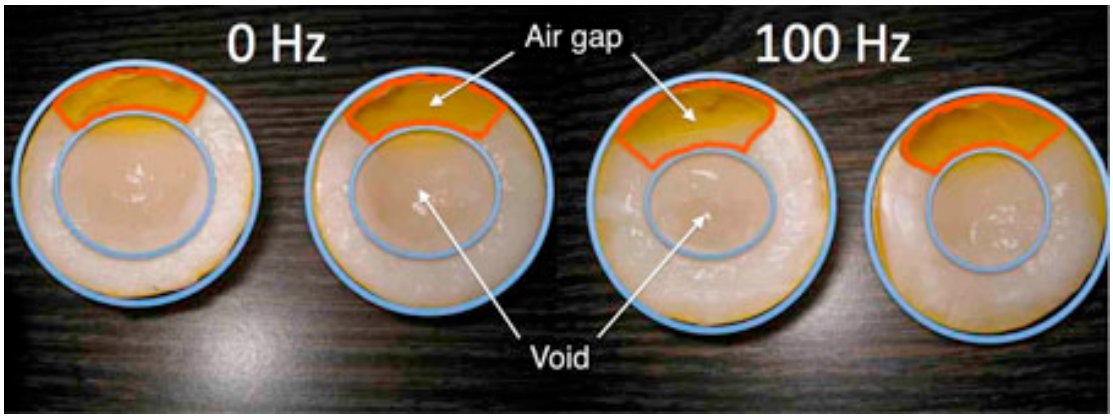

Figure 2.5: Solidified paraffin wax samples cut in half after 10 min for 0 Hz (no vibration) and 100Hz (with vibration), with the blue outline indicating the average wall thickness of the solidified paraffin wax and the centre void, and the red outline indicating the air gap.

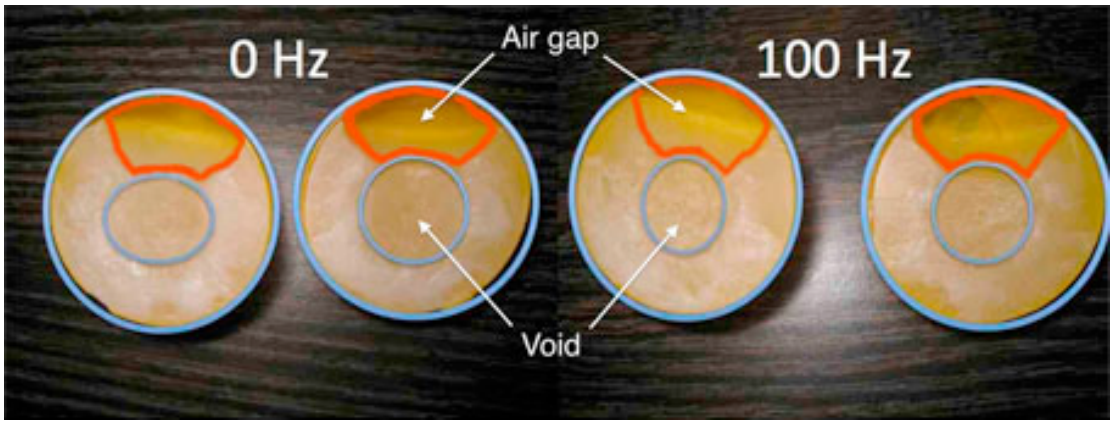

Figure 2.6: Solidified paraffin wax samples cut in half after 20 min for 0 Hz (no vibration) and 100Hz (with vibration), with the blue outline indicating the average wall thickness of the solidified paraffin wax and the centre void, and the red outline indicating the air gap.

Figures 2.5 and 2.6 show the paraffin wax solidified after 10 minutes and 20 minutes without vibration and with a vibration frequency of 100 Hz respectivaly. Measurements of the average wall thickness of the solidified paraffin wax were taken and the results

© University of Pretoria

show a difference of approximately 2 – 2.5 mm ± 0.1 mm after 10 minutes (Figure 2.5) and 1.5 – 2 mm ± 0.1 mm after 20 minutes (Figure 2.6) between the two samples, with the larger average wall thickness being that of the vibrated sample at 100 Hz.

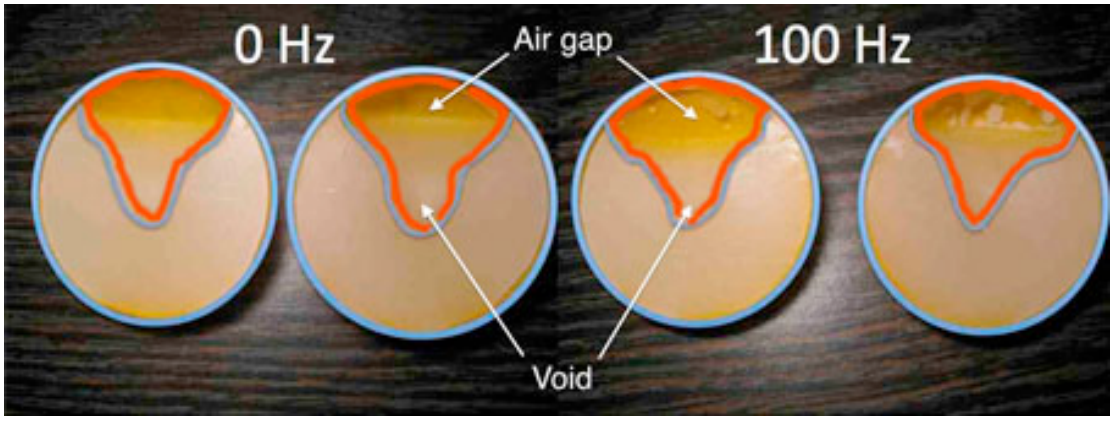

Figure 2.7: Solidified paraffin wax samples cut in half after 30 min for 0 Hz (no vibration) and 25 minutes for 100Hz (with vibration), with the blue outline indicating the void geometry formed, and the red outline indicating the air gap.

The final solidification time shown in Figure 2.7 shows the samples after 30 minutes without vibration and 25 minutes with vibration frequency of 100 Hz. It can be observed that although the void was still present in Figure 7 when there was vibration, it is very similar to the void formed without vibration. This is confirmed by the density calculations done in Table 2.1. This means that the voids were geometrically of the same size.

The samples in Figures 2.4 – 2.7 are one set of five done. The other four sets of experiments were done to check for repeatability. These results are shown in Table 2.2 and Table 2.3 for five samples each.

2.4 Experimental conclusions

It was found from experiments that the average densities of the paraffin wax samples were not affected by vibration during solidification. The experimental results indicate that imposing vibrations causes a faster solidification, i.e. the mass of solid produced at a fixed time after starting the solidification process increases due to the imposed vibration. This may be the result of two possible mechanisms. The first mechanism might be due to a mass transfer process by which more nuclei of solid particles are created due to the

© University of Pretoria

vibrations and these nuclei are more homogeneously distributed around the cooling front. The second mechanism possible mechanism is via a more efficient convection process in the mushy layer possibly causing “thermal resonances” which might enhance the heat transfer and shorten the solidification time. The objective of the following theoretical study is investigating and testing the second possibility, i.e. that heat transfer enhancement via convection in the mushy layer occurred due to vibration.

© University of Pretoria

CHAPTER 3

PROBLEM FORMULATION – THEORETICAL

3.1 Objective of the theoretical analysis

This chapter focuses on the effect of natural convection on the heat transfer and the solidfication process based on a theoretical analysis. A simplified theoretical model was established for the two-dimensional (2D) convection in a horizontal porous (mushy) layer under local thermal equilibrium condition. The problem under consideration is herein a 2D rectangular domain heated from below and cooled from above subject to acceleration of gravity as well as imposed vibrations. The left and right boundaries of the rectangular domain were considered to be adiabatic and the acceleration due to vibration is imposed in the vertical direction. Analysing the different regimes and their corresponding dynamics leads to the evaluation of the Nusselt number that provides an answer to how the heat transfer is affected by the vibrations.

3.2 Assumptions

Two-dimensional convection in a horizontal porous layer is assumed based on the observation that convection in the form of longitudinal rolls is apparently the dominant plane form (other geometries would have their own independent formulations). Local thermal equilibrium between the solid and fluid phases in the porous layer is assumed on account that locally the average fluid and solid temperatures are very close. The truncation of the spatial modes in the spectral method adopted forms the most serious assumption. No work has been done so far showing the limits of such an assumption in terms of the dimensionless groups involved. It is estimated that it might produce quantitatively accurate results for Rayleigh numbers as far as 12 times the convection onset value and qualitatively good results for Rayleigh numbers as far as 50 times the convection onset value.

3.3 Governing equations

The set of governing equations for natural convection in a fluid-saturated porous medium subject to local thermal equilibrium is presented initially for the common case of natural convection due to gravity in the absence of the additional acceleration due to vibrations, followed by its specific application to the problem at hand. Local thermal

© University of Pretoria

equilibrium implies that the temperature difference between the solid and fluid phases in a representative elementary volume (REV) is extremely small and therefore negligible. By applying the Boussinesq approximation stating that the density may be assumed constant (say ρ_o) everywhere except for the buoyancy (gravity) term in the Darcy equation, one may obtain the equations governing the natural convection problem in porous media subject to local thermal equilibrium. These are the continuity and the extended Darcy equations for the fluid flow, the energy equation for the heat transfer in the medium, and an equation of state relating the fluid's density to its temperature for which a linear approximation is deemed sensible and sufficient, as follows

$$\nabla_* \cdot \boldsymbol{V}_* = 0 \tag{1}$$

$$\frac{\rho_o}{\varphi}\frac{K}{\mu}\frac{\partial \boldsymbol{V}_*}{\partial t_*} + \boldsymbol{V}_* = -\frac{K}{\mu}\left[\nabla_* p_* + \rho_* g \nabla_*\left(\hat{\boldsymbol{e}}_{\boldsymbol{g}} \cdot \boldsymbol{X}_*\right)\right] \tag{2}$$

$$\gamma_e \frac{\partial T_*}{\partial t_*} + \gamma_f \boldsymbol{V}_* \cdot \nabla_* T_* = k_e \nabla_*^2 T_* \tag{3}$$

$$\rho_* = \rho_o\left[1 - \beta_*\left(T_* - T_C\right)\right] \tag{4}$$

where $\gamma_e = \varphi(\rho_o c_p)_f + (1-\varphi)(\rho_{s*}c)_s$, $\gamma_f = (\rho_o c_p)_f$, $k_e = \varphi k_f + (1-\varphi)k_s$ and the position vector $\boldsymbol{X}_*$ to any point in the porous domain, is defined by $\boldsymbol{X}_* = x_*\hat{\boldsymbol{e}}_x + y_*\hat{\boldsymbol{e}}_y + z_*\hat{\boldsymbol{e}}_z$, where $\hat{\boldsymbol{e}}_x, \hat{\boldsymbol{e}}_y, \hat{\boldsymbol{e}}_z$ are unit vectors in the $x-, y-$ and $z-$directions, respectively. Note that $\nabla_*\left(\hat{\boldsymbol{e}}_{\boldsymbol{g}} \cdot \boldsymbol{X}_*\right) = \hat{\boldsymbol{e}}_{\boldsymbol{g}}$, where $\hat{\boldsymbol{e}}_{\boldsymbol{g}}$ is a unit vector in the direction of the acceleration due to gravity. The gradient form is used for a certain purpose that will become clear shortly. The other symbols represent as follows: $\boldsymbol{V}_*$ is the filtration velocity; T_* is the temperature of the fluid and solid phases assumed equal due to the local thermal equilibrium assumption; ρ_* is the fluid's density; K is the permeability; μ is the dynamic viscosity; φ is porosity; $(\rho_* c_p)_f$ and $(\rho_{s*}c)_s$ are the heat capacities of the fluid and solid, respectively; γ_{e*} is the effective heat capacity of the medium; k_f and k_s are the thermal conductivities of the fluid and solid, respectively; and k_e is the effective thermal conductivity of the medium. The coefficient β_* is the thermal expansion coefficient defined by $\beta_* = -\left(\partial\rho_*/\partial T_*\right)/\rho_*$, T_C is a constant reference value of temperature and ρ_o is a constant reference value of the fluid's density.

Equation (2) can be further developed in the form

© University of Pretoria

$$\frac{\rho_o}{\varphi}\frac{K}{\mu}\frac{\partial \boldsymbol{V}_*}{\partial t_*}+\boldsymbol{V}_*=-\frac{K}{\mu}\left[\nabla_* p_*-\nabla_*\left(\rho_o g\,\hat{\boldsymbol{e}}_{\boldsymbol{g}}\cdot\boldsymbol{X}_*\right)-\left(\rho_*-\rho_o\right)g\nabla_*\left(\hat{\boldsymbol{e}}_{\boldsymbol{g}}\cdot\boldsymbol{X}_*\right)\right] \tag{5}$$

where ρ_o is the constant reference value of density. By introducing the following definition of the reduced pressure $p_{r*}=p_*-\rho_o g\,\hat{\boldsymbol{e}}_{\boldsymbol{g}}\cdot\boldsymbol{X}_*$ into equation (5), one obtains

$$\frac{\rho_o}{\varphi}\frac{K}{\mu}\frac{\partial \boldsymbol{V}_*}{\partial t_*}+\boldsymbol{V}_*=-\frac{K}{\mu}\left[\nabla_* p_{r*}-\left(\rho_*-\rho_o\right)g\nabla_*\left(\hat{\boldsymbol{e}}_{\boldsymbol{g}}\cdot\boldsymbol{X}_*\right)\right] \tag{6}$$

Transforming these equations into dimensionless form can be accomplished by introducing l_c, l_c^2/α_e, $\tilde{\alpha}_e/l_c$, ΔT_c, $\mu\tilde{\alpha}_e/K$, and ρ_o as the characteristic values of length, time, filtration velocity, temperature difference, pressure and density, while T_C is a constant reference value of temperature. As a result, the following dimensionless variables emerge:

$$\boldsymbol{X}=\frac{\boldsymbol{X}_*}{l_c}\;;\;\tilde{t}=\frac{t_*\alpha_e}{l_c^2}\;;\;\boldsymbol{V}=\frac{\boldsymbol{V}_* l_c}{\tilde{\alpha}_e}\;;\;p=\frac{p_{r*}K}{\mu\tilde{\alpha}_e}\;;\;\rho=\frac{\rho_*}{\rho_o}\;;\;T=\frac{\left(T_*-T_C\right)}{\Delta T_c} \tag{7}$$

where $\alpha_f=k_f/(\rho_* c_p)_f$ is the fluid phase thermal diffusivity; $\alpha_e=k_e/(\rho_* c_p)_e$ is the effective thermal diffusivity; $\tilde{\alpha}_e=\alpha_e\left(\gamma_e/\gamma_f\right)=\alpha_e/M_f=k_e/\gamma_f$ (where $M_f=\gamma_f/\gamma_e$) is a modified effective thermal diffusivity; and

$$\Delta T_c=\begin{cases}\left(T_H-T_C\right) & \text{when constant temperatures are imposed on two boundaries}\\ \dfrac{q_o l_c}{k_f} & \text{when a constant heat flux is imposed on one boundary and constant temperature on another boundary}\end{cases} \tag{8}$$

By using the definitions presented in equation (7), it becomes possible to transform the governing equations (1), (6) and (4) into the following dimensionless form:

$$\nabla\cdot\boldsymbol{V}=0 \tag{9}$$

$$\frac{Da}{\varphi Pr}\frac{\partial \boldsymbol{V}}{\partial \tilde{t}}+\boldsymbol{V}=-\nabla p+\left(\rho-1\right)G\nabla\left(\hat{\boldsymbol{e}}_{\boldsymbol{g}}\cdot\boldsymbol{X}\right) \tag{10}$$

$$\rho=1-\beta T_f \tag{11}$$

where the following dimensionless groups emerge:

$$G=\frac{g K l_c}{\tilde{\alpha}_e\nu}\;;\;\beta=\beta_*\Delta T_c\;;\;Da=\frac{K}{l_c^2}\;;\;Pr=\frac{\nu}{\alpha_f} \tag{12}$$

the last two being the Darcy and Prandtl numbers, while the kinematic viscosity is defined in the form $\nu=\mu/\rho_o$. From (11) $\left(\rho-1\right)=-\beta T$, which upon substitution into (10) yields

© University of Pretoria

$$\frac{1}{Pr_D}\frac{\partial \boldsymbol{V}}{\partial \tilde{t}} + \boldsymbol{V} = -\nabla p - Ra\, T\, \hat{\boldsymbol{e}}_g \tag{13}$$

by re-introducing explicitly $\hat{\boldsymbol{e}}_g$ by using the identity $\nabla\left(\hat{\boldsymbol{e}}_g \cdot \boldsymbol{X}\right) = \hat{\boldsymbol{e}}_g$, the Darcy-Prandtl number $Pr_D = \varphi Pr/Da$ emerged for the combination of the dimensionless groups Darcy and Prandtl numbers and porosity, and the Rayleigh number emerged as a combined dimensionless group $Ra = \beta G$, explicitly defined in the form

$$Ra = \frac{\beta_* \Delta T_c\, g\, K\, l_c}{\tilde{\alpha}_e \nu} \tag{14}$$

Equation (3) is then transformed into the following dimensionless form:

$$\frac{\partial T}{\partial \tilde{t}} + \boldsymbol{V} \cdot \nabla T = \nabla^2 T \tag{15}$$

The problem considered here refers to a two-dimensional rectangular domain heated from below (or cooled from above) subject to accelerations due to gravity and imposed vibrations as presented in Figure 3.1. The acceleration due to vibration is imposed in the vertical direction and can be expressed in the form

$$a_{v*} = A_{v*} \sin\left(\omega_* t_*\right) \tag{16}$$

where A_{v*} is the vibrational acceleration amplitude. A_{v*} can be expressed in relation to the acceleration due to gravity, in the form

$$A_{v*} = \delta g \tag{17}$$

In this way δ representing the dimensionless vibrational amplitude can be expressed in the form of how many *g*'s it imposes on the porous domain. Therefore

$$a_{v*} = \delta g \sin\left(\omega_* t_*\right) \tag{18}$$

Transforming the argument in (18) into a dimensionless form by using the characteristic time introduced in equation (7), yields the definition of the dimensionless vibration frequency in the form

$$\tilde{\omega} = \frac{\omega_* l_c^2}{\alpha_e} \tag{19}$$

and equation (18) becomes

$$a_{v*} = \delta g \sin\left(\tilde{\omega} \tilde{t}\right) \tag{20}$$

© University of Pretoria

By including the additional term related to the acceleration due to vibrations into equation (6), replaces each occurrence of g with $\left(g+a_{v*}\right)=g\left[1+\delta\sin\left(\tilde{\omega}\tilde{t}\right)\right]$ leading to the following form that replaces equation (13):

$$\frac{1}{Pr_D}\frac{\partial \boldsymbol{V}}{\partial \tilde{t}}+\boldsymbol{V}=-\nabla p-Ra\,T\left[1+\delta\sin\left(\tilde{\omega}\tilde{t}\right)\right]\hat{\boldsymbol{e}}_g \tag{21}$$

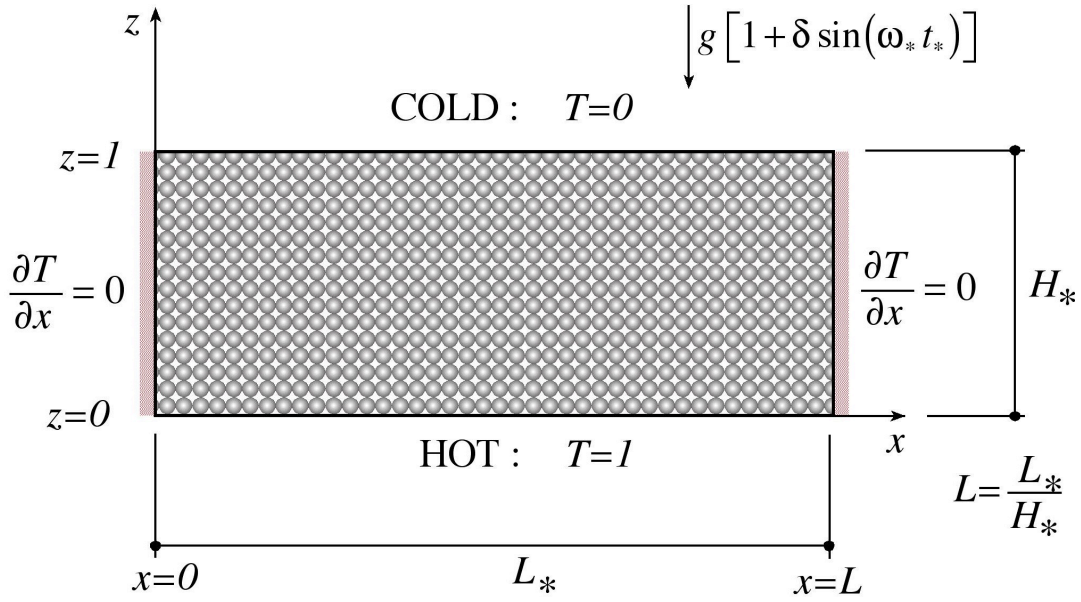

Figure 3.1: A two-dimensional rectangular domain heated from below (or cooled from above) subject to accelerations due to gravity and imposed vibrations.

The aspect ratio of the domain is defined by $L=L_*/H_*$. For a two-dimensional flow ($v=0$) one may introduce the definition of the stream-function ψ in the form

$$u=\frac{\partial \psi}{\partial z}\;;\; w=-\frac{\partial \psi}{\partial x} \tag{22}$$

to transform the dimensionless equations (15) and (21) into two coupled equations for the stream-function and temperature as follows

$$\left[\frac{1}{Pr_D}\frac{\partial}{\partial \tilde{t}}+1\right]\nabla^2\psi+Ra\left[1+\delta\sin\left(\tilde{\omega}\tilde{t}\right)\right]\frac{\partial T}{\partial x}=0 \tag{a}$$

(23)

$$\frac{\partial T}{\partial \tilde{t}}+\frac{\partial \psi}{\partial z}\frac{\partial T}{\partial x}-\frac{\partial \psi}{\partial x}\frac{\partial T}{\partial z}=\nabla^2 T \tag{b}$$

© University of Pretoria

3.4 Transformation into the spectral equations in space

The stream function and temperature are separated into a basic conduction part and a variation convection one in the form

$$\psi = \underbrace{\psi_B}_{=0} + \psi_V = \psi_V \qquad \text{(a)}$$

$$T = \underbrace{T_B}_{=1-z} + T_V = 1 - z + T_V \qquad \text{(b)} \qquad (24)$$

Substituting (24) into (23) yields

$$\left[\frac{1}{Pr_D}\frac{\partial}{\partial \tilde{t}} + 1\right]\nabla^2\psi_V + Ra\left[1 + \delta\sin\left(\tilde{\omega}\tilde{t}\right)\right]\frac{\partial T_V}{\partial x} = 0 \qquad \text{(a)}$$

$$\frac{\partial T_V}{\partial t} + \frac{\partial \psi_V}{\partial z}\frac{\partial T_V}{\partial x} + \frac{\partial \psi_V}{\partial x} - \frac{\partial \psi_V}{\partial x}\frac{\partial T_V}{\partial z} = \nabla^2 T_V \qquad \text{(b)} \qquad (25)$$

Considering the truncated expansion

$$\psi_V = A_{11}\sin\left(\frac{\pi x}{L}\right)\sin\left(\pi z\right) \qquad \text{(a)}$$

$$T_V = B_{11}\cos\left(\frac{\pi x}{L}\right)\sin\left(\pi z\right) + B_{02}\sin\left(2\pi z\right) \qquad \text{(b)} \qquad (26)$$

This representation is equivalent to a Galerkin expansion of the solution in both the $x-$ and $z-$ directions, truncated when $(i+j)=2$, where i is the Galerkin summation index in the $x-$direction while j is the Galerkin summation index in the $z-$direction.

Then, from (26), one can perform the derivatives

$$\nabla^2\psi_V = -\frac{\pi^2}{L^2}A_{11}\sin\left(\frac{\pi x}{L}\right)\sin\left(\pi z\right) - \pi^2 A_{11}\sin\left(\frac{\pi x}{L}\right)\sin\left(\pi z\right) =$$
$$-\pi^2\left(\frac{1}{L^2}+1\right)A_{11}\sin\left(\frac{\pi x}{L}\right)\sin\left(\pi z\right)$$

$$\frac{\partial \psi_V}{\partial z} = \pi A_{11}\sin\left(\frac{\pi x}{L}\right)\cos\left(\pi z\right)$$

$$\frac{\partial \psi_V}{\partial x} = \frac{\pi}{L}A_{11}\cos\left(\frac{\pi x}{L}\right)\sin\left(\pi z\right)$$

© University of Pretoria

(27)

$$\frac{\partial T_V}{\partial x} = -\frac{\pi}{L} B_{11} \sin\left(\frac{\pi x}{L}\right) \sin(\pi z)$$

$$\frac{\partial T_V}{\partial z} = \pi B_{11} \cos\left(\frac{\pi x}{L}\right) \cos(\pi z) + 2\pi B_{02} \cos(2\pi z)$$

$$\nabla^2 T_V = -\pi^2 \left(\frac{1}{L^2} + 1\right) B_{11} \cos\left(\frac{\pi x}{L}\right) \sin(\pi z) - 4\pi^2 B_{02} \sin(2\pi z)$$

Substituting (26) into equation (25)a by using the expressions for the derivatives from (27), yields

$$-\left[\frac{1}{Pr_D}\frac{d}{d\tilde{t}} + 1\right]\left[\pi^2\left(\frac{1}{L^2}+1\right) A_{11} \sin\left(\frac{\pi x}{L}\right)\sin(\pi z)\right] - Ra\left[1+\delta\sin(\tilde{\omega}\tilde{t})\right]\left[\frac{\pi}{L}B_{11}\right]\sin\left(\frac{\pi x}{L}\right)\sin(\pi z) = 0$$

which upon definition of $1/\gamma = 1/L^2 + 1$ can be grouped in the form

$$\left\{\frac{\pi^2}{\gamma}\left[\frac{1}{Pr_D}\frac{d}{d\tilde{t}} + 1\right] A_{11} + \frac{\pi\, Ra}{L}\left[1+\delta\sin(\tilde{\omega}\tilde{t})\right] B_{11}\right\} \sin\left(\frac{\pi x}{L}\right)\sin(\pi z) = 0$$

or in the expanded form

$$\left\{\frac{\pi^2}{\gamma\, Pr_D}\frac{d\, A_{11}}{d\tilde{t}} + \frac{\pi^2}{\gamma} A_{11} + \frac{\pi\, Ra}{L}\left[1+\delta\sin(\tilde{\omega}\tilde{t})\right] B_{11}\right\} \sin\left(\frac{\pi x}{L}\right)\sin(\pi z) = 0 \qquad (28)$$

where

$$\frac{1}{\gamma} = \frac{1}{L^2} + 1 \quad \text{or} \quad \gamma = \frac{L^2}{L^2+1}$$

The non-linear terms $(\partial\psi_V/\partial z)(\partial T_V/\partial x)$ and $(\partial\psi_V/\partial x)(\partial T_V/\partial z)$ in equation (25)b are evaluated from (27) in the form

$$\frac{\partial\psi_V}{\partial z}\frac{\partial T_V}{\partial x} = -\frac{\pi^2}{L} A_{11} B_{11} \sin^2\left(\frac{\pi x}{L}\right) \sin(\pi z)\cos(\pi z) = -\frac{\pi^2}{2L} A_{11} B_{11} \sin^2\left(\frac{\pi x}{L}\right) \sin(2\pi z)$$

and

$$\frac{\partial\psi_V}{\partial x}\frac{\partial T_V}{\partial z} = \frac{\pi^2}{L} A_{11} B_{11} \cos^2\left(\frac{\pi x}{L}\right) \sin(\pi z)\cos(\pi z) + \frac{2\pi^2}{L} A_{11} B_{02} \cos\left(\frac{\pi x}{L}\right) \sin(\pi z)\cos(2\pi z) =$$

$$\frac{\pi^2}{2L} A_{11} B_{11} \cos^2\left(\frac{\pi x}{L}\right) \sin(2\pi z) + \frac{2\pi^2}{L} A_{11} B_{02} \cos\left(\frac{\pi x}{L}\right) \frac{1}{2}\left[-\sin(\pi z) + \sin(3\pi z)\right] =$$

$$\frac{\pi^2}{2L} A_{11} B_{11} \cos^2\left(\frac{\pi x}{L}\right) \sin(2\pi z) - \frac{\pi^2}{L} A_{11} B_{02} \cos\left(\frac{\pi x}{L}\right) \sin(\pi z) + \frac{\pi^2}{L} A_{11} B_{02} \cos\left(\frac{\pi x}{L}\right) \sin(3\pi z)$$

Therefore, the form, which appears in (25)b is

© University of Pretoria

$$\frac{\partial \psi_V}{\partial z}\frac{\partial T_V}{\partial x}-\frac{\partial \psi_V}{\partial x}\frac{\partial T_V}{\partial z}=-\frac{\pi^2}{2L}A_{11}B_{11}\sin^2\left(\frac{\pi x}{L}\right)\sin(2\pi z)-\frac{\pi^2}{2L}A_{11}B_{11}\cos^2\left(\frac{\pi x}{L}\right)\sin(2\pi z)$$
$$+\frac{\pi^2}{L}A_{11}B_{02}\cos\left(\frac{\pi x}{L}\right)\sin(\pi z)-\frac{\pi^2}{L}A_{11}B_{02}\cos\left(\frac{\pi x}{L}\right)\sin(3\pi z)=$$
$$-\frac{\pi^2}{2L}A_{11}B_{11}\underbrace{\left[\sin^2\left(\frac{\pi x}{L}\right)+\cos^2\left(\frac{\pi x}{L}\right)\right]}_{=1}\sin(2\pi z)+\frac{\pi^2}{L}A_{11}B_{02}\cos\left(\frac{\pi x}{L}\right)\sin(\pi z)-$$
$$\frac{\pi^2}{L}A_{11}B_{02}\cos\left(\frac{\pi x}{L}\right)\sin(3\pi z)$$

(29)

Substituting now (29) and (27) into (25)b yields

$$\overbrace{\frac{\mathrm{d}B_{11}}{\mathrm{d}\tilde{t}}\cos\left(\frac{\pi x}{L}\right)\sin(\pi z)}^{A}+\overbrace{\frac{\mathrm{d}B_{02}}{\mathrm{d}\tilde{t}}\sin(2\pi z)}^{O}-\overbrace{\frac{\pi^2}{2L}A_{11}B_{11}\sin(2\pi z)}^{O}+\overbrace{\frac{\pi^2}{L}A_{11}B_{02}\cos\left(\frac{\pi x}{L}\right)\sin(\pi z)}^{A}-$$
$$\overbrace{\frac{\pi^2}{L}A_{11}B_{02}\cos\left(\frac{\pi x}{L}\right)\sin(3\pi z)}^{A}+\overbrace{\frac{\pi}{L}A_{11}\cos\left(\frac{\pi x}{L}\right)\sin(\pi z)}^{A}=$$
$$-\overbrace{\frac{\pi^2}{\gamma}B_{11}\cos\left(\frac{\pi x}{L}\right)\sin(\pi z)}^{A}-\overbrace{4\pi^2B_{02}\sin(2\pi z)}^{O}$$

Grouping likewise terms leads to

$$\left[\frac{\mathrm{d}B_{11}}{\mathrm{d}\tilde{t}}+\frac{\pi^2}{L}A_{11}B_{02}+\frac{\pi}{L}A_{11}+\frac{\pi^2}{\gamma}B_{11}\right]\cos\left(\frac{\pi x}{L}\right)\sin(\pi z)+\left[\frac{\mathrm{d}B_{02}}{\mathrm{d}\tilde{t}}-\frac{\pi^2}{2L}A_{11}B_{11}+4\pi^2B_{02}\right]\sin(2\pi z)-$$
$$\frac{\pi^2}{L}A_{11}B_{02}\cos\left(\frac{\pi x}{L}\right)\sin(3\pi z)=0$$

(30)

Summarising the resulting equations (28) and (30) in the form

$$\left\{\frac{\pi^2}{\gamma\,Pr_D}\frac{d\,A_{11}}{d\,\tilde{t}}+\frac{\pi^2}{\gamma}A_{11}+\frac{\pi\,Ra}{L}\left[1+\delta\sin(\tilde{\omega}t)\right]B_{11}\right\}\sin\left(\frac{\pi x}{L}\right)\sin(\pi z)=0 \qquad \text{(a)}$$

(31)

$$\left[\frac{\mathrm{d}B_{11}}{\mathrm{d}\tilde{t}}+\frac{\pi^2}{L}A_{11}B_{02}+\frac{\pi}{L}A_{11}+\frac{\pi^2}{\gamma}B_{11}\right]\cos\left(\frac{\pi x}{L}\right)\sin(\pi z)+$$
$$\left[\frac{\mathrm{d}B_{02}}{\mathrm{d}\tilde{t}}-\frac{\pi^2}{2L}A_{11}B_{11}+4\pi^2B_{02}\right]\sin(2\pi z)-\underbrace{\frac{\pi^2}{L}A_{11}B_{02}\cos\left(\frac{\pi x}{L}\right)\sin(3\pi z)}_{\text{This term belongs to } (i+j)=4 \text{ and is beyond the modes considered here.}}=0 \qquad \text{(b)}$$

© University of Pretoria

Multiplying now equation (31)a by the corresponding eigenfunctions and integrating over the domain, i.e. $\int_0^L \mathrm{d}x \int_0^1 (\bullet)\,\mathrm{d}z$ produces a system of ordinary differential equations for the amplitudes $A_{11}(\tilde{t}), B_{11}(\tilde{t}), B_{02}(\tilde{t})$. Multiplying equation (31) by $\sin(\pi x/L)\sin(\pi z)$ and integrating while using the orthogonality relationships from Appendix A result in

$$\frac{L}{4}\left\{\frac{\pi^2}{\gamma\, Pr_D}\frac{d\,A_{11}}{d\,\tilde{t}} + \frac{\pi^2}{\gamma}A_{11} + \frac{\pi\, Ra}{L}\left[1+\delta\sin(\tilde{\omega}t)\right]B_{11}\right\} = 0 \tag{32}$$

Multiplying equation (31)b by $\cos\left(\frac{\pi x}{L}\right)\sin(\pi z)$ and integrating over the domain produce

$$\frac{L}{4}\left[\frac{\mathrm{d}\,B_{11}}{\mathrm{d}\,\tilde{t}} + \frac{\pi^2}{L}A_{11}B_{02} + \frac{\pi}{L}A_{11} + \frac{\pi^2}{\gamma}B_{11}\right] = 0 \tag{33}$$

Multiplying equation (31)b by $\sin(2\pi z)$ and integrating over the domain yield

$$\frac{L}{2}\left[\frac{\mathrm{d}\,B_{02}}{\mathrm{d}\,\tilde{t}} - \frac{\pi^2}{2L}A_{11}B_{11} + 4\pi^2 B_{02}\right] = 0 \tag{34}$$

The resulting equations are

$$\frac{L}{4}\left\{\frac{\pi^2}{\gamma\, Pr_D}\frac{d\,A_{11}}{d\,\tilde{t}} + \frac{\pi^2}{\gamma}A_{11} + \frac{\pi\, Ra}{L}\left[1+\delta\sin(\tilde{\omega}t)\right]B_{11}\right\} = 0 \tag{35}$$

$$\frac{L}{4}\left[\frac{\mathrm{d}\,B_{11}}{\mathrm{d}\,\tilde{t}} + \frac{\pi^2}{L}A_{11}B_{02} + \frac{\pi}{L}A_{11} + \frac{\pi^2}{\gamma}B_{11}\right] = 0 \tag{36}$$

$$\frac{L}{2}\left[\frac{\mathrm{d}\,B_{02}}{\mathrm{d}\,\tilde{t}} - \frac{\pi^2}{2L}A_{11}B_{11} + 4\pi^2 B_{02}\right] = 0 \tag{37}$$

By introducing for convenience the following notation:

$$\gamma = \frac{L^2}{L^2+1}\;;\quad \theta = \frac{L}{\gamma} = \frac{L^2+1}{L} \tag{38}$$

and by rescaling the time variable in the form

$$t = \frac{\pi^2}{\gamma}\tilde{t} \tag{39}$$

© University of Pretoria

one may present equations (35)-(37) after multiplying each one of them by γ/π^2 in the form

$$\frac{\gamma}{\pi^2}\frac{d\,A_{11}}{d\,\tilde{t}} = -\frac{Pr_D\gamma}{\pi^2}\left\{A_{11} + \frac{\gamma\,Ra}{L\pi}\left[1+\delta\sin\left(\tilde{\omega}\,\tilde{t}\right)\right]B_{11}\right\}$$

$$\frac{\gamma}{\pi^2}\frac{\mathrm{d}\,B_{11}}{\mathrm{d}\,\tilde{t}} = -\frac{\gamma}{\pi L}A_{11} - B_{11} - \frac{\gamma}{L}A_{11}B_{02}$$

$$\frac{\gamma}{\pi^2}\frac{\mathrm{d}\,B_{02}}{\mathrm{d}\,\tilde{t}} = -4\gamma B_{02} + \frac{\gamma}{2L}A_{11}B_{11}$$

to yield

$$\frac{L}{4}\left\{\frac{1}{Pr_D}\frac{d\,A_{11}}{d\,\tilde{t}} + A_{11} + \frac{Ra}{\pi\theta}\left[1+\delta\sin\left(\frac{\tilde{\omega}\tilde{t}\,\pi^2}{\gamma}\right)\right]B_{11}\right\} = 0 \qquad \text{(a)}$$

$$\frac{L}{4}\left[\frac{\mathrm{d}\,B_{11}}{\mathrm{d}\,\tilde{t}}\frac{L^2}{\pi^2\left(L^2+1\right)} + \frac{1}{\theta}A_{11}B_{02} + \frac{1}{\theta\pi}A_{11} + B_{11}\right] = 0 \qquad \text{(b)} \qquad (40)$$

$$\frac{L}{2}\left[\frac{\mathrm{d}\,B_{02}}{\mathrm{d}\,\tilde{t}}\frac{L^2}{\pi^2\left(L^2+1\right)} - \frac{1}{2\theta}A_{11}B_{11} + \frac{4L^2}{L^2+1}B_{02}\right] = 0 \qquad \text{(c)}$$

where the forcing vibration's frequency was also rescaled in (18a) in the form

$$\omega = \frac{\tilde{\omega}\,\gamma}{\pi^2} \qquad (41)$$

In the limit, when $\delta = 0$, i.e. without vibrations, the system has the following stationary (fixed) points $A_{11,f} = B_{11,f} = B_{02,f} = 0$, the trivial motionless conduction solution that is expected to be stable for $Ra < 4\pi^2$, and the following steady convective solution, which is expected to be stable for $4\pi^2 < Ra < Ra_0$

$$A_{11,f} = \mp\frac{2\sqrt{2}\gamma^{1/2}Ra^{1/2}}{\pi}\left[1-\frac{\pi^2\theta^2}{Ra}\right]^{1/2} \qquad \text{(a)}$$

$$B_{11,f} = \pm\frac{2\sqrt{2}\,L}{\gamma^{1/2}Ra^{1/2}}\left[1-\frac{\pi^2\theta^2}{Ra}\right]^{1/2} \qquad \text{(b)} \qquad (42)$$

$$B_{02,f} = \frac{\pi\theta^2}{Ra} - \frac{1}{\pi} = \frac{1}{\pi}\left[\frac{\pi^2\theta^2}{Ra} - 1\right] \qquad \text{(c)}$$

Rescaling the Rayleigh and Darcy Prandtl numbers in the form

© University of Pretoria

$$R = \frac{Ra}{\pi^2 \theta^2} \quad ; \quad \alpha = \frac{Pr_D \gamma}{\pi^2} \tag{43}$$

yields

$$A_{11,f} = \mp 2\sqrt{2}\underbrace{\gamma^{1/2}\theta}_{=L/\gamma^2} R^{1/2}\left[1-\frac{1}{R}\right]^{1/2} = \mp 2\sqrt{2}\,\gamma^{1/2}\theta\left(R-1\right)^{1/2} \tag{44}$$

$$B_{11,f} = \pm \frac{2\sqrt{2}\,\gamma^{1/2}}{\pi R^{1/2}}\left[1-\frac{1}{R}\right]^{1/2} = \pm \frac{2\sqrt{2}\,\gamma^{1/2}}{\pi R^{1/2}}\left[\frac{R-1}{R}\right]^{1/2} = \pm \frac{2\sqrt{2}\,\gamma^{1/2}}{\pi}\frac{\left(R-1\right)^{1/2}}{R} \tag{45}$$

$$B_{02,f} == \frac{1}{\pi}\left[\frac{1}{R}-1\right] = -\frac{\left(R-1\right)}{\pi R} \tag{46}$$

A first rescaling of the amplitudes is convenient for plotting the bifurcation diagrams

$$\tilde{A}_{11} = -\frac{A_{11}}{2\sqrt{2}\,\gamma^{1/2}\theta} \rightarrow \tilde{A}_{11,f} = \pm\left(R-1\right)^{1/2} \tag{a}$$

$$\tilde{B}_{11} = \frac{\pi B_{11}}{2\sqrt{2}\,\gamma^{1/2}} \rightarrow \tilde{B}_{11,f} = \pm\frac{\left(R-1\right)^{1/2}}{R} \tag{b}$$

$$\tilde{B}_{02} = -\pi B_{02} \rightarrow \tilde{B}_{02,f} = \frac{\left(R-1\right)}{R} \tag{c}$$

(47)

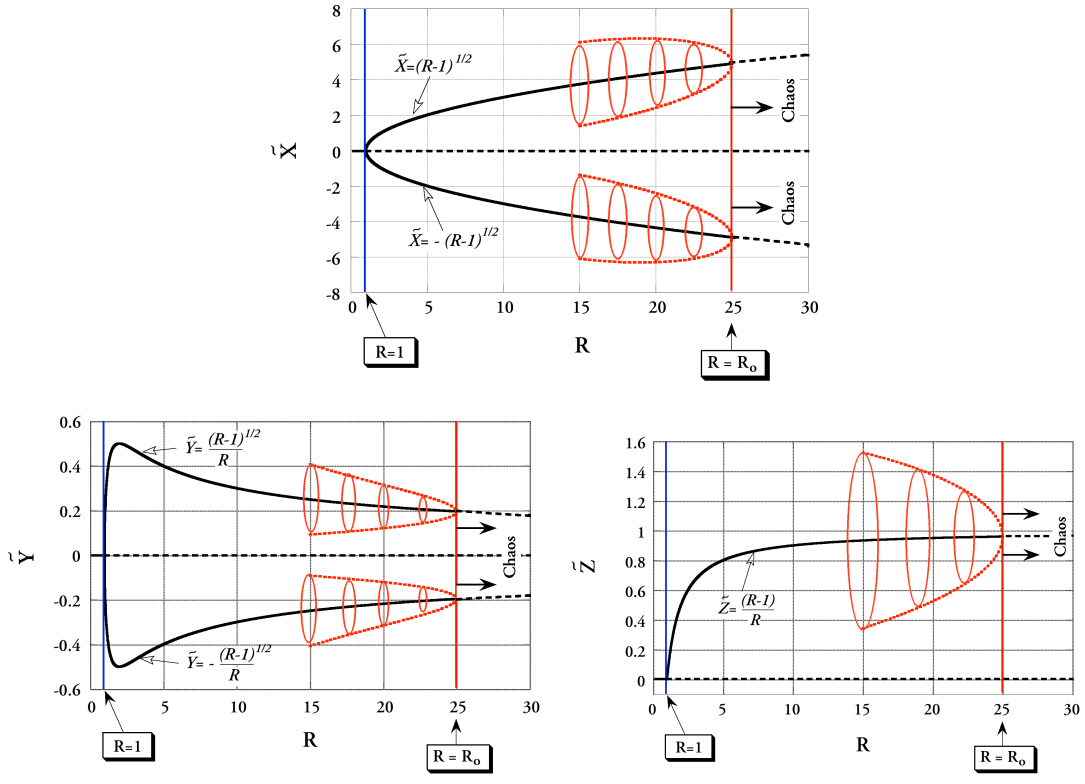

Figure 3.2: Bifurcation diagrams representing the fixed points (Vadasz, 2001)

© University of Pretoria

Rescaling again the amplitudes in a way that removes the explicit dependence of the fixed points on R in the form

$$X = -\frac{A_{11}}{2\sqrt{2}\,\gamma^{1/2}\theta\,(R-1)^{1/2}} \quad \rightarrow \quad A_{11} = -\,2\left[2\gamma(R-1)\right]^{1/2}\theta\,X \tag{48}$$

$$Y = \frac{\pi R\,B_{11}}{2\sqrt{2}\,\gamma^{1/2}(R-1)^{1/2}} \quad \rightarrow \quad B_{11} = \frac{2\left[2\gamma(R-1)\right]^{1/2}}{\pi R}\,Y \tag{49}$$

$$Z = -\frac{\pi R}{(R-1)}\,B_{02} \quad \rightarrow \quad B_{02} = -\frac{(R-1)}{\pi R}\,Z \tag{50}$$

The convective fixed points are now $X_f = \pm 1$, $Y_f = \pm 1$, $Z_f = 1$.

Substituting the rescaled amplitudes by using (47) into the equation (39), yields

$$-2\left[2\gamma(R-1)\right]^{1/2}\theta\,\frac{\mathrm{d}X}{\mathrm{d}t} = -\frac{Pr_D\gamma}{\pi^2}\left\{-2\left[2\gamma(R-1)\right]^{1/2}\theta X + 2\pi\theta R\,\frac{\left[2\gamma(R-1)\right]^{1/2}}{\pi R}\left[1+\delta\sin(\omega t)\right]Y\right\}$$

$$\frac{\mathrm{d}X}{\mathrm{d}t} = -\frac{Pr_D\gamma}{\pi^2}\left\{\frac{2\left[2\gamma(R-1)\right]^{1/2}\theta}{2\left[2\gamma(R-1)\right]^{1/2}\theta}X - \frac{2\pi\theta R\left[2\gamma(R-1)\right]^{1/2}}{2\left[2\gamma(R-1)\right]^{1/2}\theta\pi R}\left[1+\delta\sin(\omega t)\right]Y\right\}$$

$$\frac{\mathrm{d}X}{\mathrm{d}t} = -\frac{Pr_D\gamma}{\pi^2}\left\{X - \left[1+\delta\sin(\omega t)\right]Y\right\} \tag{51}$$

$$\frac{2\left[2\gamma(R-1)\right]^{1/2}}{\pi R}\frac{\mathrm{d}Y}{\mathrm{d}t} = -\frac{2\left[2\gamma(R-1)\right]^{1/2}}{\pi R}Y + \frac{2\left[2\gamma(R-1)\right]^{1/2}\theta}{\pi\theta}X - 2\left[2\gamma(R-1)\right]^{1/2}\frac{(R-1)}{\pi R}\frac{1}{}XZ$$

$$\frac{\mathrm{d}Y}{\mathrm{d}t} = -\frac{2\left[2\gamma(R-1)\right]^{1/2}\pi R}{2\left[2\gamma(R-1)\right]^{1/2}\pi R}Y + \frac{2\left[2\gamma(R-1)\right]^{1/2}\pi R}{2\left[2\gamma(R-1)\right]^{1/2}\pi}X - 2\left[2\gamma(R-1)\right]^{1/2}\frac{(R-1)\pi R}{2\left[2\gamma(R-1)\right]^{1/2}\pi R}XZ$$

$$\frac{\mathrm{d}Y}{\mathrm{d}t} = -Y + RX - (R-1)XZ \tag{52}$$

© University of Pretoria

$$-\frac{(R-1)}{\pi R}\frac{\mathrm{d}Z}{\mathrm{d}t}=-4\gamma\left[-\frac{(R-1)}{\pi R}\right]Z+\frac{1}{2\theta}\left\{-2\left[2\gamma(R-1)\right]^{1/2}\theta\right\}\frac{2\left[2\gamma(R-1)\right]^{1/2}}{\pi R}XY$$

$$-\frac{(R-1)}{\pi R}\frac{\mathrm{d}Z}{\mathrm{d}t}=4\gamma\frac{(R-1)}{\pi R}Z-\frac{2\left[2\gamma(R-1)\right]^{1/2}\theta}{2\theta}\frac{2\left[2\gamma(R-1)\right]^{1/2}}{\pi R}XY$$

$$-\frac{(R-1)}{\pi R}\frac{\mathrm{d}Z}{\mathrm{d}t}=4\gamma\frac{(R-1)}{\pi R}Z-4\gamma\frac{(R-1)}{\pi R}XY$$

$$-\frac{(R-1)}{\pi R}\frac{\mathrm{d}Z}{\mathrm{d}t}=4\gamma\frac{(R-1)}{\pi R}Z-4\gamma\frac{(R-1)}{\pi R}XY$$

$$-\frac{\mathrm{d}Z}{\mathrm{d}t}=4\gamma(Z-XY)$$

$$\frac{\mathrm{d}Z}{\mathrm{d}t}=4\gamma(XY-Z) \tag{53}$$

To summarise, the rescaled equations have the form

$$\dot{X}=-\alpha\left\{X-\left[1+\delta\sin(\omega t)\right]Y\right\} \tag{51}$$

$$\dot{Y}=-Y+RX-(R-1)XZ \tag{52}$$

$$\dot{Z}=4\gamma(XY-Z) \tag{53}$$

where the Newtonian notation for time derivatives was introduced in the form

$$\dot{X}=\frac{\mathrm{d}X}{\mathrm{d}t},\ \dot{Y}=\frac{\mathrm{d}Y}{\mathrm{d}t},\ \dot{Z}=\frac{\mathrm{d}Z}{\mathrm{d}t} \tag{54}$$

The controlling parameters are

$$R=\frac{Ra}{\pi^2\theta^2}\ ;\ \alpha=\frac{Pr_D\gamma}{\pi^2}\ ;\ \gamma=\frac{L^2}{L^2+1}\ ;\ \omega=\frac{\tilde{\omega}\gamma}{\pi^2} \tag{55}$$

and δ as the forcing vibration's amplitude.

Also, in (53) and (55), the following parameters and variables are defined:

$$\theta=\frac{L}{\gamma}=\frac{L^2+1}{L}\ ,\quad t=\frac{\pi^2}{\gamma}\tilde{t}\ , \tag{56}$$

$$X=-\frac{A_{11}}{2\sqrt{2}\,\gamma^{1/2}\theta\,(R-1)^{1/2}}\ ,\quad Y=\frac{\pi R\,B_{11}}{2\sqrt{2}\,\gamma^{1/2}(R-1)^{1/2}}\ ,\quad Z=-\frac{\pi R}{(R-1)}B_{02}$$

As $L\to\infty$ we obtain

© University of Pretoria

$\gamma = \lim_{L\to\infty} \frac{L^2}{L^2+1} = \lim_{L\to\infty} \frac{1}{1+\frac{1}{L^2}} = 1$ and $\theta \to L \to \infty$ so $R \to 0$ for any finite value of Ra

(If the assumption that $L \to \infty$ was relaxed then the modes would change, but the results would be similar). Therefore, for large values of L, i.e. $L >> 1$ one gets

$\gamma \sim 1$; $\theta \sim L$; $\alpha \sim \frac{Pr_D}{\pi^2}$; $t \sim \pi^2 \tilde{t}$ and $R \sim \frac{Ra}{\pi^2} L^{-2}$ as the approximations for $L >> 1$.

Large values of L produce finite values of R only for large values of Ra. In order for $R = O(1)$, the Rayleigh number has to be of the order of magnitude $Ra = O(L^2)$.

For the solution of the non-autonomous system (51), (52), (53), one introduces an additional dummy dependent variable

$$W = \omega t \tag{57}$$

transforming (51), (52), (53), into

$$\dot{X} = -\alpha(X - Y) + \alpha \delta Y \sin(W) \tag{58}$$

$$\dot{Y} = -Y + R X - (R-1) X Z \tag{59}$$

$$\dot{Z} = 4\gamma(XY - Z) \tag{60}$$

$$\dot{W} = \omega \tag{61}$$

3.5 Summary

A simplified theoretical model for natural convection heat transfer in a vibrating porous layer was derived in this chapter. The simplification to the dimensionless governing equations was obtained by assuming two-dimensional convection based on the observation that longitudinal rolls are apparently the dominant plane form. Local thermal equilibrium between the solid and fluid phases in the porous layer is assumed too, on account that locally the average fluid and solid temperature are very close. Then the truncation of the spatial modes via a spectral method was adopted to yield the equations governing the dynamics of the convection amplitudes that are time dependent. The stationary points of the resulting equations were identified and their dependence on the controlling parameters was analysed. Based on the identified stationary points the resulting equations were rescaled in a form that is convenient to be used in the following chapters.

© University of Pretoria

CHAPTER 4

THEORETICAL METHOD OF SOLUTION AND PRESENTATION

4.1 Numerical solution evaluated using Fortran

All the solutions for the amplitudes of stream function and temperature, as a function of time presented in the previous section were evaluated via Fortran programming, by using the subroutine DVERK by Hull et al. (1976) and applying a fifth- and sixth-order Runge-Kutta-Verner numerical method of solution. The main program calls subroutine DVERK to solve the specified system of ordinary differential equations.

The results are presented in graphs showing the amplitudes as a function of time as well as on phase diagrams (phase portraits) with the aim of identifying the different parameter regimes and possibly identifing the regimes that enhance the heat transfer.

In order to establish the stability type of the results and the type of attracting trajectory, the results were used to evaluate their corresponding Lyapunov exponents. Finally, in order to establish which parameter regimes cause a resulting heat transfer enhancement and which cause a heat transfer reduction when compared with the non-vibrating convection problem, the resulting Nusselt number was evaluated and presented as it varies with varying the value of the scaled Rayleigh number, R.

4.2 Graphical representation of the results

There is no need to explain the graphical results when presented in terms of the amplitudes versus time. However, when they are presented on phase diagrams, and in particular as projections on the three relevant planes on a three-dimensional phase diagram some explanation is required in order to avoid ambiguity in the interpretation of the results. In order to avoid ambiguity some simple artificially produced examples are presented first.

Assuming that $X(t)$, $Y(t)$ and $Z(t)$ are the amplitudes representing a dynamic system of differential equations then a solution of the form:

$$X = \sin(t)\,,\ Y = \cos(3t)\,,\ Z = \cos(t) \tag{62}$$

can be presented on a three-dimensional phase diagram where $X(t)$, $Y(t)$ and $Z(t)$ represent a point on this diagram for a given value of t. As the value of t changes, so the location of this point varies creating a **trajectory** of "motion" on the diagram. In any

© University of Pretoria

dynamical system two distinct trajectories cannot intersect, and any specific trajectory cannot intersect itself. These trajectories can be open i.e. they start at some point representing the initial conditions (the initial values of $X(0),Y(0)$ and $Z(0)$) and end for example at another point that may represent a possible steady state value of the system. In such a case the steady state is a stable fixed point of the system. Another possibility is that the trajectory is closed, in which case we anticipate usually a periodic motion. The example presented above belongs to such a periodic motion. A graph of this motion in the three dimensional space of the phase diagram is presented in Figure 4.1 where it is evident that the trajectory closes and therefore the motion is periodic. In this example the functions $X(t),Y(t)$ and $Z(t)$ are being given analytically so the periodic motion could have been anticipated from their analytical form, however when the results are being obtained from numerical solutions the one possible way to identify a periodic solution is from the phase diagram by observing whether a trajectory is closed.

In Figure 4.1 the vertical direction represents the z axis and the horizontal directions x and y correspond to a right-handed orthogonal Cartesian coordinate system.

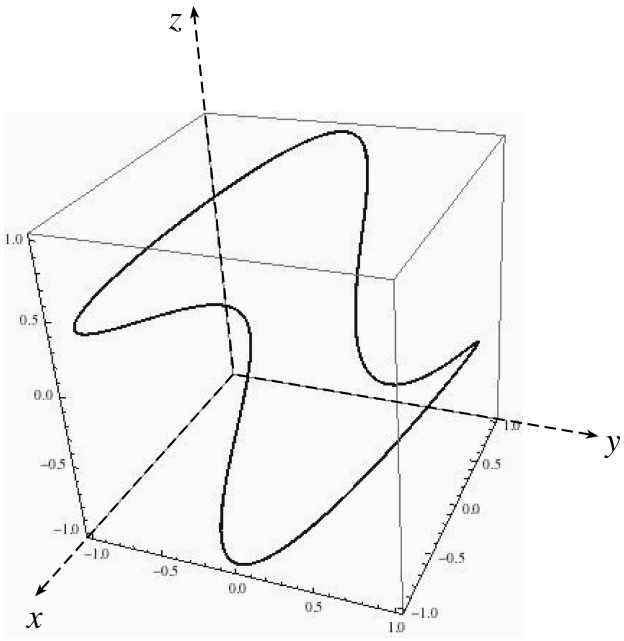

Figure 4.1: The trajectory of the solution $X=\sin(t)$, $Y=\cos(3t)$, $Z=\cos(t)$ on a three-dimensional phase diagram.

© University of Pretoria

Usually it is not practical to plot the trajectory and present it in the complete three-dimensional phase-space. It is more convenient to plot its projections on the three planes linked to the three-dimensional coordinates, i.e. the $X-Y$ plane (where $Z=0$), the $X-Z$ plane (where $Y=0$), and the $Y-Z$ plane (where $X=0$). These graphs will represent the projection of the trajectory on these planes. Therefore it becomes imperative to present the selected example and demonstrate some possible issues related to the interpretation of such diagrams in order to avoid misleading conclusions. The projections of the trajectory presented in Figure 4.1 on the $X-Y$, $X-Z$, and $Y-Z$ planes are presented in Figure 4.2. Figure 4.2(a) presents the solution in the time domain for $X(t)$, while Figures 4.2(b),(c), and (d) represent the projections of the trajectory on the three planes as indicated above.

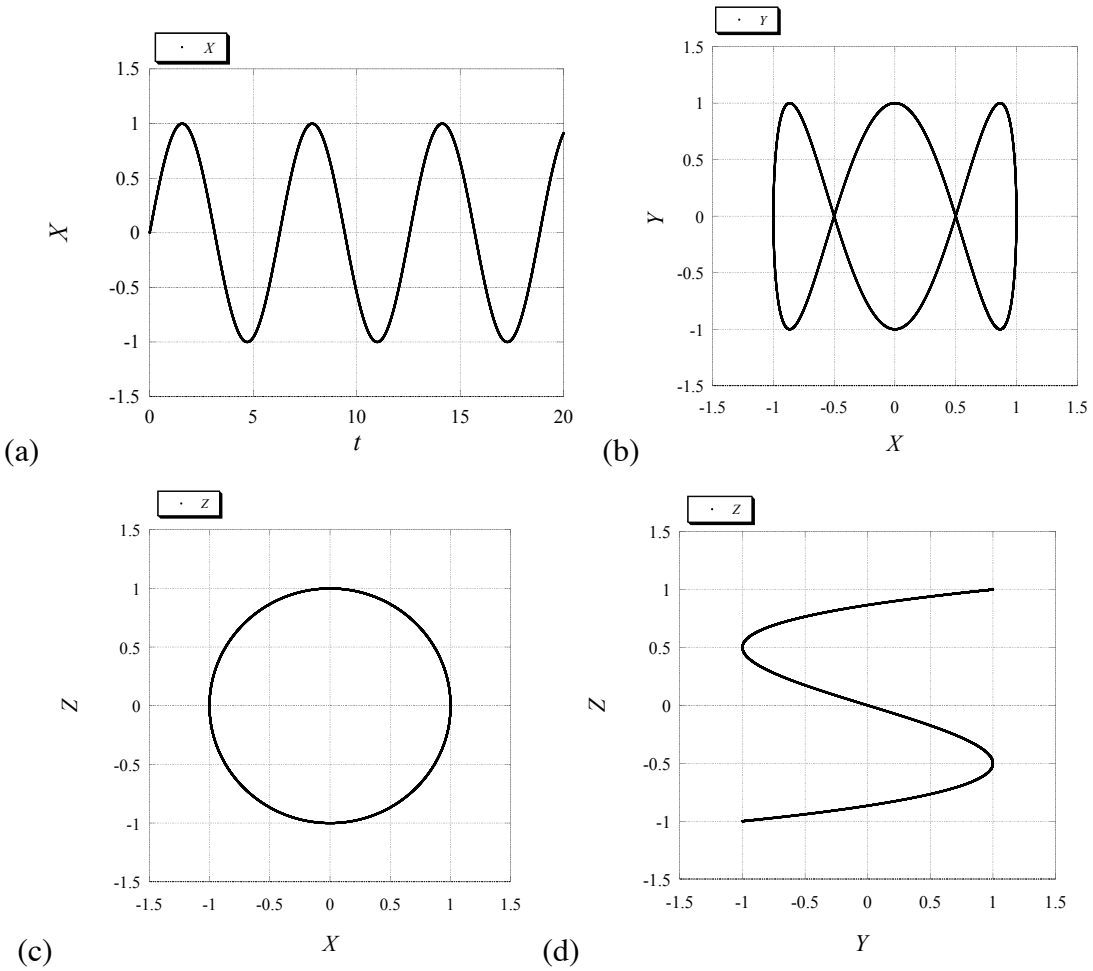

Figure 4.2: Projections of the trajectory of the solution $X=\sin(t)$, $Y=\cos(3t)$, $Z=\cos(t)$ on the $X-Y$, $X-Z$, and $Y-Z$ planes.

© University of Pretoria

The main features of these projections is that in Figure 4.2(b) representing the projection on the $Y-Z$ plane the trajectory seems to be apparently intersecting itself while it was indicated that this is impossible in any dynamical system. From the three-dimensional picture of the trajectory presented in Figure 4.1 it is evident that the trajectory does not intersect itself. The "apparent" intersection is a consequence of the projection and therefore conclusions about intersection of trajectories cannot be drawn from the projections of the trajectory on the $X-Y$, $X-Z$, and $Y-Z$ planes, nor any other projections. Actually, it is quite common that these projections will disclose such apparent intersections that are not real. The projection on the $X-Z$ plane identifies a closed trajectory forming a circle. This is to be expected because by squaring the equations for $X(t), Y(t)$ and $Z(t)$, and adding them and using equation (62) yields

$$X^2+Y^2+Z^2=\sin^2(t)+\cos^2(3t)+\cos^2(t)=1+Y^2 \tag{63}$$

and for $Y=0$ representing the $X-Z$ plane on which the projection is sought yields

$$X^2+Z^2=1 \tag{64}$$

which is the equation of a circle.

Another example is the trajectory corresponding to

$$X=\sin(t),\ Y=\cos(t),\ Z=\cos(2t) \tag{65}$$

Its representation on the three-dimensional phase diagram is presented in Figure 4.3.

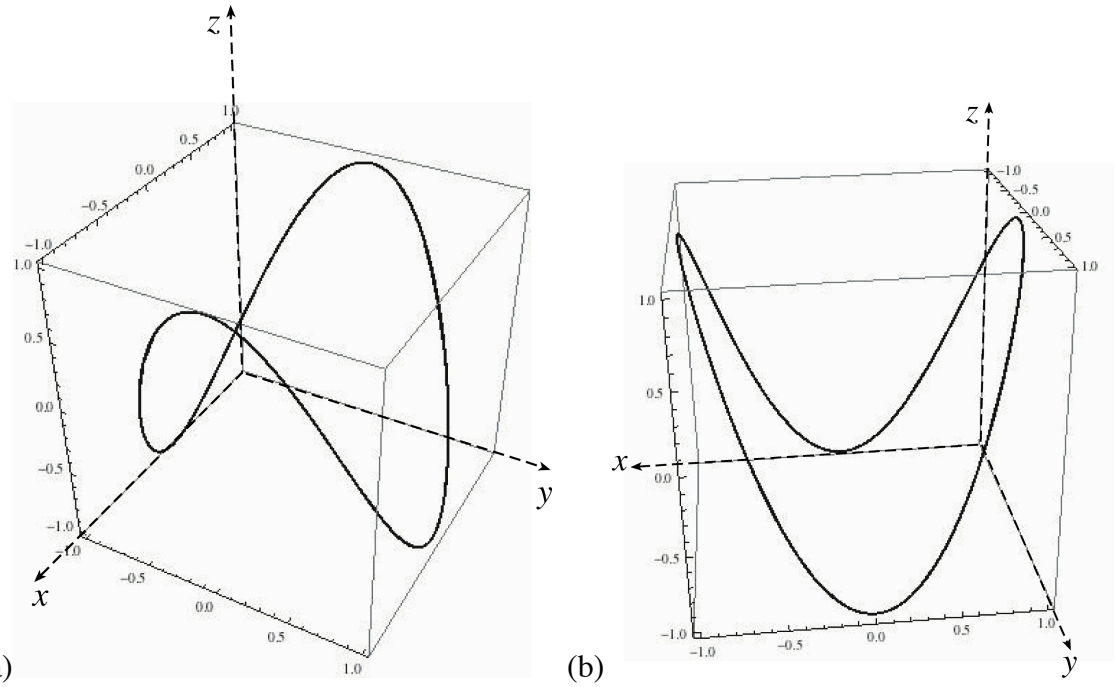

(a) (b)

Figure 4.3: The trajectory of the solution $X=\sin(t)$, $Y=\cos(t)$, $Z=\cos(2t)$ on a three-dimensional phase diagram.

© University of Pretoria

In Figure 4.3(a) it is evident that even on a three-dimensional representation of the trajectory the curve appears to be intersecting from this angle, however a rotation around the vertical axis presented in 4.3(b) clearly demonstrates that this is not the case. The projections of the trajectory on the $X-Y$, $X-Z$, and $Y-Z$ planes are presented in Figure 4.4. Figure 4.4(a) shows the graphical representation of the amplitude X versus time, while Figures 4.4(b),(c), and (d) represent the projections of the trajectory on the $X-Y$, $X-Z$, and $Y-Z$ planes. The circle obtained on the $X-Y$ projection corresponding to $Z=0$ can be obtained from (65) by squaring each of the equations and adding them while setting $Z=0$ resulting in the equation $X^2+Y^2=1$ representing the circle obtained in Figure 4.4(b). On the other hand by using the equation for $Z(t)$, leads to $Z=\cos(2t)=1-2\sin^2(t)=1-2X^2$ and for any constant value of Y including $Y=0$ this equation represents an inverted parabola, as indeed it shows in Figure 4.4(c). The latter shows a trajectory that is apparently not closed, while in reality this is a closed trajectory that the projection of its two branches overlaps.

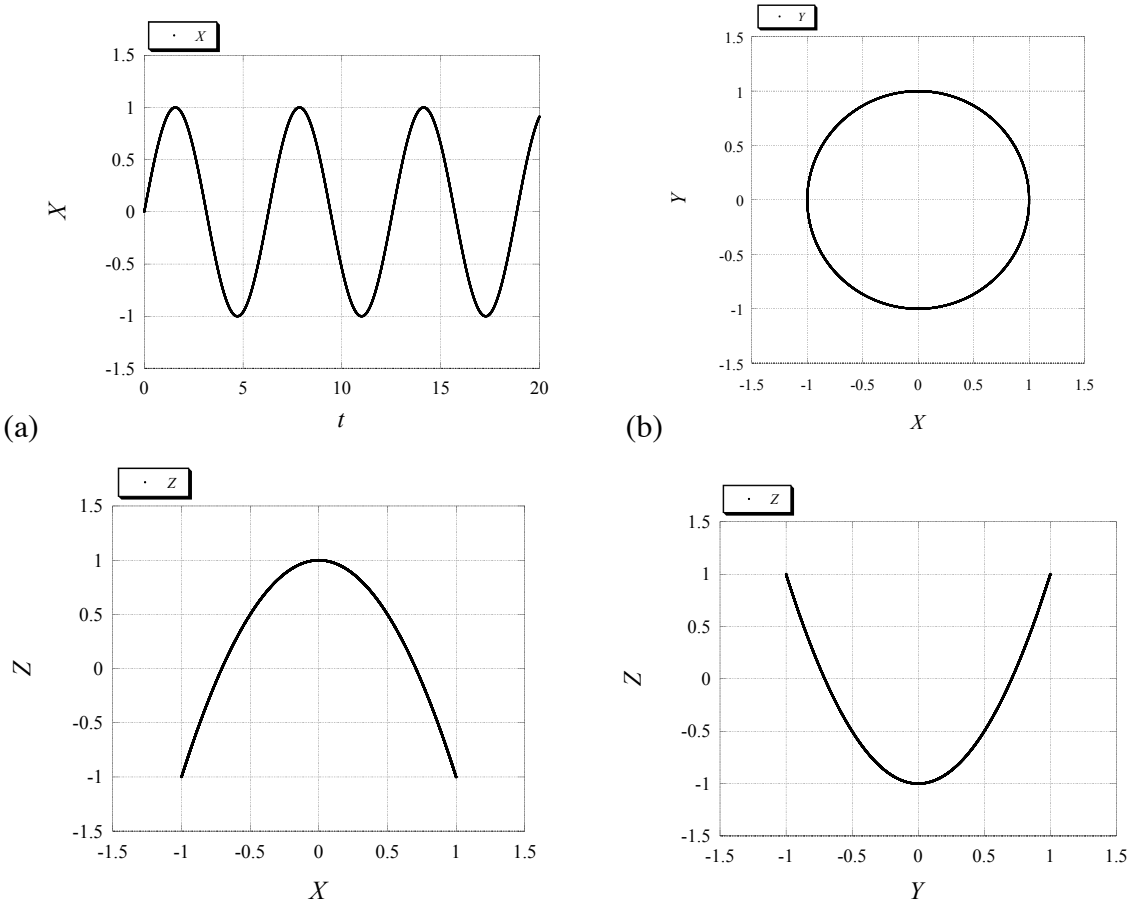

(a) (b)

(c) (d)

Figure 4.4: $X=\sin(t)$, $Y=\cos(t)$, $Z=\cos(2t)$ on the $X-Y$, $X-Z$, and $Y-Z$ planes.

© University of Pretoria

A similar parabolic picture is obtained in Figure 4.4d.

An important feature that will appear in the results is the appearance of quasi-periodic solutions. While not essential to the eventual application of these results it is important to distinguish such quasi-periodic solution in order to avoid confusing it with a chaotic solution that is essentially distinct but may look alike. The distinction between periodic and quasi-periodic solution is presented first by looking at a trajectory moving on a torus as presented in Figure 4.5. The torus is characterized by two radii, the large radius of the centreline of the large circle r_O and the small radius of the circle obtain by a vertical cross-section of the torus r_I. The motion of the trajectory around the centre of the torus has a frequency ω_O, while the motion around the smaller cross-sectional circle has a frequency ω_I.

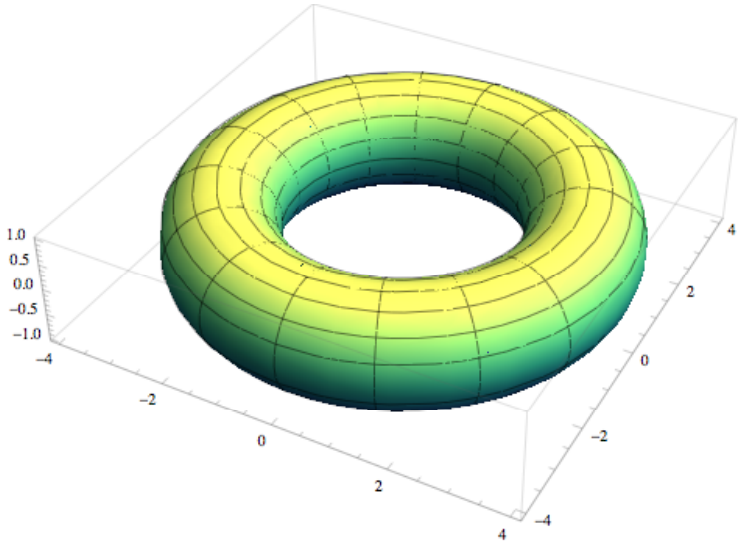

Figure 4.5: A torus on which the trajectory is allowed to move.

Let us consider the trajectory represented by the following parametric curves:

$$X = \left[30 + 5\sin(100\pi t)\right]\cos(2\pi t) \tag{66}$$

$$Y = \left[30 + 5\sin(100\pi t)\right]\sin(2\pi t) \tag{67}$$

$$Z = 5\cos(100\pi t) \tag{68}$$

These equations represent the spiral motion of the trajectory on a torus. As long as the ratio between the two frequencies is a rational number the trajectory will close itself and the motion will be periodic. In the example presented above the frequency ratio is $\omega_I/\omega_O = 100\pi/2\pi = 50$ a rational number indeed and therefore the result is a closed trajectory as presented in Figure 4.6.

© University of Pretoria

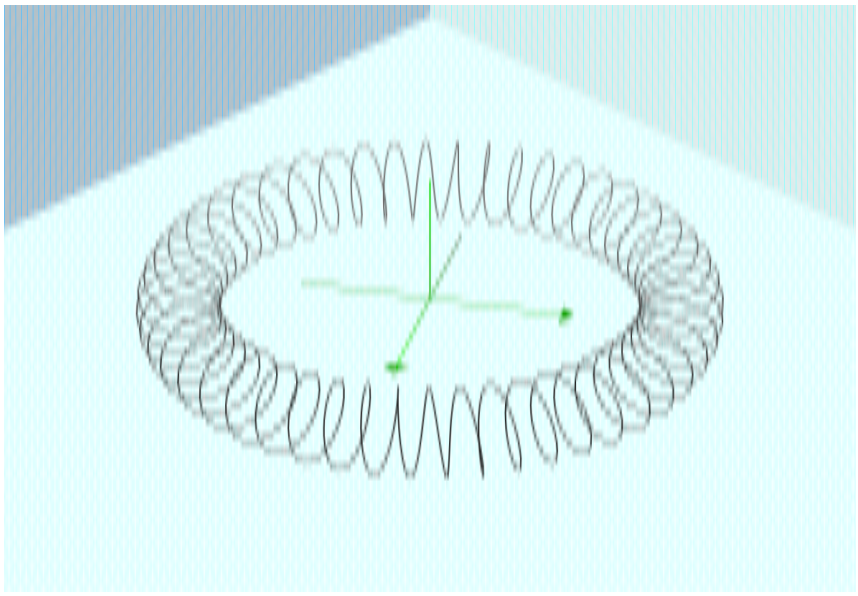

Figure 4.6: A closed trajectory of a motion on a torus representing periodic motion.

When the ratio between the frequencies is an irrational number such as in the system

$$X = \left[30 + 5\sin(50\pi t)\right]\cos(2t) \tag{69}$$

$$Y = \left[30 + 5\sin(50\pi t)\right]\sin(2t) \tag{70}$$

$$Z = 5\cos(50\pi t) \tag{71}$$

that produces $\omega_I/\omega_O = 50\pi/2 = 50\pi$ and therefore it is irrational the trajectory cannot close ever as presented in Figure 4.4. The end of the trajectory after the first cycle cannot meet its beginning, not even after any number of more cycles. This is an example of quasi-periodic motion.

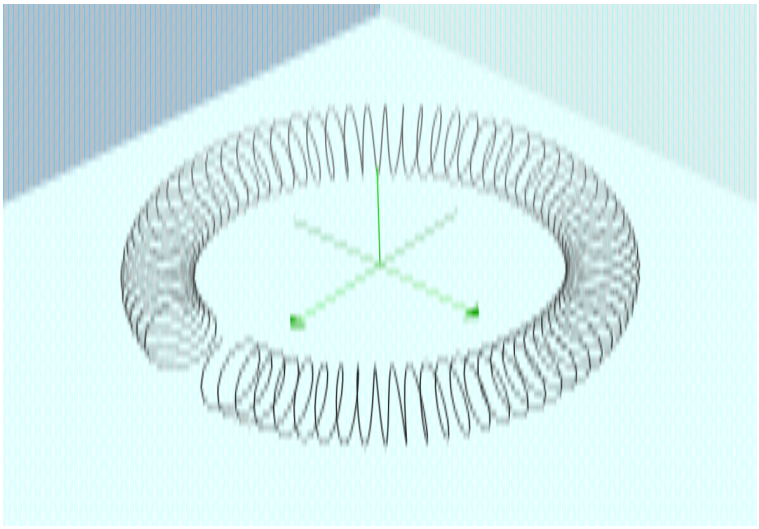

Figure 4.7: A trajectory that cannot close on a torus representing quasi-periodic motion.

© University of Pretoria

4.3 Lyapunov exponents

It is essential to understand the distinction between the possible stable solutions of any dynamical system. A stable solution means that any small perturbation around it can cause only a small variation of the solution, and the stable trajectory essentially remains in the same neighbourhood. A stable trajectory is called an attractor. An unstable trajectory is called a repelor. Generally in a dynamical third-order system such as (29)-(31) one has four possible types of attractors. A stable fixed point of the system is an example of an attractor.

The original system of equation (29)-(31) was non-autonomous, i.e. it included time explicitly. Converting it to the corresponding autonomous form presented in equations (36)-(39) added an additional dependent variable $W(t)$ and removed the fixed points from the system. These fixed points exist only in the absence of vibrations and are obtained from the vibrating system (36)-(39) only when the vibration forcing amplitude $\delta = 0$, or when the vibrations frequency is $\omega = 0$, i.e. practically in the degenerated special states of no-vibrations. For these special cases (either $\delta = 0$ or $\omega = 0$) the system becomes

$$\dot{X} = -\alpha\left(X - Y\right) \tag{72}$$

$$\dot{Y} = -Y + R\,X - \left(R - 1\right)X\,Z \tag{73}$$

$$\dot{Z} = 4\gamma\left(X\,Y - Z\right) \tag{74}$$

The system (72)-(74) has three fixed points; the first fixed point: $X_1 = Y_1 = Z_1 = 1$, the second fixed point: $X_2 = Y_2 = -1;\ Z_2 = 1$, and the third fixed point: $X_1 = Y_1 = Z_1 = 0$. A linear stability analysis of the system (72)-(74) shows that any small perturbation around these fixed points changes in time as $e^{(\lambda_r + i\lambda_i)t}$ or $e^{(\lambda_r - i\lambda_i)t}$, where λ_r and λ_i are the real and imaginary parts of the eigenvalues of the system. The real part of the eigenvalues λ_r controls the stability of the system. If $\lambda_r \le 0$ any small perturbation either decays exponentially in time or at most will remain small, causing the fixed point in question to be stable and therefore an attractor. If however $\lambda_r > 0$ the small perturbations grow exponentially causing the fixed point to loose stability and the solution to move away from the fixed point, the latter becoming a repelor. Linear stability analysis is a powerful tool of evaluating the stability of fixed points. However, in order to evaluate the stability of other types of solutions, such as periodic, quasi-periodic or chaotic one needs to resort to the use of Lyapunov exponents. They are the analogue to the eigenvalues obtained

© University of Pretoria

when analyzing the stability of fixed points and they represent the rate of divergence or convergence of nearby trajectories. Based on the Lyapunov exponents one may determine whether the stable solution (attractor) is a fixed point, periodic orbit, quasi-periodic, or chaotic (strange attractor). Generally, for a system of order n there are n Lyapunov exponents. There is no analytical form of representing the Lyapunov exponents and evaluating them. Numerical evaluation is therefore the only available method. The following table represents these four possibilities for a system of order three.

Table 4.1: The four types of attractors in a system of order three and their Lyapunov exponents.

Attractor: → Lyapunov Exponents ↓	Fixed Point	Periodic Orbit	Quasi-periodic Orbit	Chaotic Orbit
λ_i	$\lambda_i < 0$ for all i (- , - , -). All < 0	Two $\lambda_i < 0$ and one $\lambda_j = 0$. (0 , - , -) All ≤ 0	One $\lambda_i < 0$ and two $\lambda_j = \lambda_k = 0$. (0 , 0 , -) All ≤ 0	One or more $\lambda_i > 0$ (+ , 0 , -), or (+ , - , -), or (+ , 0 , 0). At least one > 0

The Lyapunov exponents corresponding to the solutions obtained from the system with vibrations (36)-(39) are being evaluated and presented in the next chapter.

4.4 Heat flux and Nusselt number

This section is dedicated to the derivation of relationships for the average Nusselt number that are sufficiently general to include post-transient, but time dependent variations of the heat flux following a method developed by Vadasz (2001). This is accomplished first by using the conservative form of the energy equation **(25)**b, integrating it over the horizontal plane in order to obtain a spatially averaged Nusselt number, and then substituting the expression from equations **(24)**b and **(26)**b for the temperature. The definition of the horizontally averaged Nusselt number is given by

$$\overline{Nu}^h = \frac{1}{LW}\int_0^L dx \int_0^W dy \left[wT - \frac{\partial T}{\partial z} \right] \tag{75}$$

© University of Pretoria

Averaging horizontally the conservative form of the energy equation and using the boundary conditions on the sidewalls yields

$$\int_0^W dy \int_0^L dx \left[\frac{\partial T}{\partial t} + \nabla \cdot \left(\boldsymbol{V} T - \nabla T \right) \right] = \int_0^W dy \int_0^L dx \left[\frac{\partial T}{\partial t} \right] + \frac{\partial}{\partial z} \int_0^W dy \int_0^L dx \left[wT - \frac{\partial T}{\partial z} \right] = 0 \qquad (76)$$

and upon introducing equation (75) into (76) yields

$$\frac{\partial \overline{T}^h}{\partial t} + \frac{\partial \overline{Nu}^h}{\partial z} = 0 \qquad (77)$$

where $\overline{(\bullet)}^h = \left(\int_0^W dy \int_0^L dx (\bullet) \right) / (WL)$ stands for the horizontal averaging operator. Integrating equation (77) in the z direction and using the boundary condition $w = 0$ at $z = 0$ yields a relationship for the horizontally averaged Nusselt number in the form

$$\overline{Nu}^h (t,z) = -\int_0^z \frac{\partial \overline{T}^h (t,z)}{\partial t} dz - \left(\frac{\partial \overline{T}^h}{\partial z} \right)_{z=0} \qquad (78)$$

Substituting now the expression for the temperature from equations **(24)**b and **(26)**b and using the rescaled variables from equation **(56)** yields

$$\overline{Nu}^h (t,z) = 1 + \frac{2(R-1)}{R} Z + \frac{(R-1)}{R} \dot{Z} \left[1 - \cos(2\pi z) \right] \qquad (79)$$

An alternative form of equation (79) can be obtained by substituting equation **(60)** into (79) to yield

$$\overline{Nu}^h (t,z) = 1 + \frac{2(R-1)}{R} Z + \frac{2(R-1)}{R} (XY - Z) \left[1 - \cos(2\pi z) \right] \qquad (80)$$

Clearly when the post-transient solution is not time dependent and a steady state is reached, $\dot{Z} = 0$ and $Z = Z_S = 1$, therefore equation (79) yields

$$\overline{Nu}^h_{\substack{steady \\ state}} = 3 - \frac{2}{R} \qquad (81)$$

For the evaluation of the heat flux one is interested in an expression for the Nusselt number, which is independent of z. This can be accomplished by considering the heat flux into the domain crossing the bottom boundary at $z = 0$ or the heat flux from the domain crossing the boundary at $z = 1$. They both yield

$$\overline{Nu}^h (t) = \overline{Nu}^h (t,0) = \overline{Nu}^h (t,1) = 1 + \frac{2(R-1)}{R} Z \qquad (82)$$

© University of Pretoria

Equation (82) provides an expression for the spatially averaged Nusselt number, however the result is still time dependent if the post-transient solution for Z is not a stationary point, i.e. if it is periodic, quasi-periodic or chaotic. Averaging over the period in the case periodic solution will provide a time-average of the Nusselt number. The major limitation of this representation is the need to evaluate *apriori* the period of oscillations. For chaotic solutions, for example, this becomes theoretically impossible because then the period is either very large (i.e. beyond the time over which the solution is computed) or does not exist. Nevertheless, for such cases one can adopt an alternative, practical, approach by realizing that chaotic solutions are obtained because of the finite (and therefore limited) accuracy of the solution, hence two nearby solutions will diverge. However, this divergence is limited by the dissipative nature of the convection system. Therefore, by taking advantage of this limited divergence one can attempt to integrate the spatially averaged Nusselt number over a very large time range $\tau_1 = t_1 - t_o$ (starting from arbitrary post-transient values of the solution, at t_o). By separating the constant and time dependent parts of Z in the form $Z = 1 + Z'(t)$, averaging over the time range τ_1, and looking for the limit as $\tau_1 \to \infty$, yields from equation (82)

$$\overline{Nu}_o^{h\infty} = 1 + \frac{2(R-1)}{R} + \frac{2(R-1)}{R} \lim_{\tau_1 \to \infty} \left[\frac{1}{\tau_1} \int_{t_o}^{t_1} Z' dt \right] \tag{83}$$

The dissipative property of the convection system represented by the equations **(58)**-, **(60)** imposes the following restrictions on the solution $\lim_{\tau_1 \to \infty} \left[\int_{t_o}^{t_1} Z' dt \right] \to$ finite as well as $\lim_{\tau_1 \to \infty} [Z_o] \to$ finite and $\lim_{\tau_1 \to \infty} [Z_1] \to$ finite. This requirement to obtain finite values for the integral and for Z_o and Z_1 as $\tau_1 \to \infty$ causes the limits in equations (83), which consist of a ratio of a finite value over τ_1, to vanish as $\tau_1 \to \infty$. Then, both equations (83) yields

$$\overline{Nu}_o^{h\infty} = 1 + \frac{2(R-1)}{R} \tag{84}$$

which is identical to equation (81) for the steady state Nusselt number. While the limit as $\tau_1 \to \infty$ has significant theoretical value in providing an upper limit for the heat flux, in real and practical cases its applicability is problematic, especially when chaotic solutions are considered. In such cases evaluating the time average over a large, but finite, post-transient time range can provide an approximation for the heat flux. Because of the finite time range to be used in such a time averaging process the result is expected still to include oscillations, however, it is also expected that these oscillations become

© University of Pretoria

smaller as the time range used for averaging, τ_1, becomes larger. This behaviour will be observed when presenting the computational results. An additional particular point of interest can be observed from equation (84) when an upper bound for the heat flux is to be estimated. This can be evaluated using the limit of equation (84) for large values of R, i.e. as $R \to \infty$. For this limit equation, (84) produces $\overline{Nu}_{o,\infty}^{h\infty} = \lim_{R\to\infty}\left(\overline{Nu}_o^{h\infty}\right) = 3$. Therefore, the heat flux over the convective porous layer is limited in the present model by this upper bound value of 3. Higher values can only be obtained by including more modes in the truncated Galerkin representation of the spatial variation of the solution or by allowing the variation of the wave number as the value of R varies. Finally, the numerical results used in the evaluation of the Nusselt number were substituted into the following equation:

$$Nu = 1 + \frac{2(R-1)}{R}\,\frac{1}{\tau_1}\int_{t_o}^{t_1} Z\,dt \tag{85}$$

where t_o was some post-transient value, t_1 was the last value of time in the computations, and $\tau_1 = t_1 - t_o$. The integral in (85) was evaluated numerically by using the trapezoidal numerical integration method.

4.5 Summary

In the current chapter two methods are presented. The first is the method of solution, and the second is the method of graphical presentation of the results. The solutions for the amplitudes of stream function and temperature as a function of time were evaluated numerically via Fortran programming. The results are presented in graphs showing the amplitudes as a function of time as well as on phase diagrams aiming at identifying the different parameter regimes and possibly identify the regimes that enhance the heat transfer. In order to establish the stability type of the results and the type of the attracting trajectory the results were used to evaluate their corresponding Lyapunov exponents. The resulting Nusselt number was evaluated then, and presented as it varies with varying the value of the scaled Rayleigh number, in order to establish what parameter regimes cause heat transfer enhancement and which cause a heat transfer reduction when compared to the non-vibrating convection problem.

© University of Pretoria

CHAPTER 5

THEORETICAL RESULTS AND DISCUSSION

5.1 Results for the amplitudes subject to varying Rayleigh numbers and frequency

The computed numerical results for the amplitudes of convection for a vibrating porous layer heated from below are presented in terms of the amplitude in the time domain as well as projections of the three-dimensional phase diagrams on the $X-Y$, $X-Z$ and $Y-Z$ planes. The effect of the variation of the scaled Rayleigh number in the range $25 \le R \le 75$ on the results is then observed. Note that the non-vibrating system shows that the fixed points corresponding to steady convection $X = Y = \pm 1$, $Z = 1$ lose stability in the linear sense at $R = 25$. Different initial conditions may promote or delay this transition point, however, for initial conditions sufficiently close to these convective fixed points, the transition from steady to chaotic (weak-turbulent) convection occurs at or very close to $R = 25$. Therefore, the initial conditions for all the numerical solutions were selected close to these convective fixed points as

$$X_o = 0.9\ ,\ Y_o = 0.9\ ,\ Z_o = 0.9\ ,\ W_o = 0 \tag{86}$$

The effect of the scaled Rayleigh number and frequency is the major objective of the investigation. It is anticipated that a strong forcing vibration amplitude δ will affect the convection, however, the more important point is to test whether specific frequencies may resonate the solution even when the forcing vibration amplitude δ is not strong. Therefore, δ was kept constant in all the numerical computations and was assigned a value of

$$\delta = 1 \tag{87}$$

in all computations. The visualisation of the solution for $W(t)$ does not add anything to the graphical description because by its own definition $W(t) = \omega t$. Therefore there is no point in including W in the presentation, and only the amplitudes $X(t)$, $Y(t)$ and $Z(t)$ are represented graphically. A large number of computational results were obtained. Only a select group of these results is presented here to demonstrate the types of different solutions obtained. For reference purposes, the first result presented in each group corresponds to the solution obtained for the case when there is no vibration. No vibration was obtained by setting the frequency $\omega = 0$.

© University of Pretoria

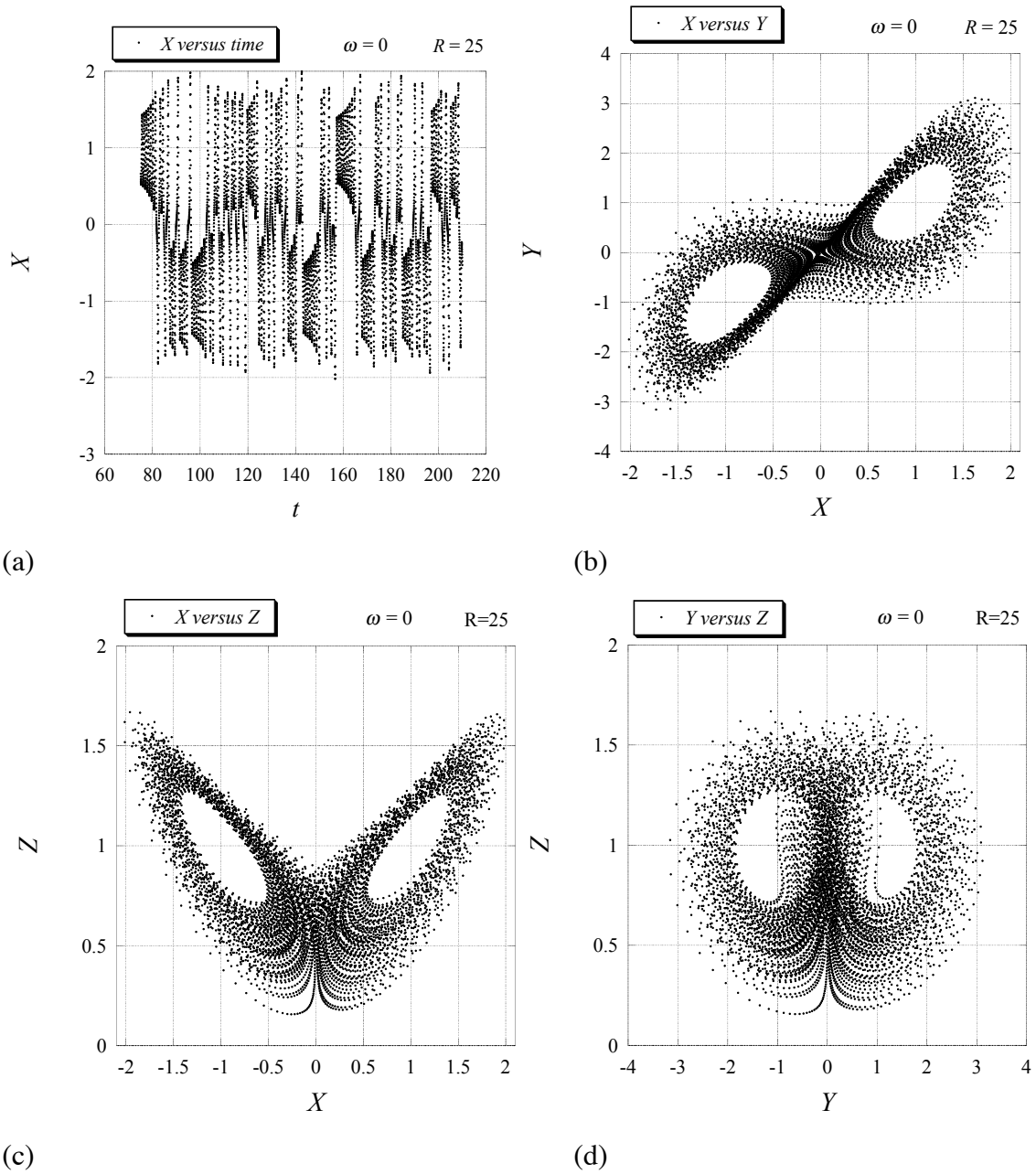

Figure 5.1: Graphical description of the solutions for $\omega = 0, R = 25$: (a) The amplitude X in the time domain, i.e. X versus t, (b), (c), and (d). The solution on a phase diagram: projections of the solution on the $X-Y$, $X-Z$ and $Y-Z$ planes, respectively. The data points are not connected.

The numerical post-transient results ($t > 80$) when there are no forced vibrations are presented in Figure 5.1 for a value of $R = 25$. This is the value where the transition to chaos occurs in the non-vibrating case. Figure 5.1 demonstrates the typical chaotic attractor on the phase diagram as well the typical form of the solution in the time domain.

© University of Pretoria

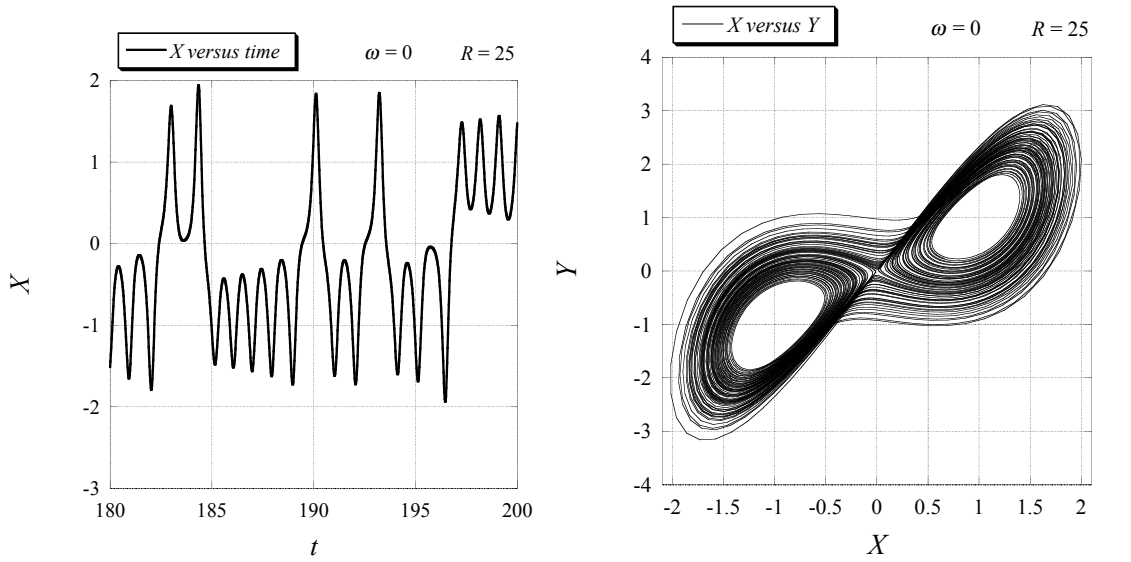

(a) (b)

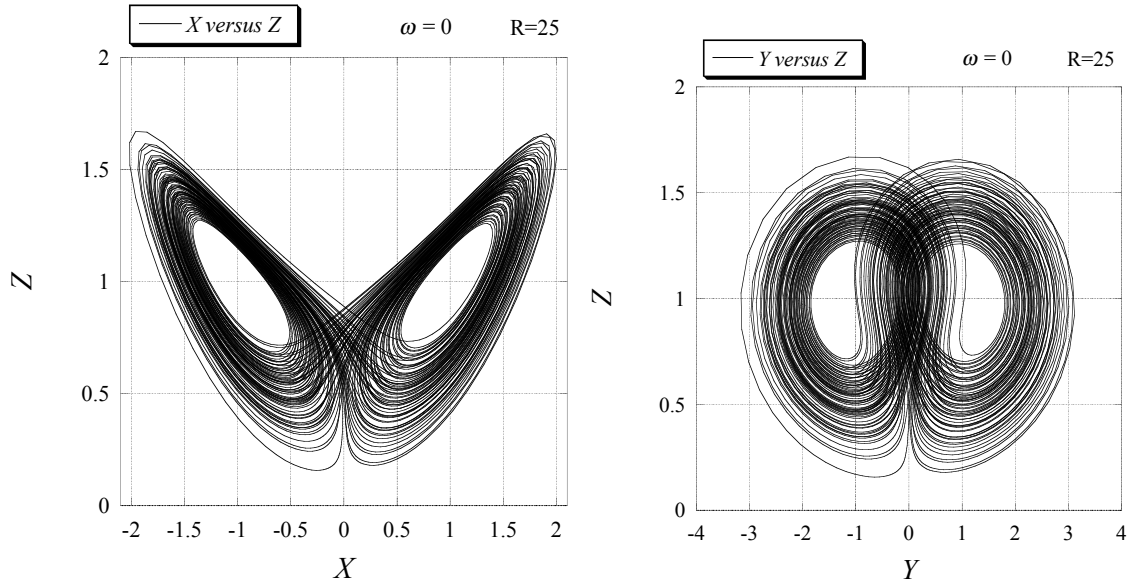

(c) (d)

Figure 5.2: Graphical description of the solutions for $\omega = 0, R = 25$: (a) The amplitude X in the time domain, i.e. X versus t, (b), (c), and (d). The solution on a phase diagram: projections of the solution on the $X-Y$, $X-Z$ and $Y-Z$ planes, respectively. The data points are connected.

In all presentations, the data points of the solution and its trajectory were not connected in order to provide a better view of the graphical results. In order to observe how the solution will look when the data points are connected, the same results as in Figure 5.1 are being presented in Figure 5.2, where the data points are connected. In this particular example, connecting the data points does not obscure the visualisation.

© University of Pretoria

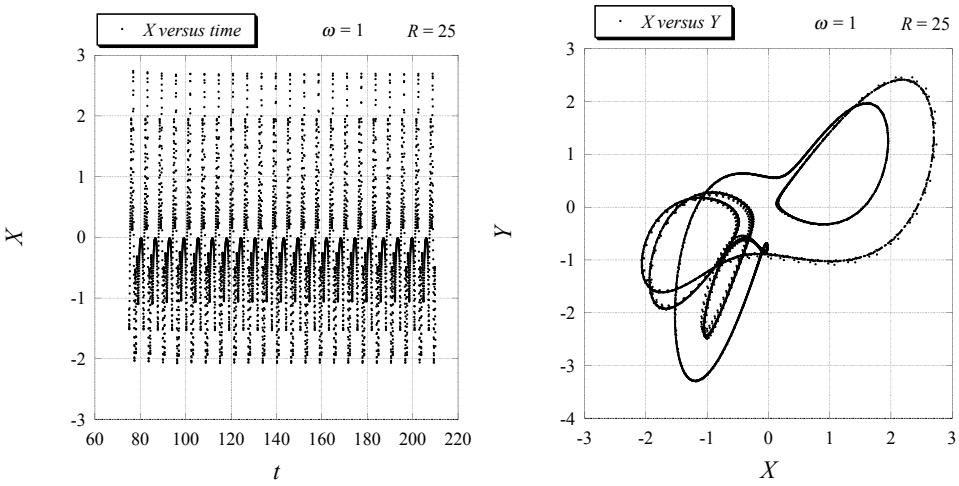

(a) (b)

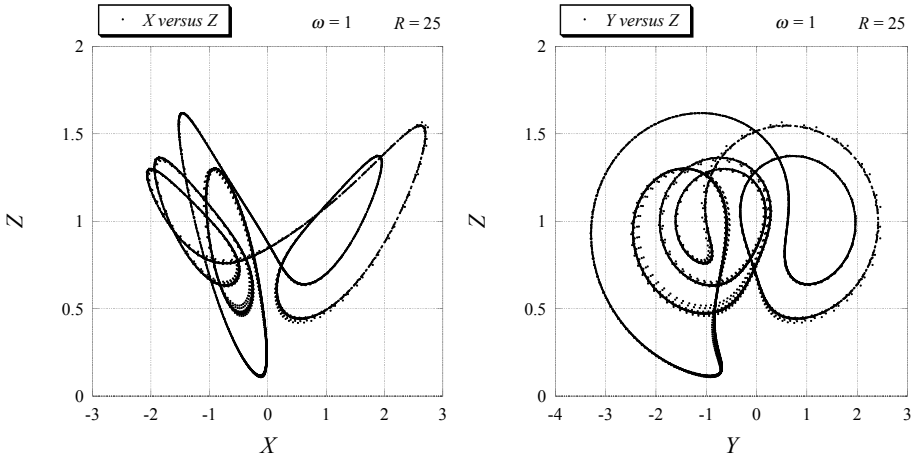

(c) (d)

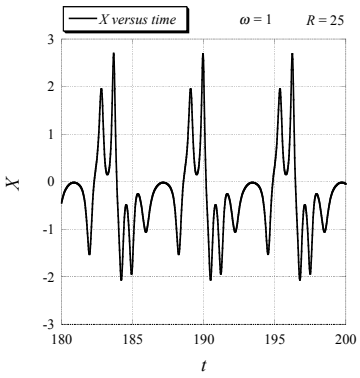

(e)

Figure 5.3: Graphical description of the solutions for $\omega = 1, R = 25$: (a) The amplitude X in the time domain, i.e. X versus t, (b), (c), and (d). The solution on a phase diagram: projections of the solution on the $X-Y$, $X-Z$ and $Y-Z$ planes, respectively. (e) Zoom into the time domain $180 \le t \le 200$, X versus t.

© University of Pretoria

The first effect of vibrations on the solution is presented in Figure 5.3 corresponding to $\omega = 1, R = 25$. The same format of presentation is maintained across this section, meaning that the first graph represents the solution $X(t)$ in the time domain, followed by the three projections from the phase-diagram on the planes $X - Y$, $X - Z$ and $Y - Z$, respectively. Occasionally, a zoom into a particular time domain is added to provide detailed insight when it is of interest. This is the case in Figure 5.3, where the inset into the time domain $180 \le t \le 200$ is presented in Figure 5.3e. From the graphical results presented in Figure 5.3 it is evident that forcing vibrations rendered the otherwise chaotic solution presented in Figure 5.1 corresponding to $\omega = 0$ into a periodic solution when $\omega = 1$, at the same value of the scaled Rayleigh number $R = 25$.

Increasing the forcing vibration frequency to $\omega = 5$ produces the results presented in Figure 5.4, where a chaotic or quasi-periodic solution is observed. It is sometimes very difficult to distinguish some times between a chaotic and a quasi-periodic solution. The only way to do this accurately is by evaluating the Lyapunov exponents. These exponents will be evaluated and presented in the next section.

Increasing further the forcing vibration frequency to $\omega = 6.5$ yields the results presented in Figure 5.5 identifying a periodic solution. The values of the Lyapunov exponents to be presented in the next section confirm that only one of them is zero and the rest are negative, implying a periodic orbit based on Table 4.1. An interesting result is obtained for $\omega = 7$ and the same value of the scaled Rayleigh number $R = 25$, and is presented in Figure 5.6. The solution oscillates around the 'ghost' fixed point $X = Y = Z = 1$ followed at a later time by larger amplitude oscillations around both convective 'ghost' fixed points $X = Y = \pm 1, Z = 1$. The term 'ghost' is used in the loose sense referring to the fact that the forced-vibration system has no fixed points. This exists only when $\omega = 0$. The solution looks periodic.

At a frequency of $\omega = 8$, periodic oscillations with a single frequency are observed as presented in Figure 5.7.

© University of Pretoria

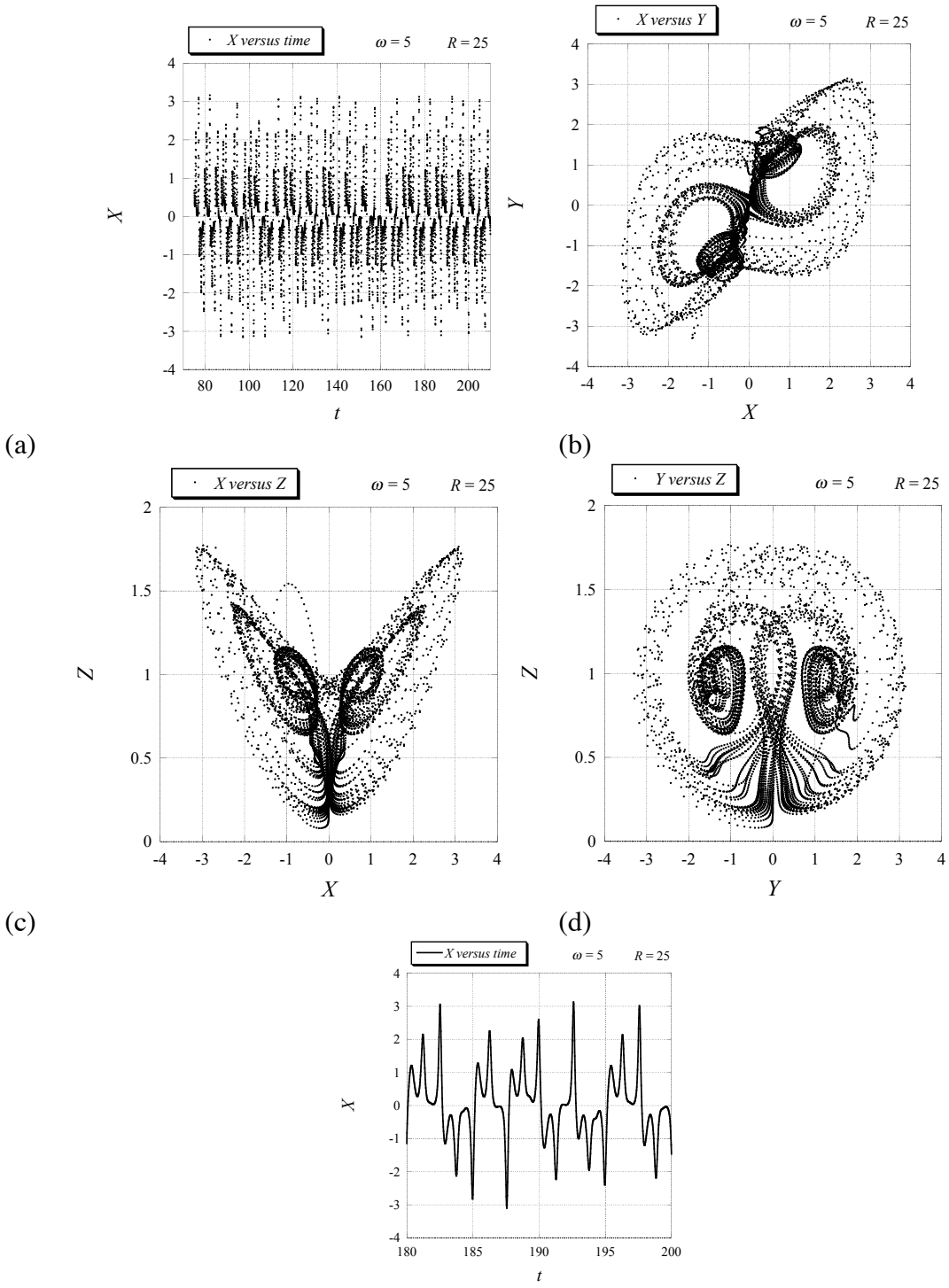

Figure 5.4: Graphical description of the solutions for $\omega = 5, R = 25$: (a) The amplitude X in the time domain, i.e. X versus t, (b), (c), and (d). The solution on a phase diagram: projections of the solution on the $X-Y$, $X-Z$ and $Y-Z$ planes, respectively. (e) Zoom into the time domain $180 \le t \le 200$, X versus t.

© University of Pretoria

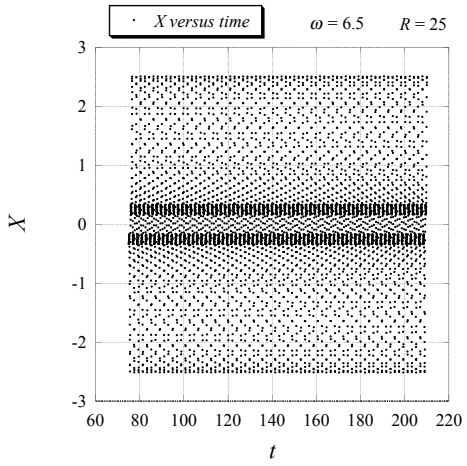

(a)

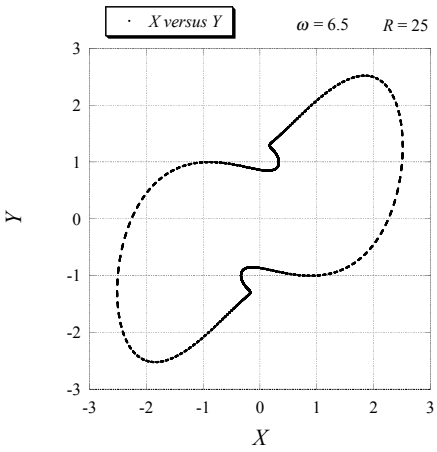

(b)

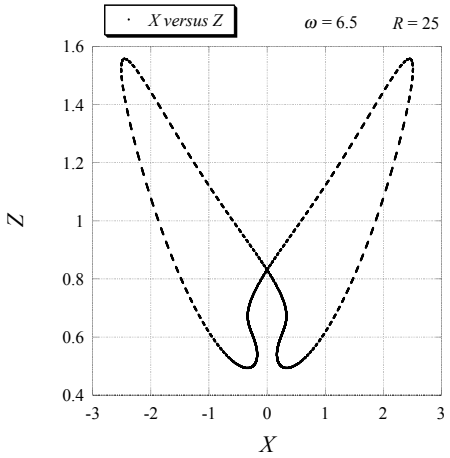

(c)

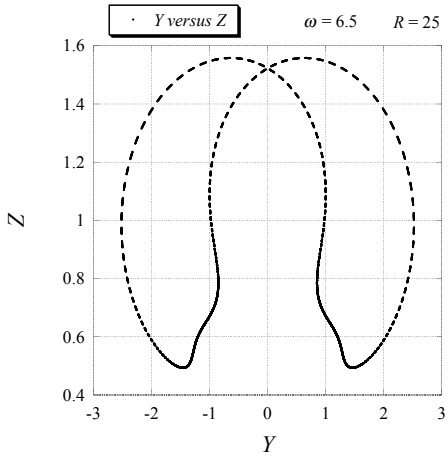

(d)

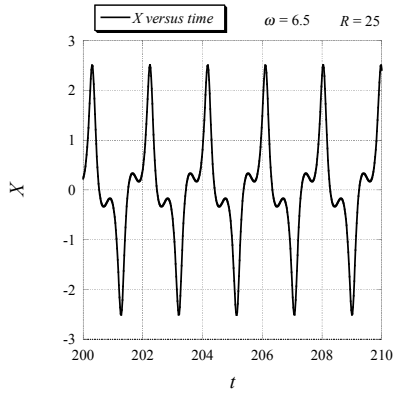

(e)

Figure 5.5: Graphical description of the solutions for $\omega = 6.5, R = 25$: (a) The amplitude X in the time domain, i.e. X versus t, (b), (c), and (d). The solution on a phase diagram: projections of the solution on the $X-Y$, $X-Z$ and $Y-Z$ planes, respectively. (e) Zoom into the time domain $200 \le t \le 210$, X versus t.

© University of Pretoria

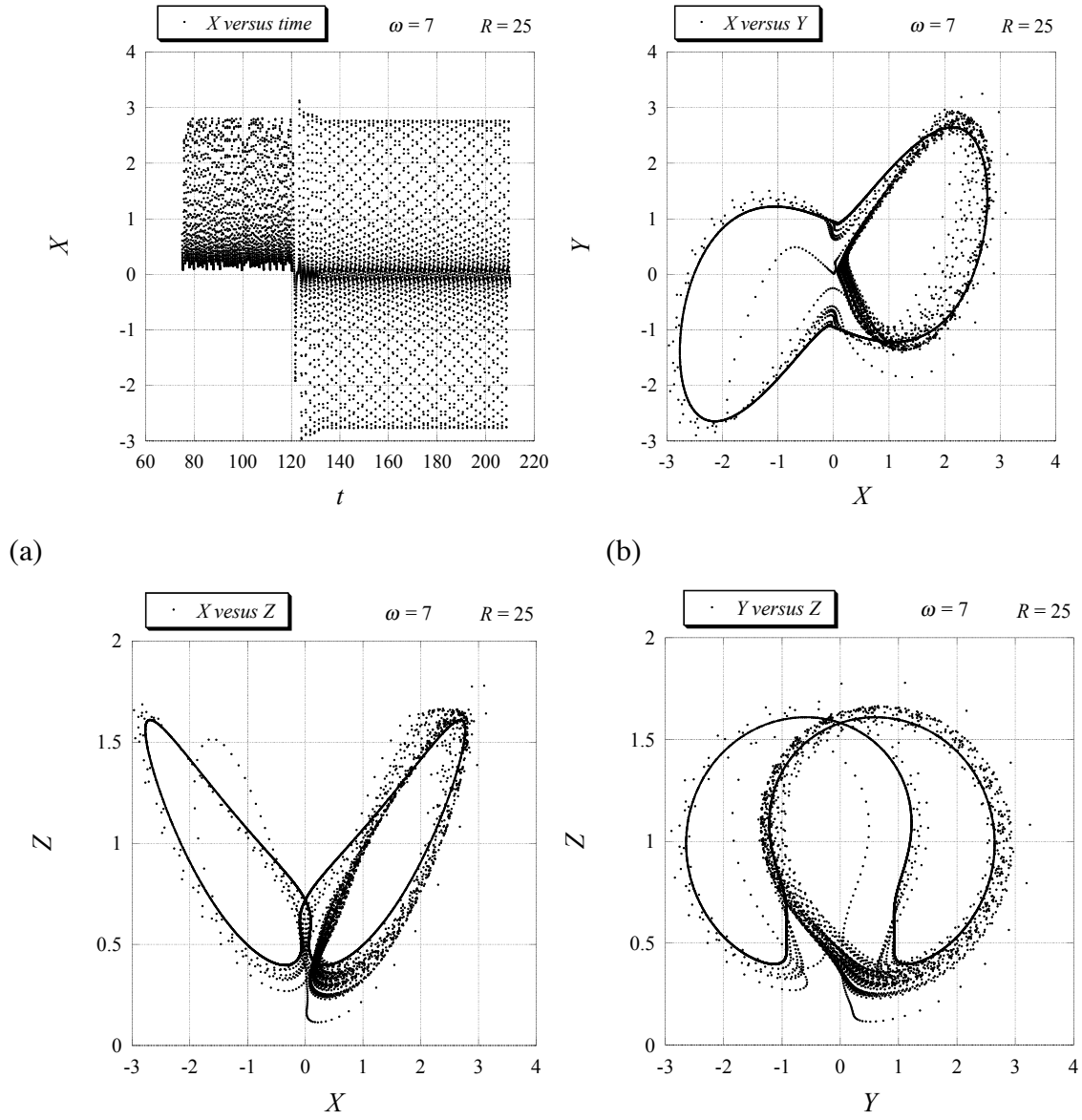

Figure 5.6: Graphical description of the solutions for $\omega = 7, R = 25$: (a) The amplitude X in the time domain, i.e. X versus t , (b), (c) and (d) The solution on a phase diagram: projections of the solution on the $X-Y$, $X-Z$ and $Y-Z$ planes, respectively.

© University of Pretoria

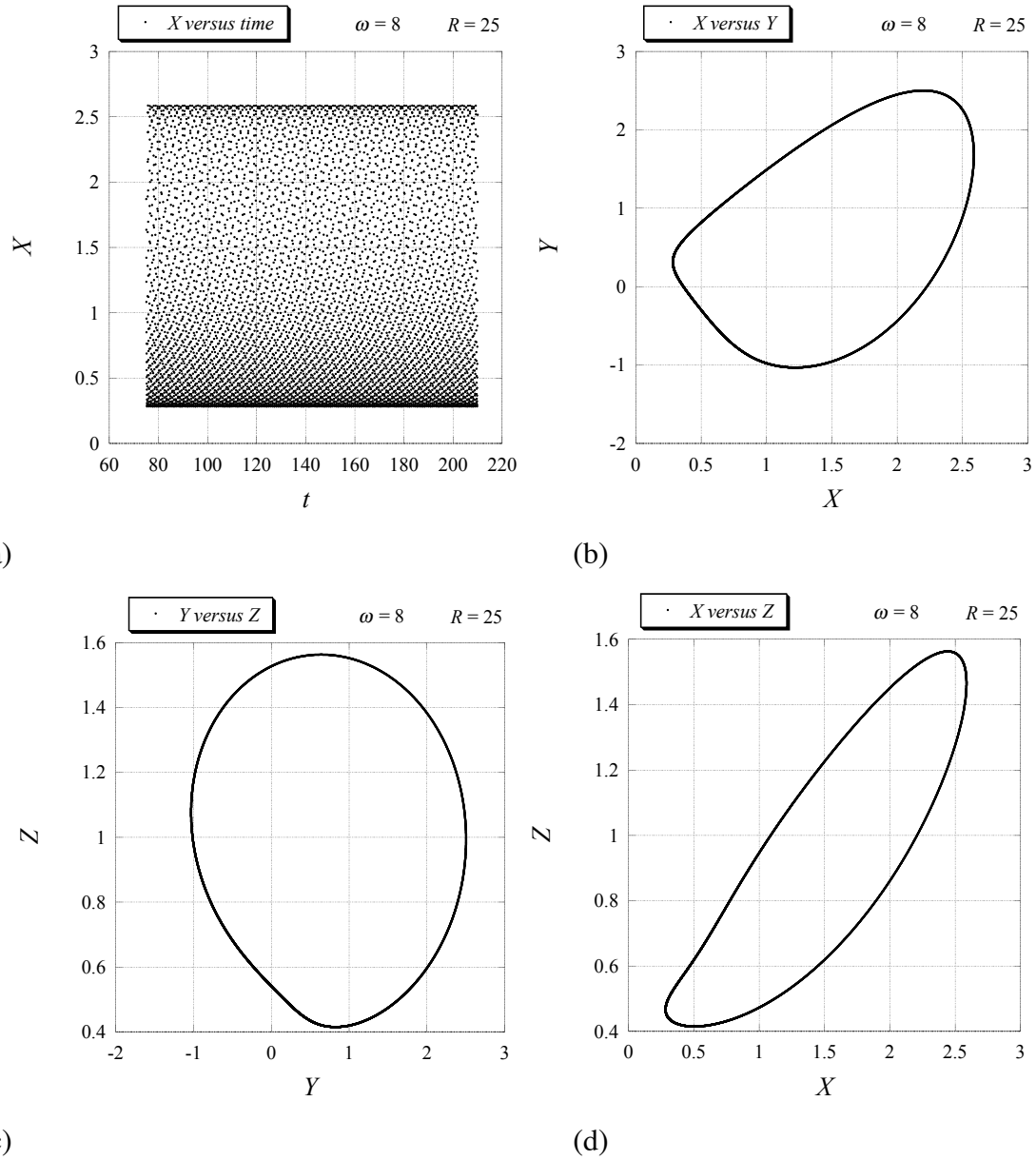

Figure 5.7: Graphical description of the solutions for $\omega = 8, R = 25$: (a) The amplitude X in the time domain, i.e. X versus t, (b), (c) and (d) The solution on a phase diagram: projections of the solution on the $X-Y$, $X-Z$ and $Y-Z$ planes, respectively.

© University of Pretoria

A burst that is typical to a homoclinic explosion shows-up in Figure 5.8 for $\omega = 8.1327$, however, the solution stabilises immediately to a periodic orbit. This burst is an indication of what is to occur next as the value ω increases further to $\omega = 10$. The solution returns to chaotic behaviour for $\omega = 10$, as shown in Figure 5.9. Although the solution is different from that without vibration, $\omega = 0$, it has returned to the chaotic solution expected at a scaled Rayleigh number $R = 25$.

Increasing the frequency further to $\omega = 13.5$ brings back periodic oscillations with a single frequency, as presented in Figure 5.10. With a frequency $\omega = 20$, the solution again returns to chaotic behaviour presented in Figure 5.11.

© University of Pretoria

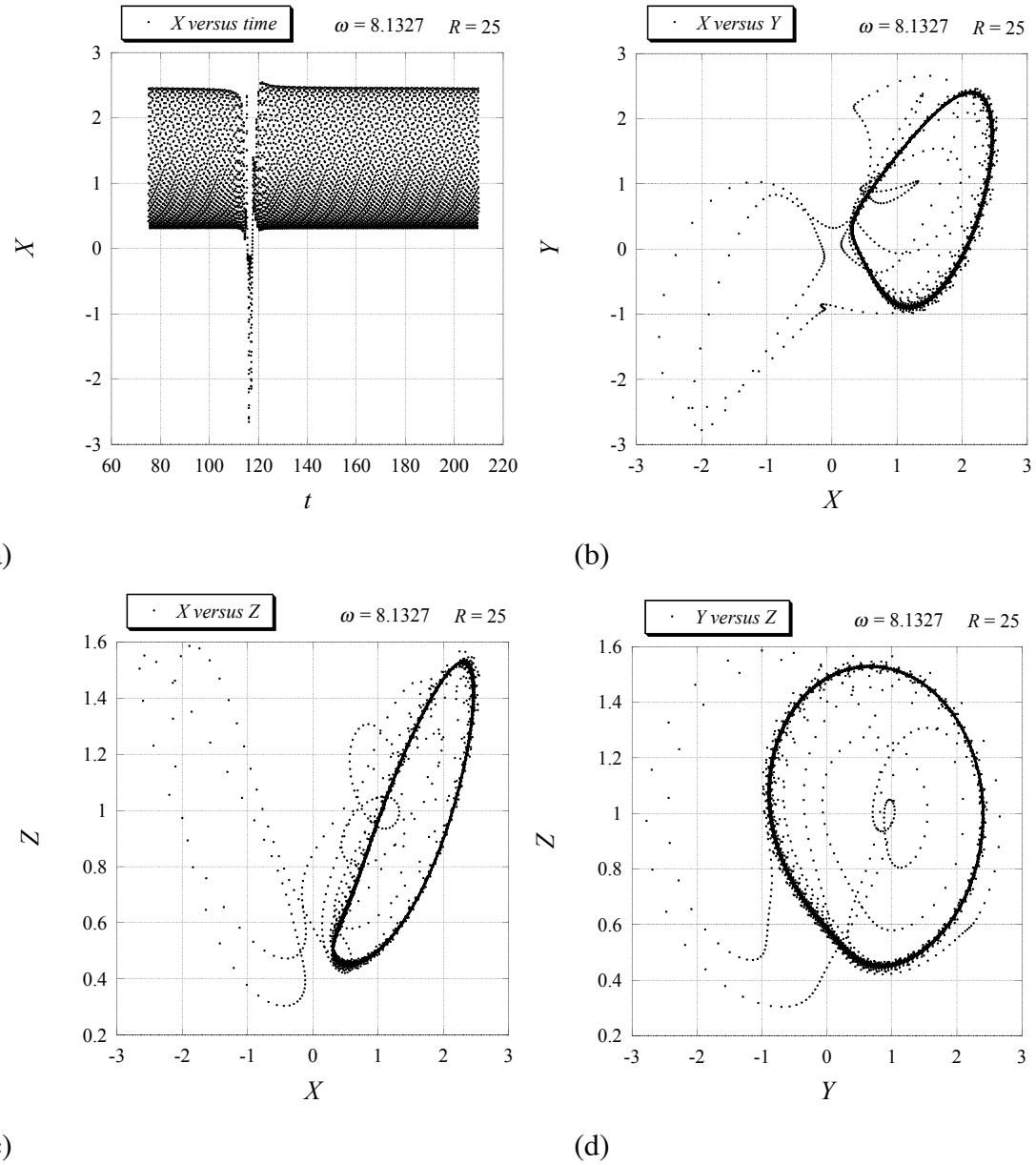

Figure 5.8: Graphical description of the solutions for $\omega = 8.1325, R = 25$: (a) The amplitude X in the time domain, i.e. X versus t, (b), (c) and (d) The solution on a phase diagram: projections of the solution on the $X-Y$, $X-Z$ and $Y-Z$ planes, respectively.

© University of Pretoria

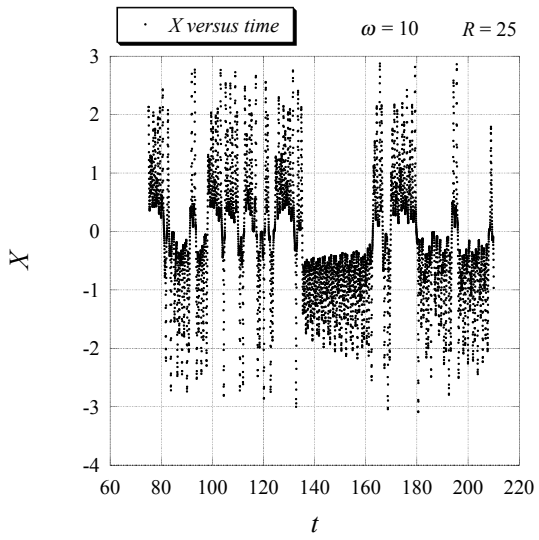

(a)

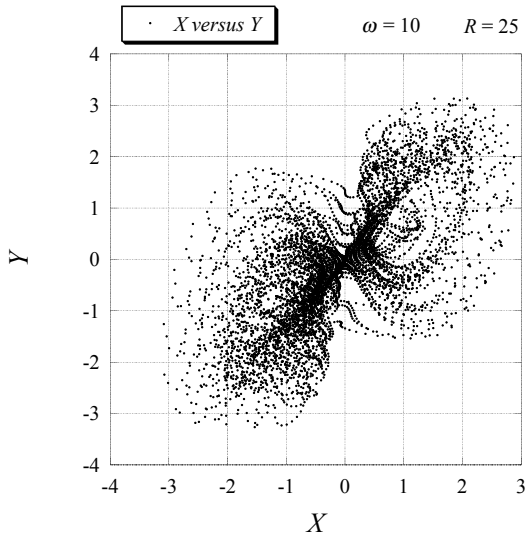

(b)

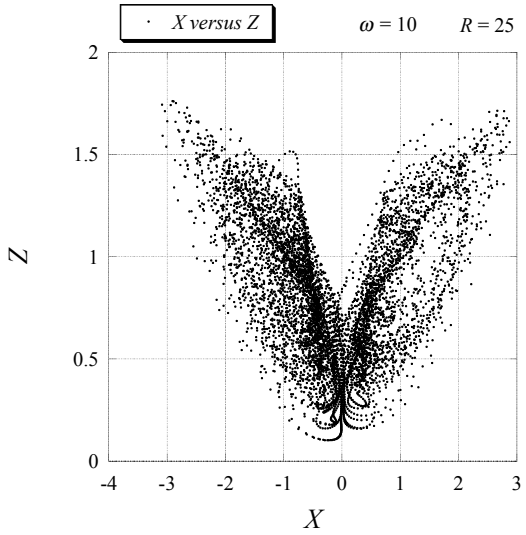

(c)

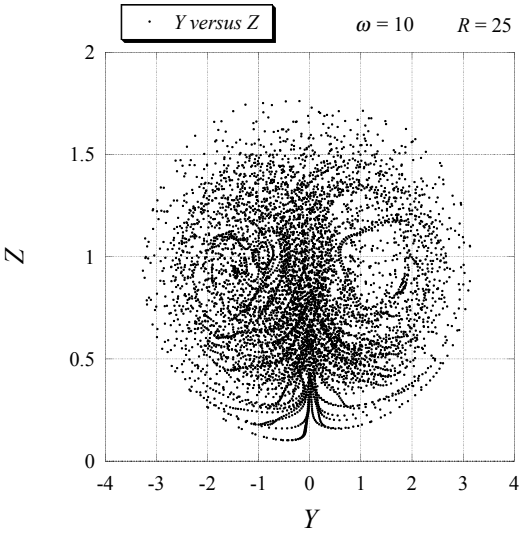

(d)

Figure 5.9: Graphical description of the solutions for $\omega = 10, R = 25$: (a) The amplitude X in the time domain, i.e. X versus t, (b), (c) and (d) The solution on a phase diagram: projections of the solution on the $X-Y$, $X-Z$ and $Y-Z$ planes, respectively.

© University of Pretoria

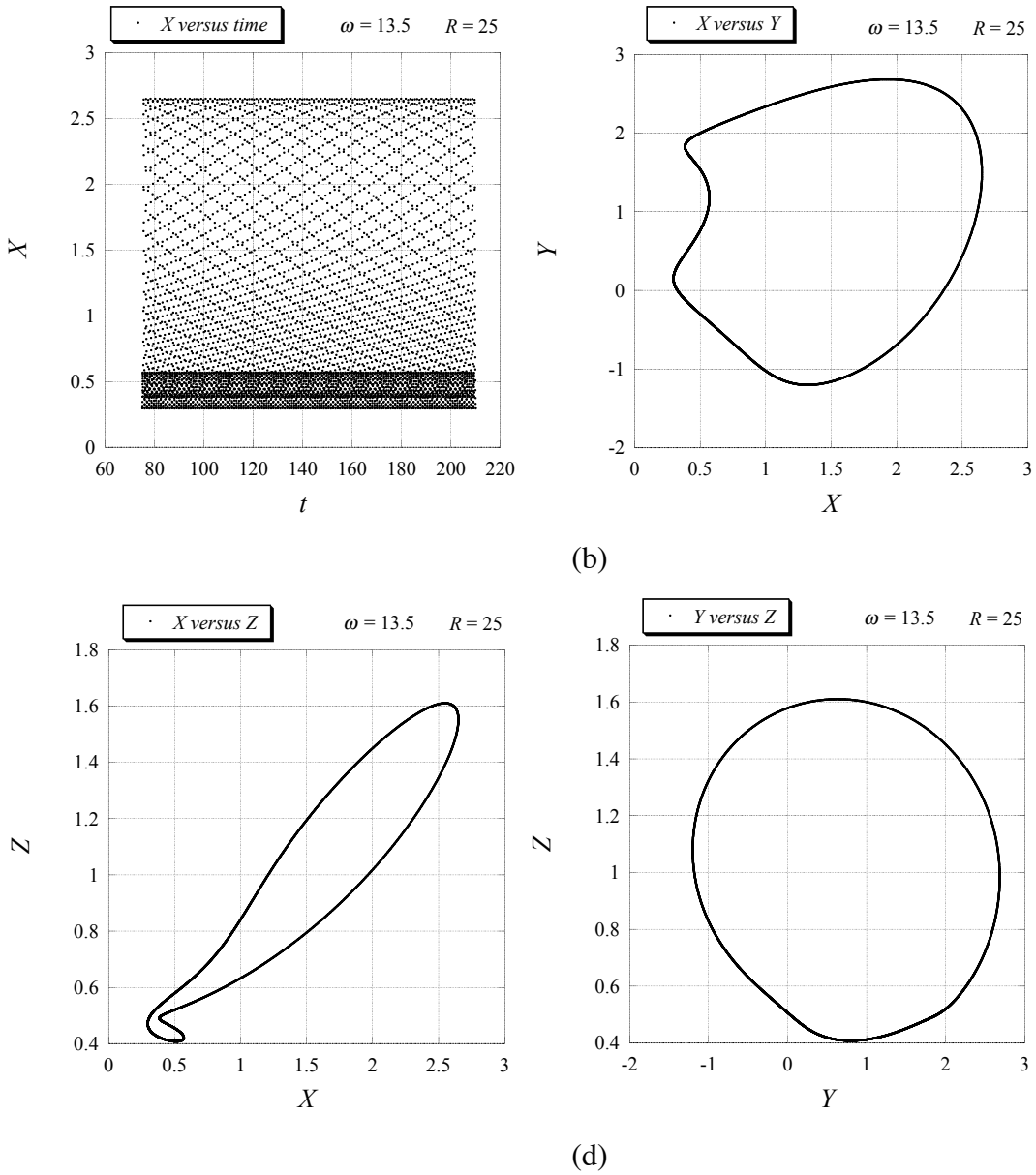

Figure 5.10: Graphical description of the solutions for $\omega = 13.5, R = 25$: (a) The amplitude X in the time domain, i.e. X versus t, (b), (c) and (d) The solution on a phase diagram: projections of the solution on the $X-Y$, $X-Z$ and $Y-Z$ planes, respectively.

© University of Pretoria

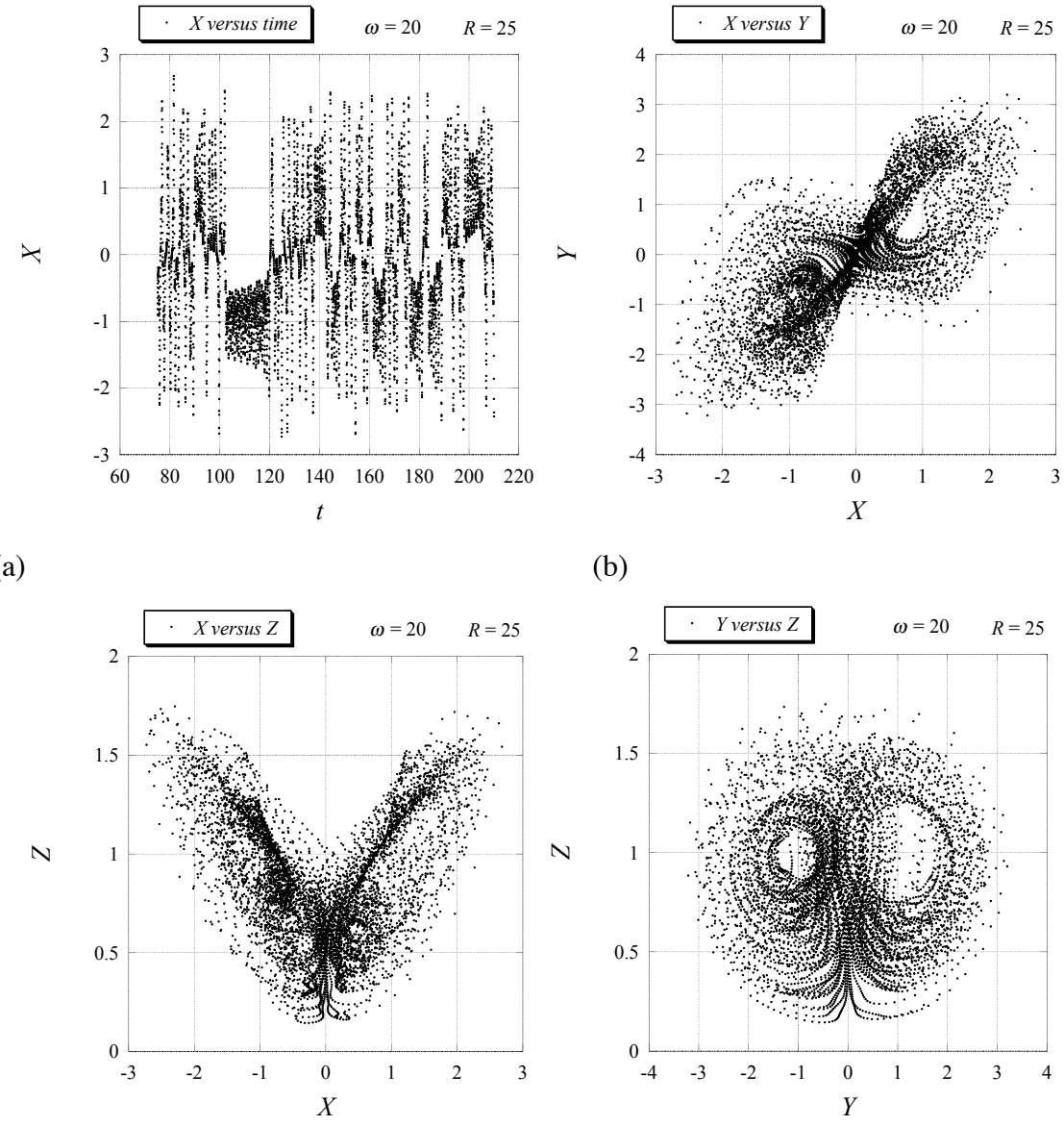

(a) (b)

(c) (d)

Figure 5.11: Graphical description of the solutions for $\omega = 20, R = 25$: (a) The amplitude X in the time domain, i.e. X versus t, (b), (c)and (d) The solution on a phase diagram: projections of the solution on the $X-Y$, $X-Z$ and $Y-Z$ planes, respectively.

© University of Pretoria

As the value of the scaled Rayleigh number changes, there are anticipated changes in the solutions. However, a particular interesting parameter window exists in the neighbourhood of $R = 75$. When there are no forced vibrations, the chaotic solution becomes periodic in this region. It becomes therefore interesting to observe how forced vibrations affect this periodic window. The results of the periodic solution obtained when there are no forced vibrations, i.e. for $\omega = 0$, are presented in Figure 5.12. The corresponding results when forced vibrations are applied at a frequency of $\omega = 5$ show a transition to chaos, as presented in Figure 5.13.

As previously shown with a scaled Rayleigh number R = 25, the frequency is increased and the solution observed now for a Rayleigh number R = 75. At a frequency $\omega = 6.5$ and scaled Rayleigh number R = 75, the solution becomes periodic, as presented in Figure 5.14. Increasing the frequency further to $\omega = 8$ the solution transitions to chaotic again, as presented in Figure 5.15. Further increase of the frequency returns the solution to periodic, as presented in Figure 5.16 with a $\omega = 25.2$. A similar result is presented in Figure 5.17 when the frequency is raised to $\omega = 26$ and again a periodic solution is seen. An interesting result is presented at a frequency $\omega = 28.5$ in Figure 5.18, where the solution seems to represent a chaotic or quasi-periodic one. As mentioned earlier, it is hard to distinguish between the two and will be discussed later when evaluating the Lyapunov exponents.

The sensitivity of the frequency is seen when it is taken at $\omega = 28.515$ and the solution presented in Figure 5.19 shows a chaotic result transforming into what seems to be a periodic solution.

Increasing the frequency to $\omega = 44$ and $\omega = 45.9$ presented in Figures 5.20 and 5.21, respectively, shows a periodic solution for both. Further, at a frequency of $\omega = 46$ the solution seems to change from periodic to chaotic or quasi-periodic, as presented in Figure 5.22. The transformation from chaotic to periodic and back is evident from the results shown. Finally, at a frequency $\omega = 100$, the solution is chaotic or quasi-periodic as presented in Figure 5.23. Although in this solution, it is more likely from Figure 5.23 that it is quasi-periodic, this must be verified by evaluating the Lyapunov exponents before a conclusive interpretation can be made.

© University of Pretoria

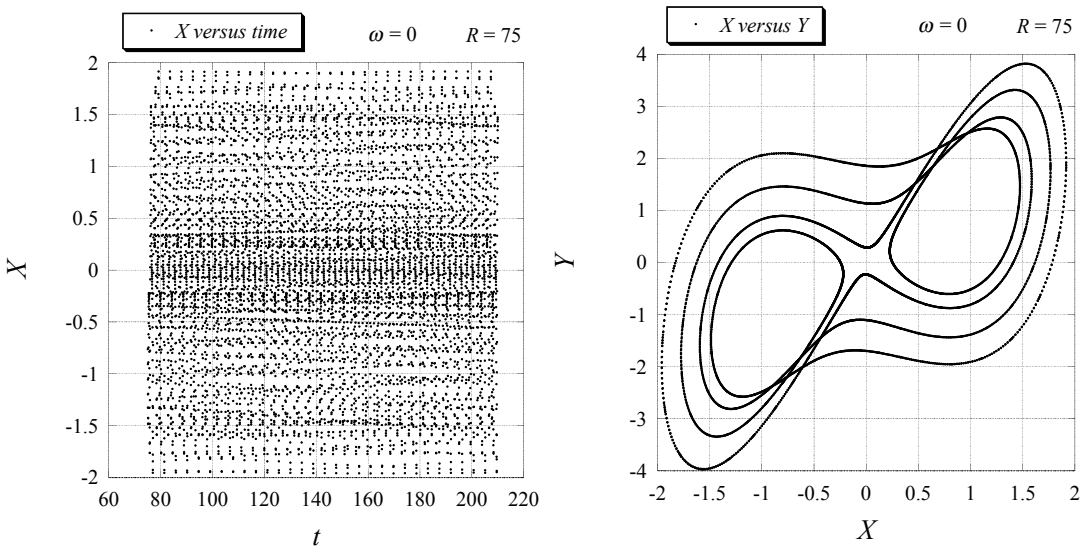

(a) (b)

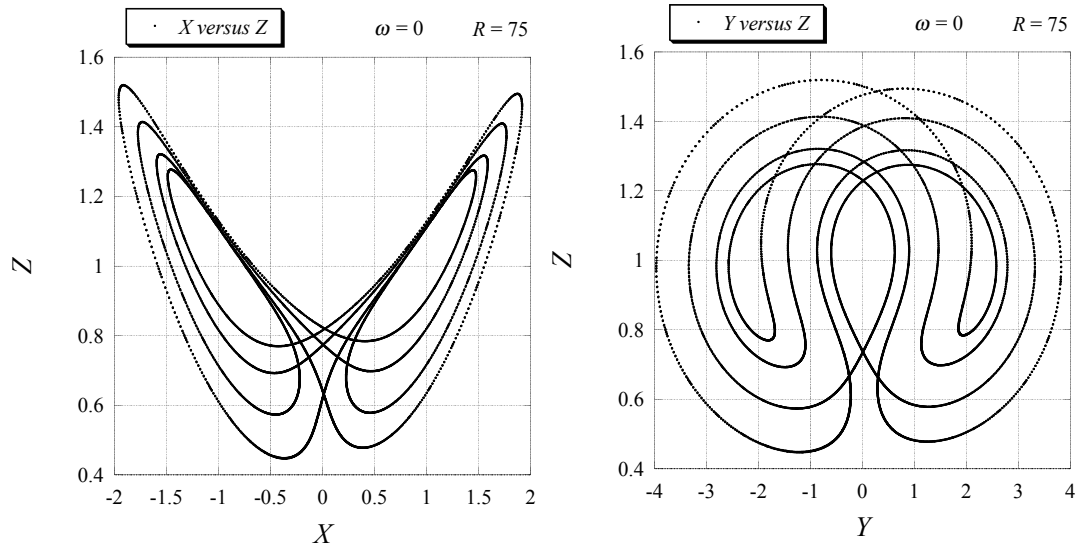

(c) (d)

Figure 5.12: Graphical description of the solutions for $\omega = 0, R = 75$: (a) The amplitude X in the time domain, i.e. X versus t , (b), (c) and (d) The solution on a phase diagram: projections of the solution on the $X-Y$, $X-Z$ and $Y-Z$ planes, respectively.

© University of Pretoria

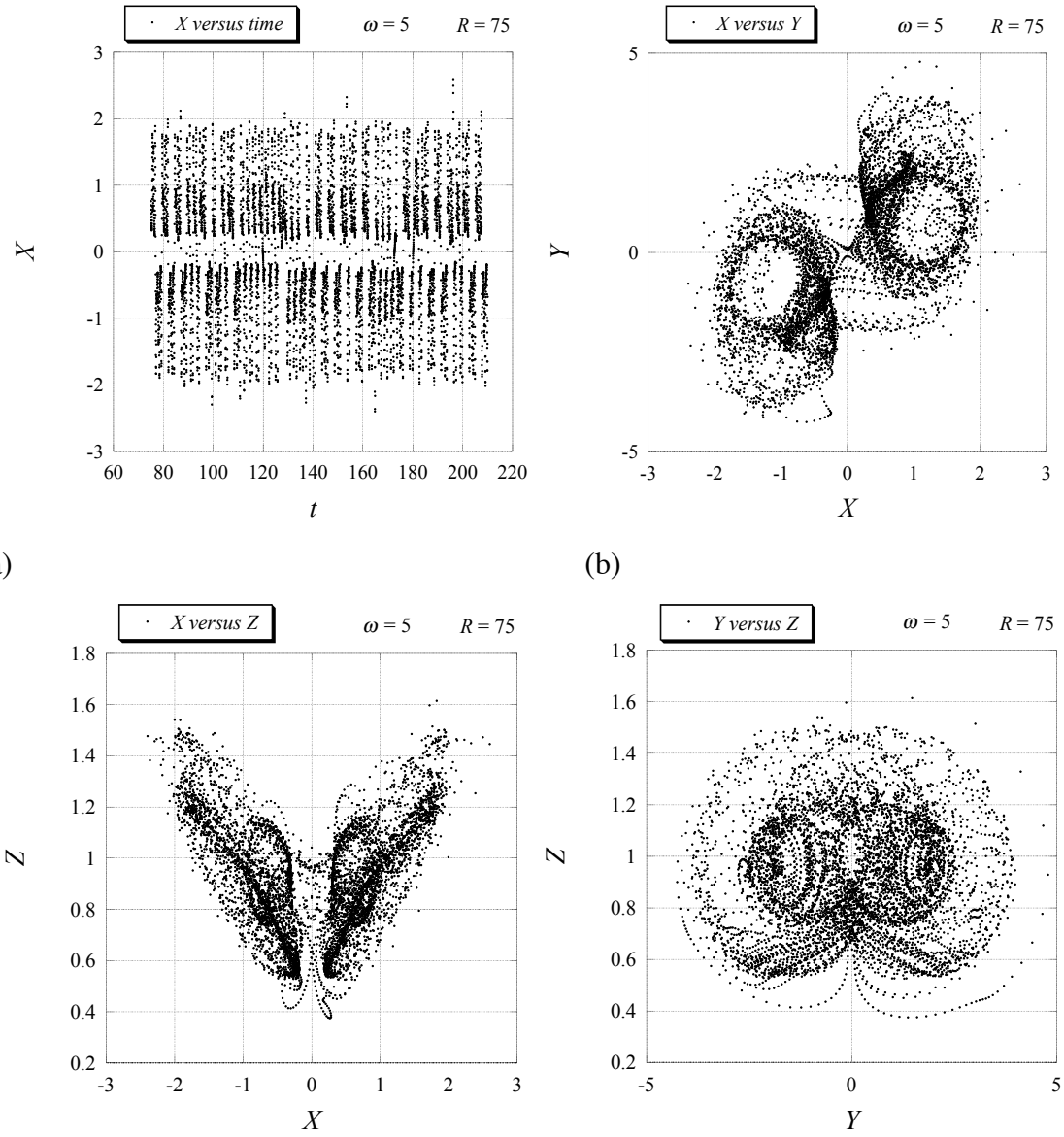

Figure 5.13: Graphical description of the solutions for $\omega = 5, R = 75$: (a) The amplitude X in the time domain, i.e. X versus t , (b), (c) and (d) The solution on a phase diagram: projections of the solution on the $X-Y$, $X-Z$ and $Y-Z$ planes, respectively.

© University of Pretoria

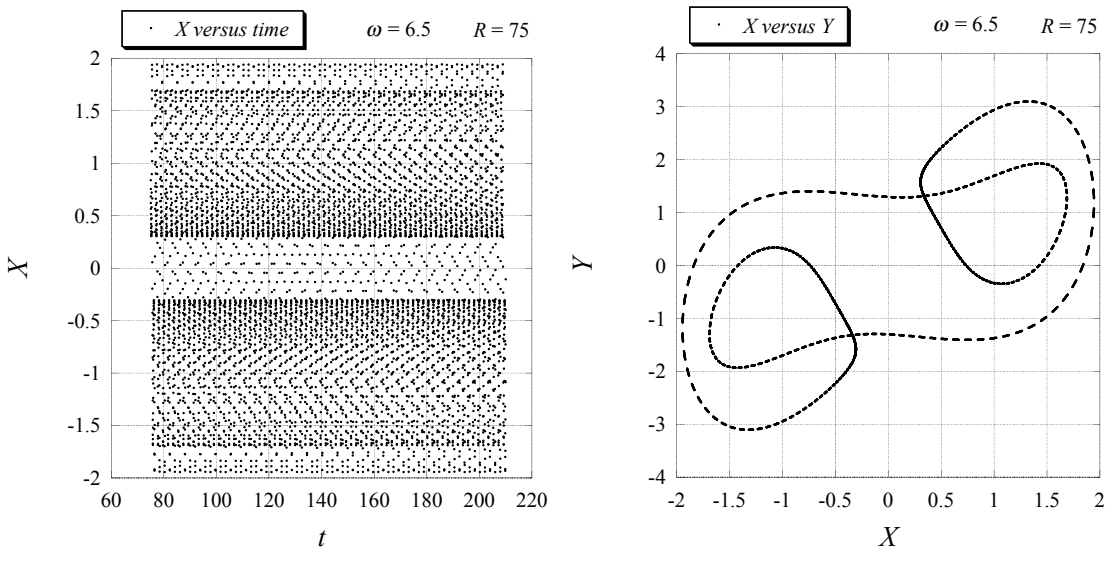

(a) (b)

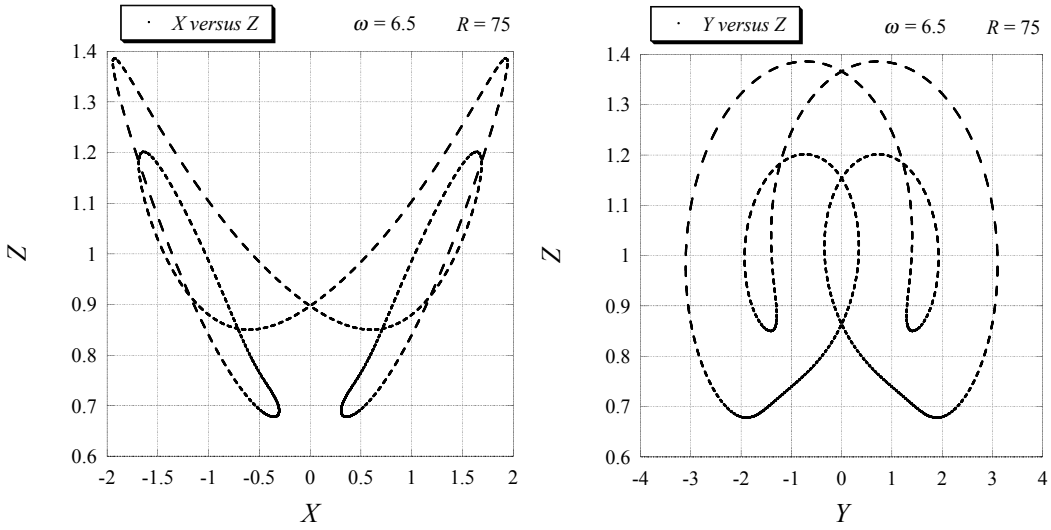

(c) (d)

Figure 5.14: Graphical description of the solutions for $\omega = 6.5, R = 75$: (a) The amplitude X in the time domain, i.e. X versus t, (b), (c) and (d) The solution on a phase diagram: projections of the solution on the $X-Y$, $X-Z$ and $Y-Z$ planes, respectively.

© University of Pretoria

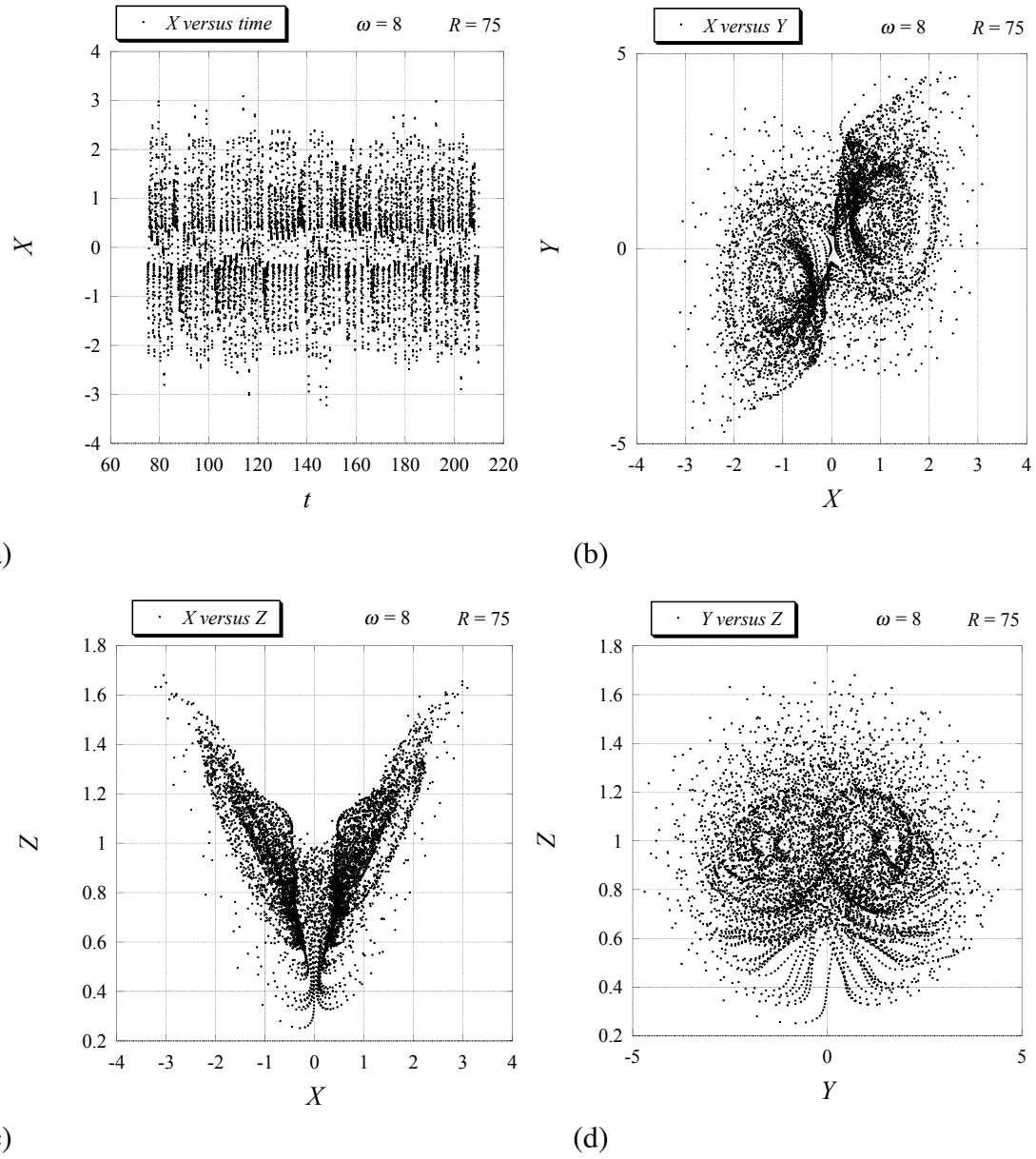

Figure 5.15: Graphical description of the solutions for $\omega = 8, R = 75$: (a) The amplitude X in the time domain, i.e. X versus t , (b), (c) and (d) The solution on a phase diagram: projections of the solution on the $X-Y$, $X-Z$ and $Y-Z$ planes, respectively.

© University of Pretoria

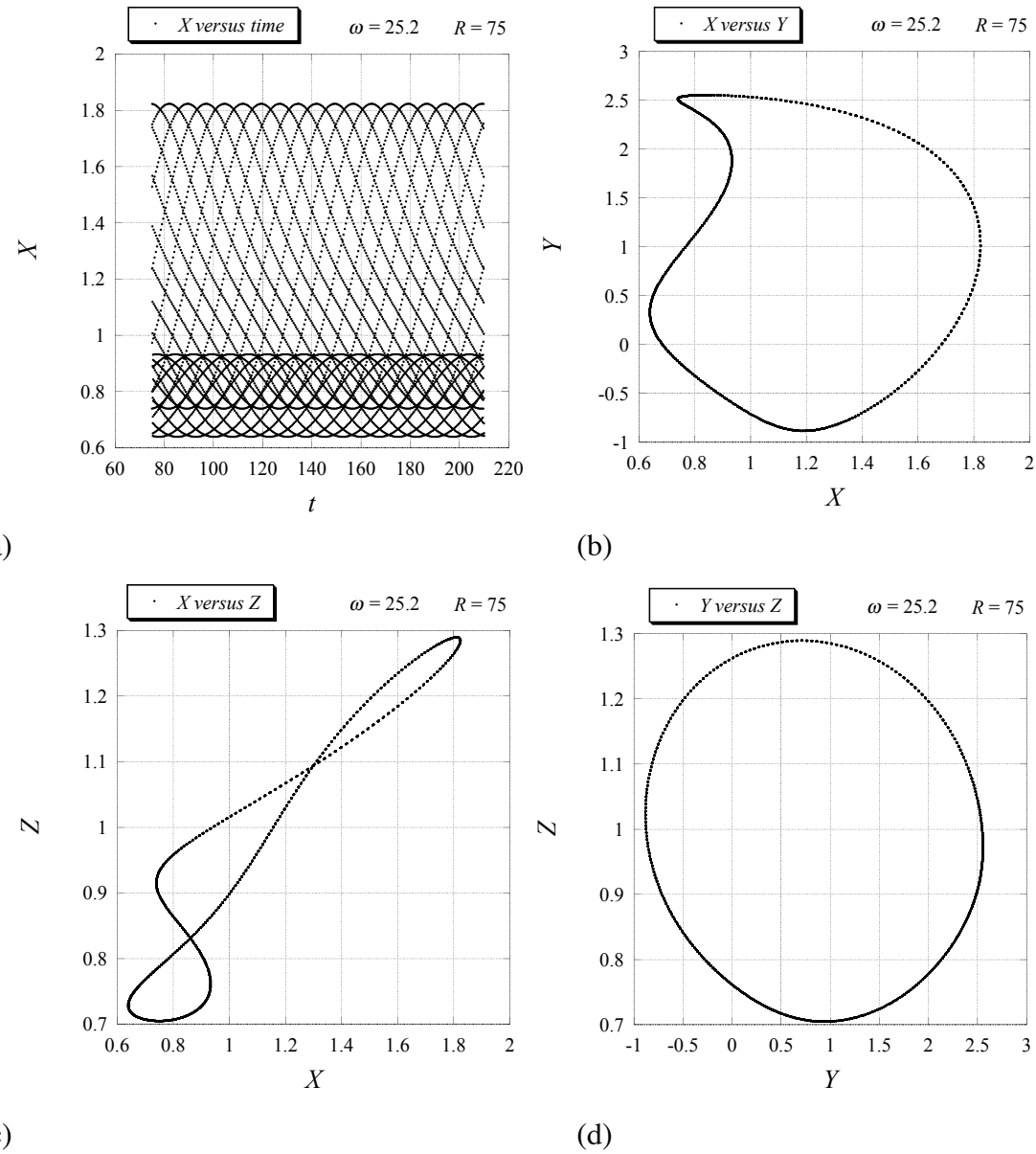

Figure 5.16: Graphical description of the solutions for $\omega = 25.2, R = 75$: (a) The amplitude X in the time domain, i.e. X versus t, (b), (c) and (d) The solution on a phase diagram: projections of the solution on the $X-Y$, $X-Z$ and $Y-Z$ planes, respectively.

© University of Pretoria

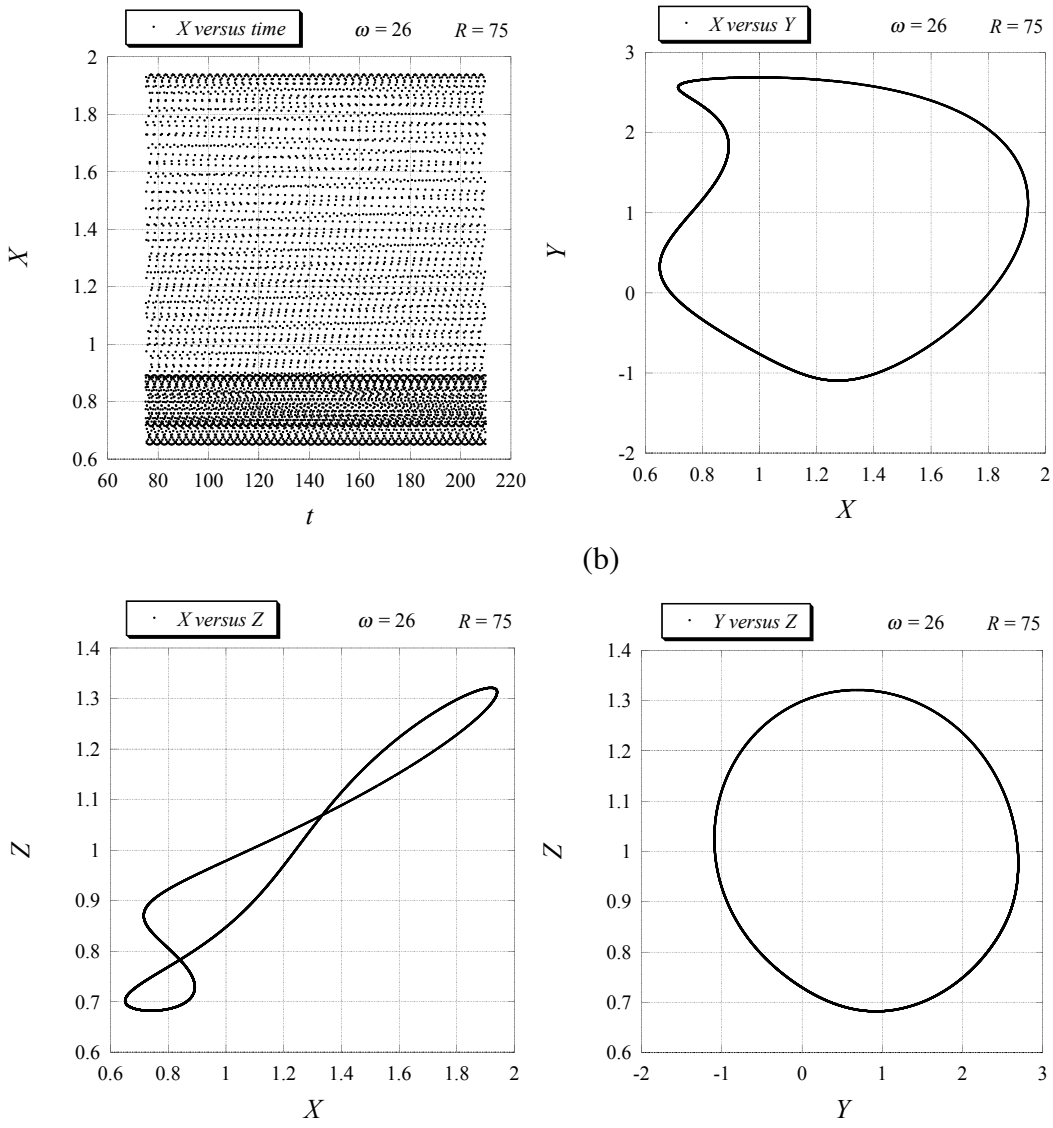

Figure 5.17: Graphical description of the solutions for $\omega = 26, R = 75$: (a) The amplitude X in the time domain, i.e. X versus t, (b), (c) and (d) The solution on a phase diagram: projections of the solution on the $X-Y$, $X-Z$ and $Y-Z$ planes, respectively.

© University of Pretoria

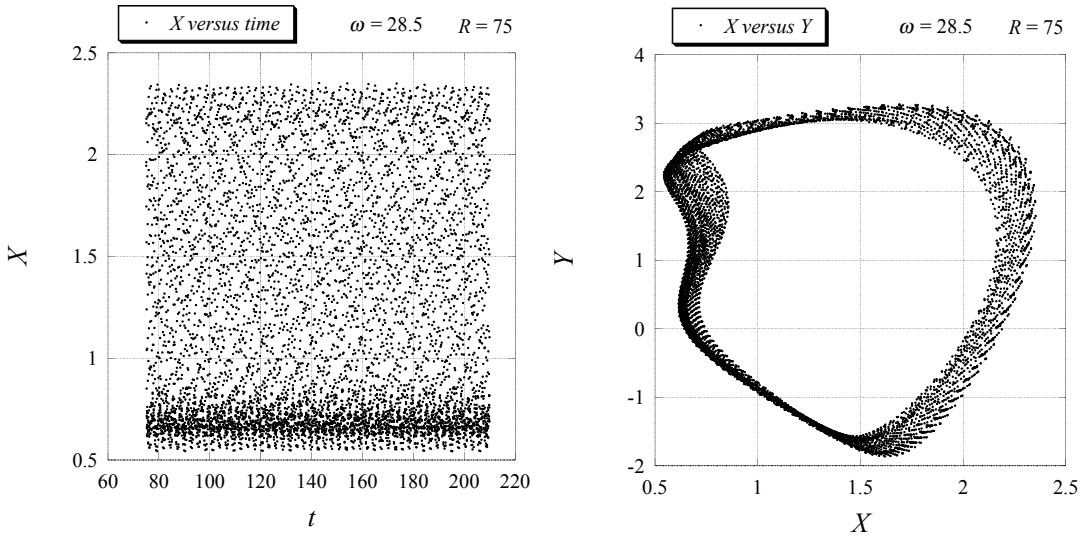

(a) (b)

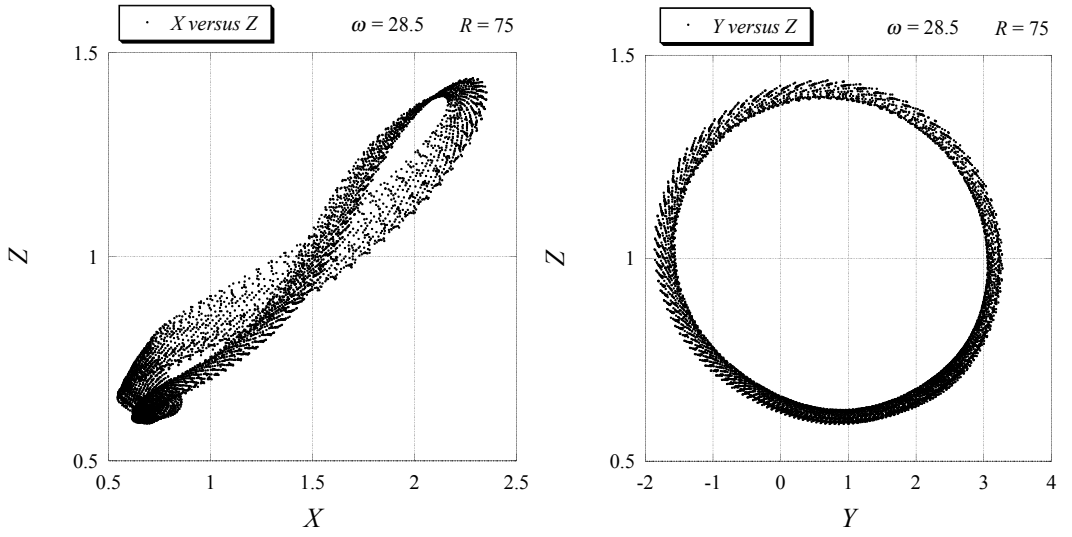

(c) (d)

Figure 5.18: Graphical description of the solutions for $\omega = 28.5, R = 75$: (a) The amplitude X in the time domain, i.e. X versus t, (b), (c) and (d) The solution on a phase diagram: projections of the solution on the $X-Y$, $X-Z$ and $Y-Z$ planes, respectively.

© University of Pretoria

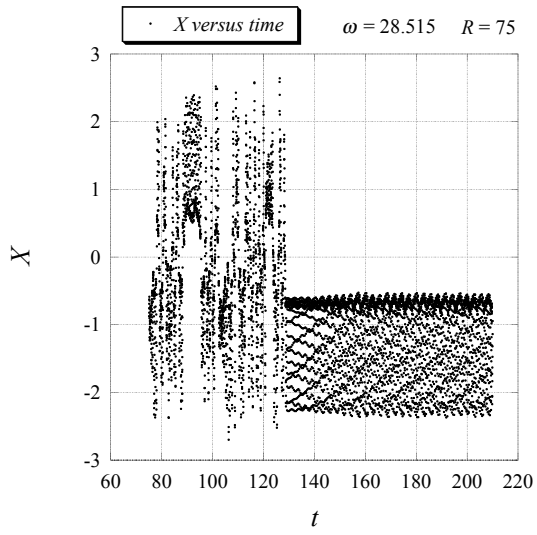

(a)

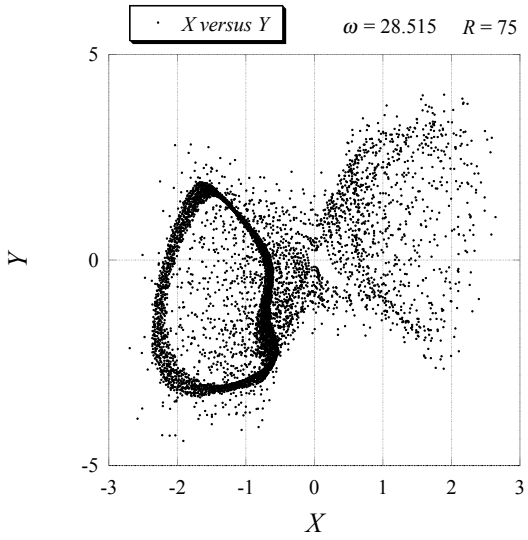

(b)

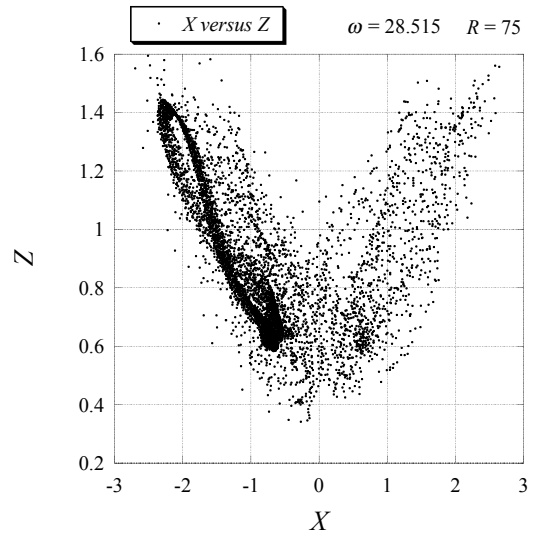

(c)

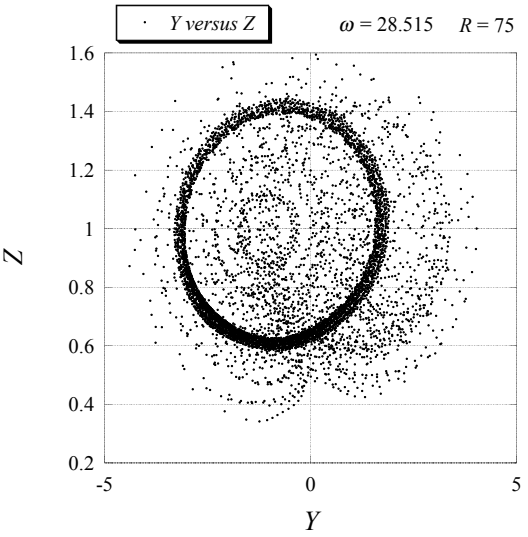

(d)

Figure 5.19: Graphical description of the solutions for $\omega = 28.515, R = 75$: (a) The amplitude X in the time domain, i.e. X versus t, (b), (c) and (d) The solution on a phase diagram: projections of the solution on the $X-Y$, $X-Z$ and $Y-Z$ planes, respectively.

© University of Pretoria

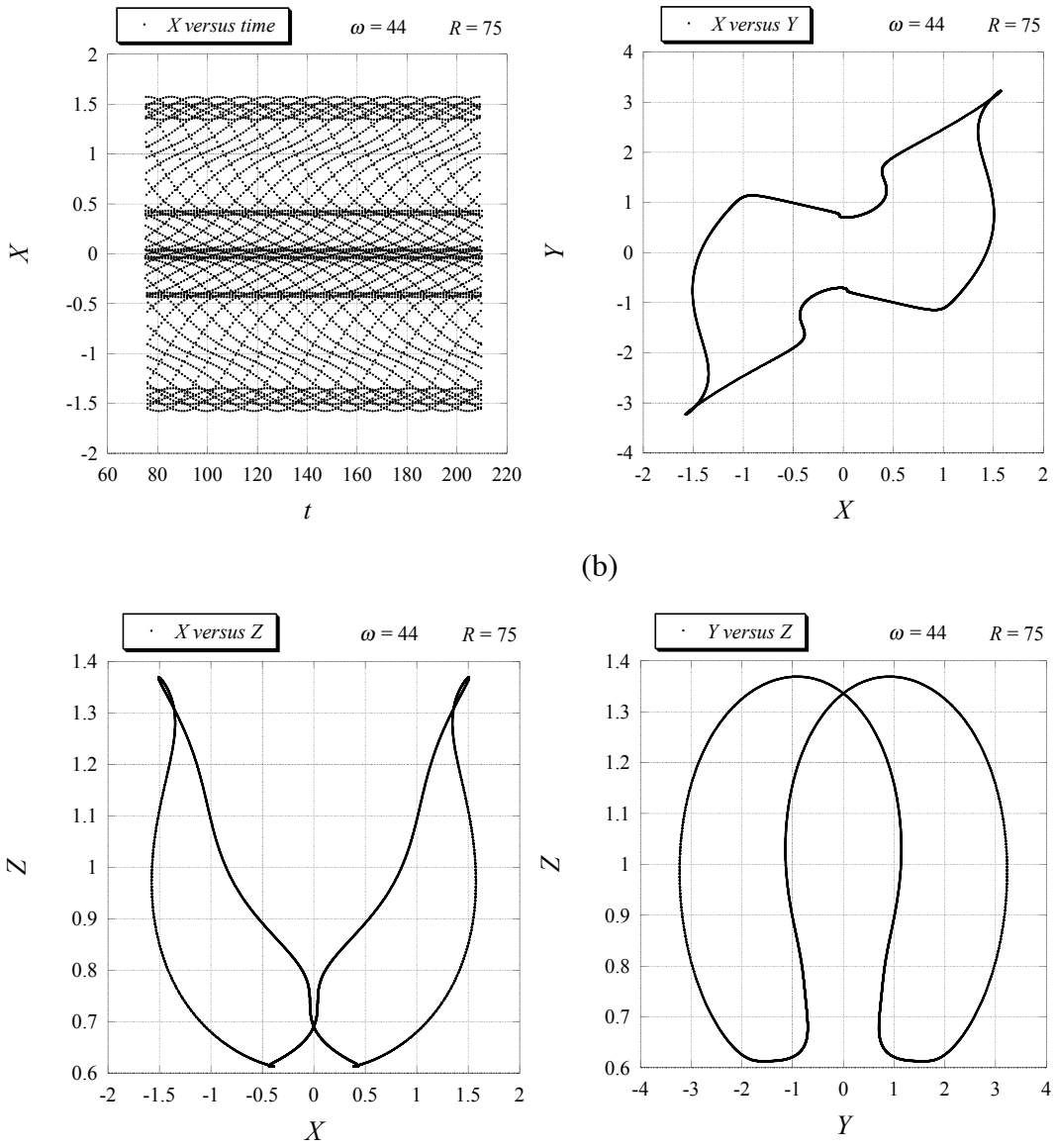

(a) (b)

(c) (d)

Figure 5.20: Graphical description of the solutions for $\omega = 44, R = 75$: (a) The amplitude X in the time domain, i.e. X versus t, (b), (c) and (d) The solution on a phase diagram: projections of the solution on the $X-Y$, $X-Z$ and $Y-Z$ planes, respectively.

© University of Pretoria

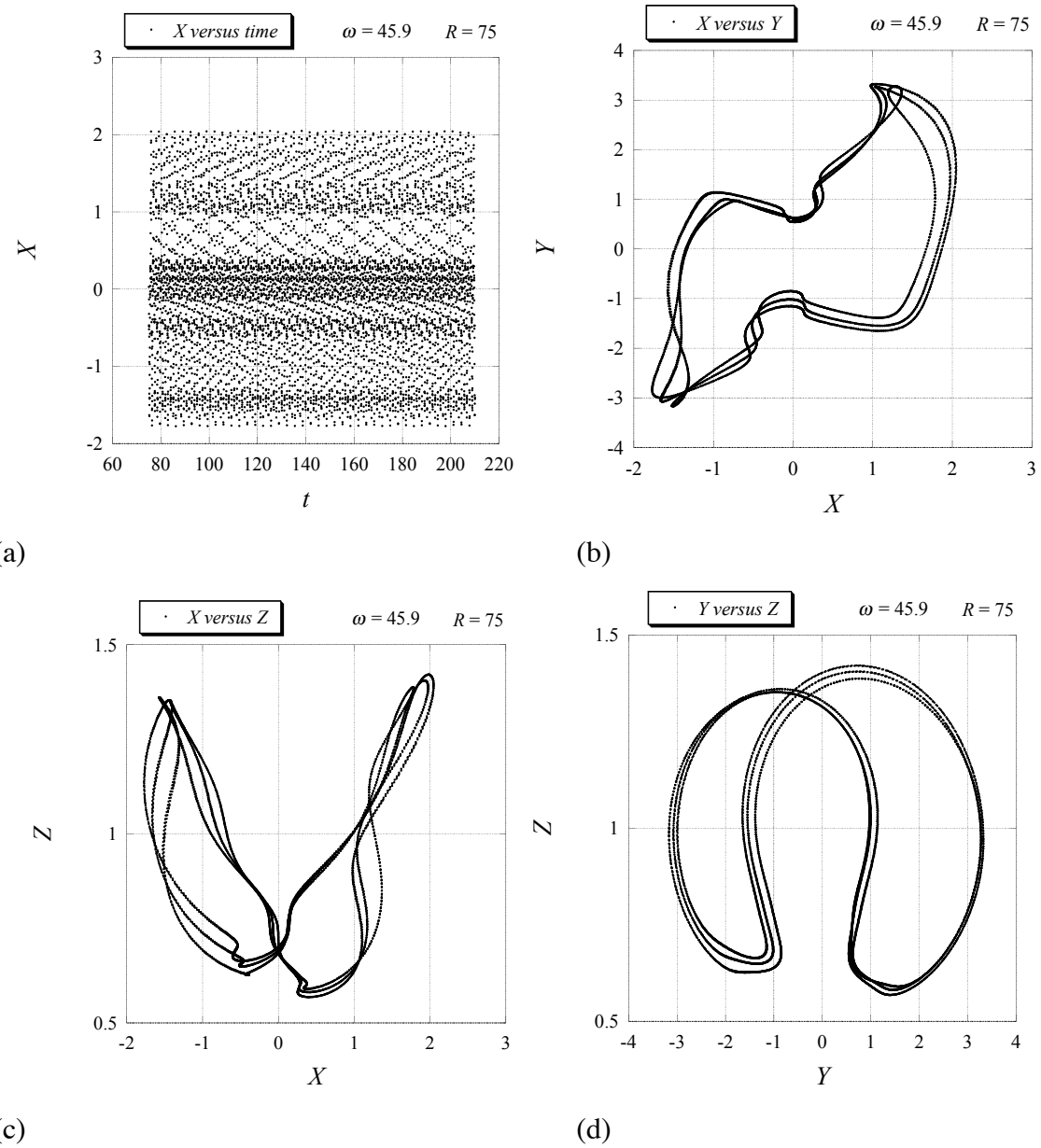

Figure 5.21: Graphical description of the solutions for $\omega = 45.9, R = 75$: (a) The amplitude X in the time domain, i.e. X versus t, (b), (c) and (d) The solution on a phase diagram: projections of the solution on the $X-Y$, $X-Z$ and $Y-Z$ planes, respectively.

© University of Pretoria

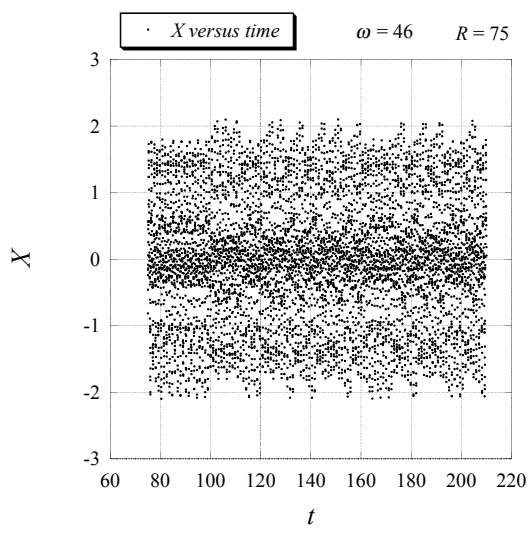

(a)

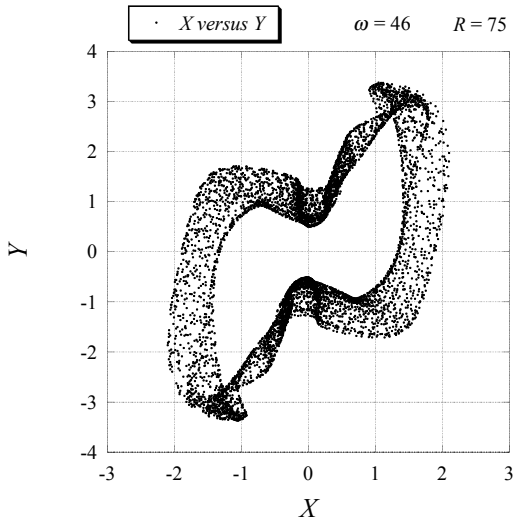

(b)

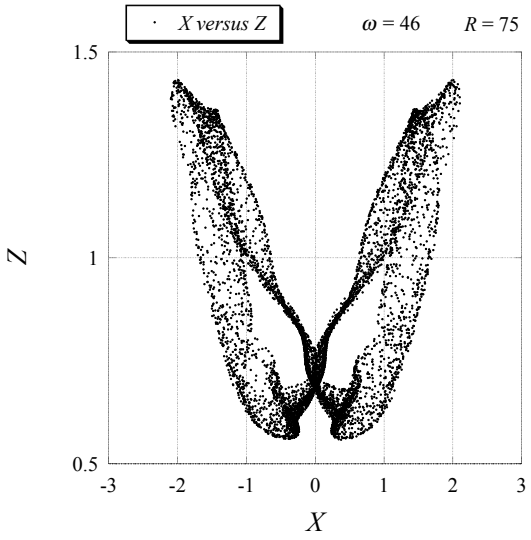

(c)

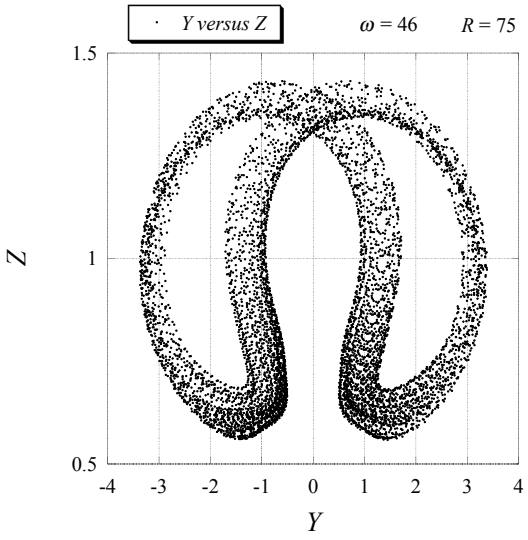

(d)

Figure 5.22: Graphical description of the solutions for $\omega = 46, R = 75$: (a) The amplitude X in the time domain, i.e. X versus t, (b), (c) and (d) The solution on a phase diagram: projections of the solution on the $X-Y$, $X-Z$ and $Y-Z$ planes, respectively.

© University of Pretoria

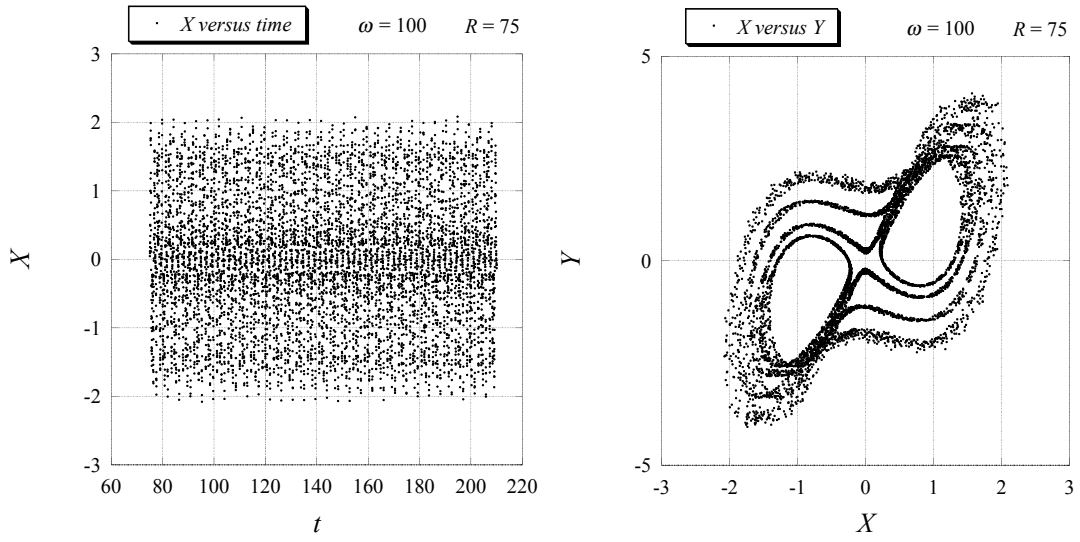

(a) (b)

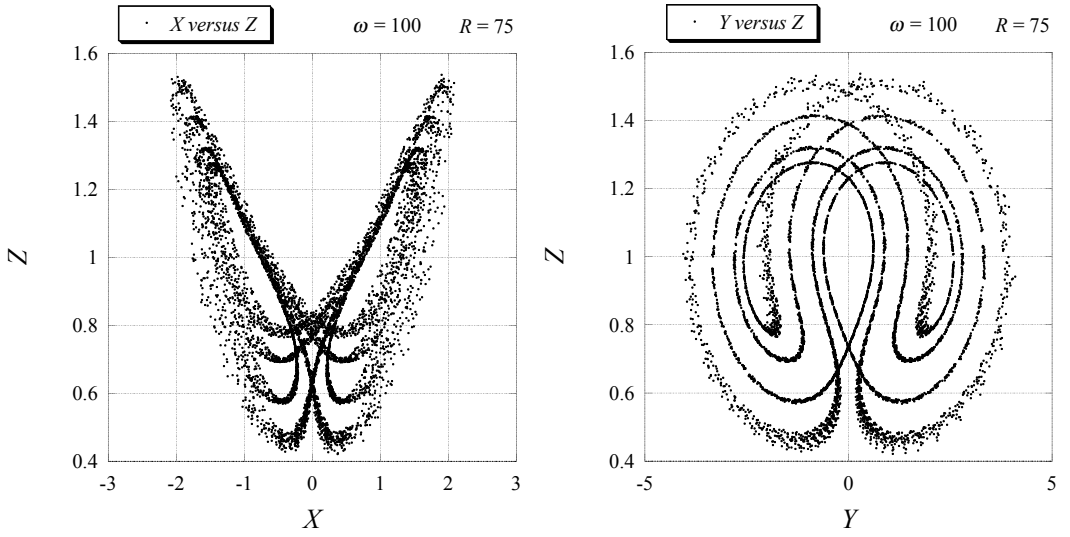

(c) (d)

Figure 5.23: Graphical description of the solutions for $\omega = 100, R = 75$: (a) The amplitude X in the time domain, i.e. X versus t, (b), (c) and (d) The solution on a phase diagram: projections of the solution on the $X-Y$, $X-Z$ and $Y-Z$ planes, respectively.

© University of Pretoria

5.2 Results for the Lyapunov exponents

The presentation in the previous section was used to demonstrate different types of results, such as periodic, quasi-periodic and chaotic. Stationary solutions (fixed points) cannot be obtained when there are forced vibrations. However, identifying accurately the distinction between periodic, quasi-periodic and chaotic orbits needs a more accurate tool. Therefore, the Lyapunov exponents will be evaluated and presented in this section. Generally, the results for the Lyapunov exponents are being presented as a function of R for different frequency values. However, firstly it becomes appealing to show the link between the Lyapunov exponents results and the graphical presentation in the previous section. Therefore, the results for different values of R at a constant frequency of $\omega = 6.5$ are being presented first.

Figure 5.24 shows the results for $\omega = 6.5$ and $R = 14$. This value of R would have caused steady convection if there were no forced vibrations, i.e. the solution would have stabilised at one of the fixed points. The critical value of R for this case is $R = 25$. When applying forced vibrations with a frequency $\omega = 6.5$, it is evident from Figure 5.24 that sub-critical periodic convection takes place. Increasing the value of R to $R = 17$ at the same frequency renders the solution chaotic as observed from Figure 5.25. A restoration of a periodic solution is observed in Figure 5.26 as the value of R increases further to $R = 20$.

In order to confirm these transitions by using the Lyapunov exponents, the results of evaluating the Lyapunov exponents for $\omega = 6.5$ as a function of R are presented in Figure 5.27. While four distinct values of Lyapunov exponents exist, each related to one of the dependent variables X, Y, Z and W, the Lyapunov exponent associated with W is not relevant it changes monotonically in time. Therefore, one would pay attention to the other three values of the Lyapunov exponents referred to as λ_1, λ_2 and λ_3 in the figures. From Figure 5.27 it is evident that no chaotic solutions exist for R values less than $R = 15$ as none of the Lyapunov exponents are positive. Non-positive values of Lyapunov exponents indicate either a fixed point (non-existent in the present case), a periodic or a quasi-periodic solution. At $R = 14$, one of the three relevant Lyapunov exponents is zero, while the other two are negative. Therefore, the solution is indeed periodic. At $R = 17$, Figure 5.27 shows that one of the Lyapunov exponents is positive indicating a chaotic solution, confirming the conclusion reached from Figure 5.25. At

© University of Pretoria

$R = 20$, Figure 5.27 suggests a periodic solution as one of the Lyapunov exponents is zero, confirming again the previous conclusions.

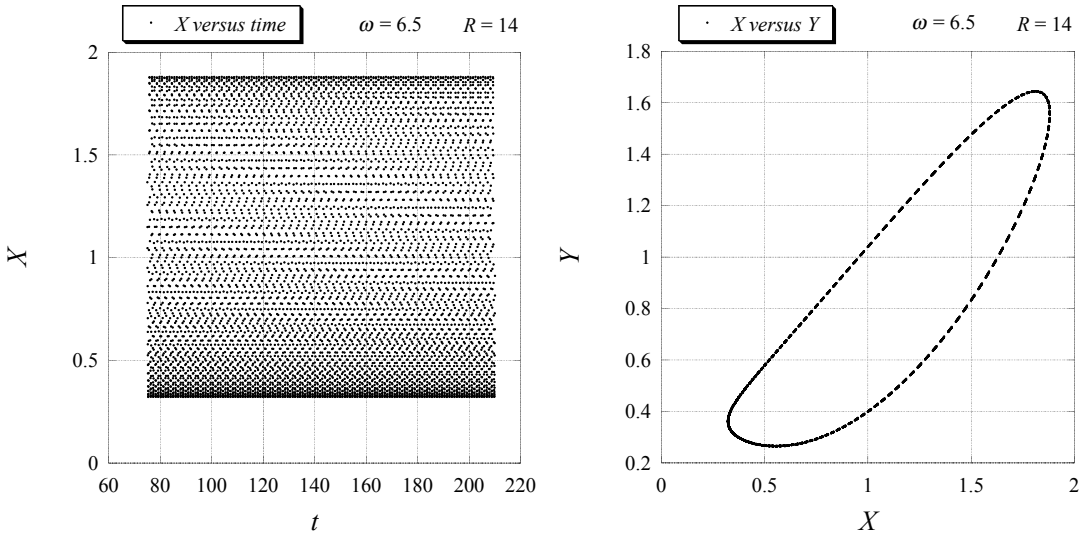

(a) (b)

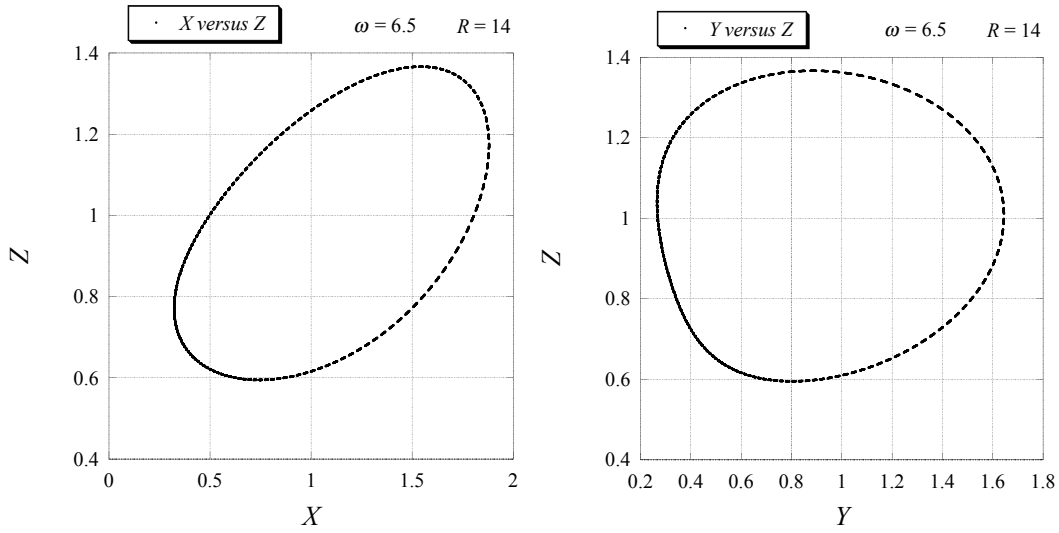

(c) (d)

Figure 5.24: Graphical description of the solutions for $\omega = 6.5, R = 14$: (a) The amplitude X in the time domain, i.e. X versus t, (b), (c) and (d) The solution on a phase diagram: projections of the solution on the $X-Y$, $X-Z$ and $Y-Z$ planes, respectively.

© University of Pretoria

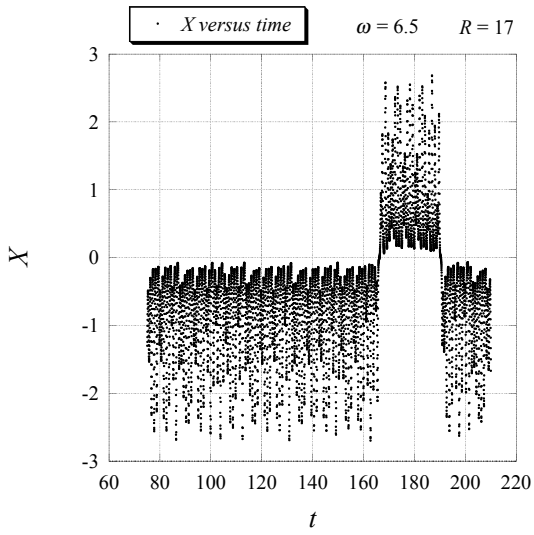

(a)

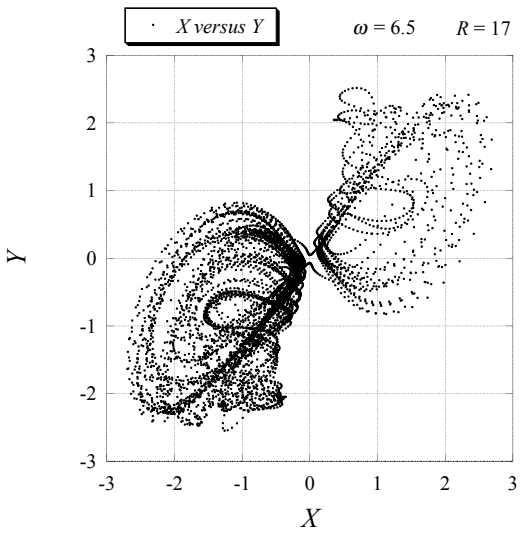

(b)

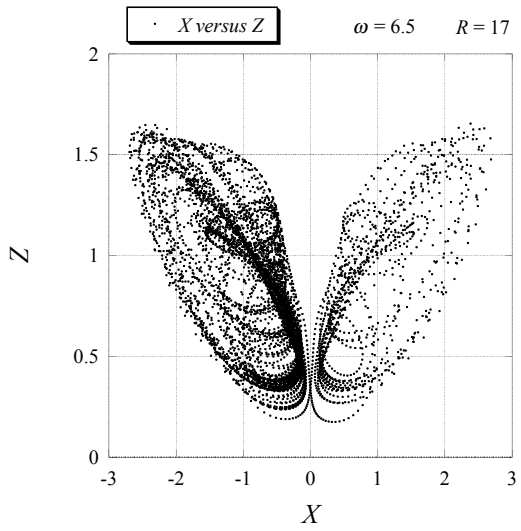

(c)

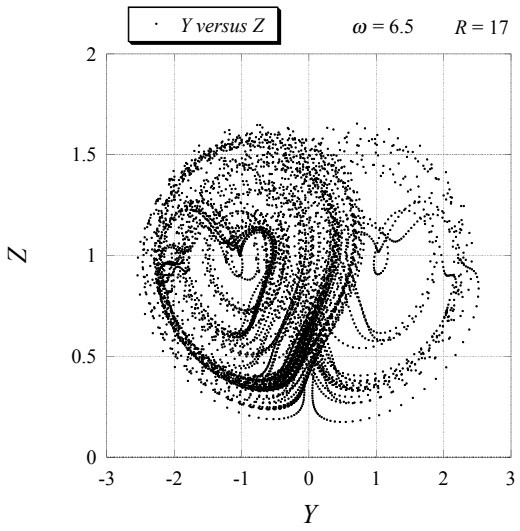

(d)

Figure 5.25: Graphical description of the solutions for $\omega = 6.5, R = 17$: (a) The amplitude X in the time domain, i.e. X versus t, (b), (c) and (d) The solution on a phase diagram: projections of the solution on the $X-Y$, $X-Z$ and $Y-Z$ planes, respectively.

© University of Pretoria

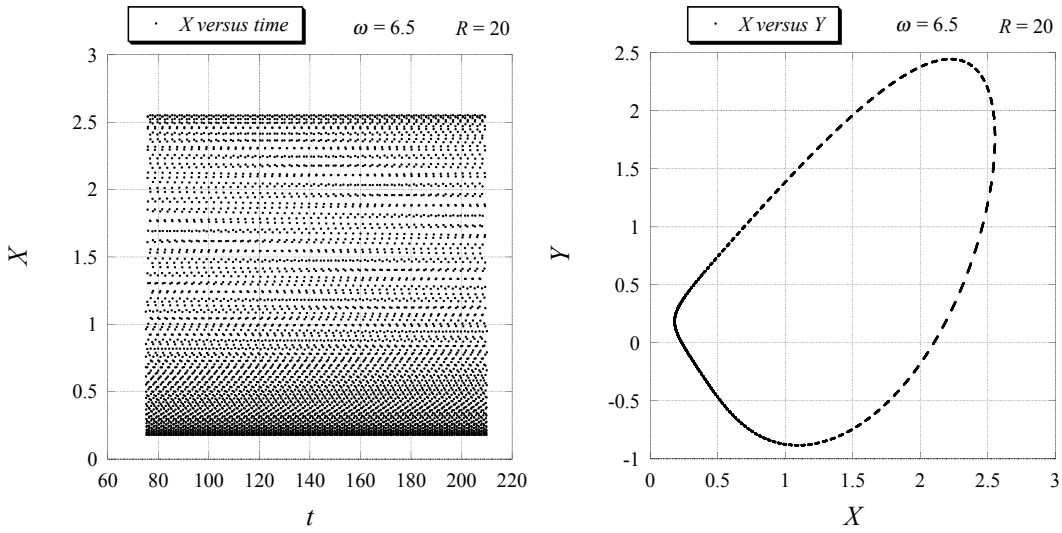

(a) (b)

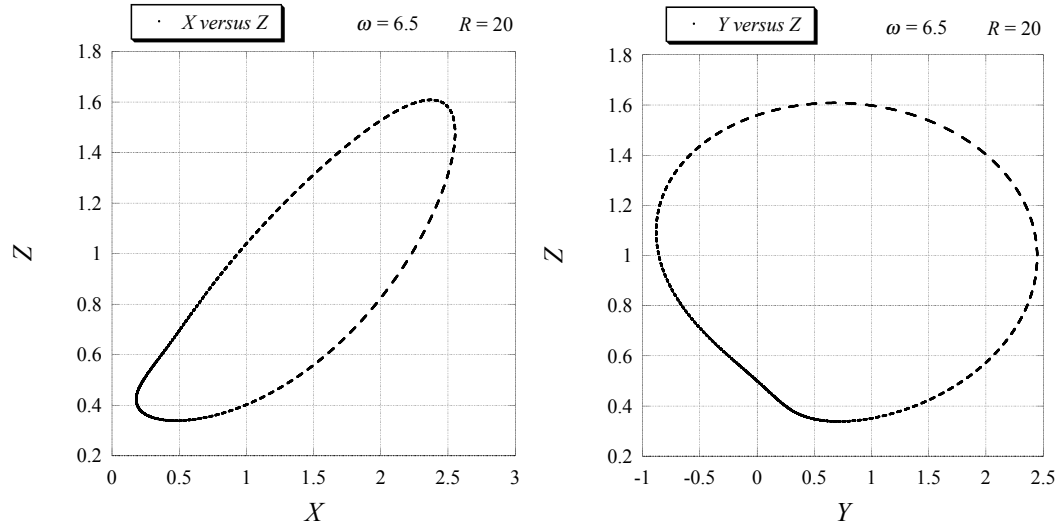

(c) (d)

Figure 5.26: Graphical description of the solutions for $\omega = 6.5, R = 20$: (a) The amplitude X in the time domain, i.e. X versus t, (b), (c) and (d) The solution on a phase diagram: projections of the solution on the $X-Y$, $X-Z$ and $Y-Z$ planes, respectively.

© University of Pretoria

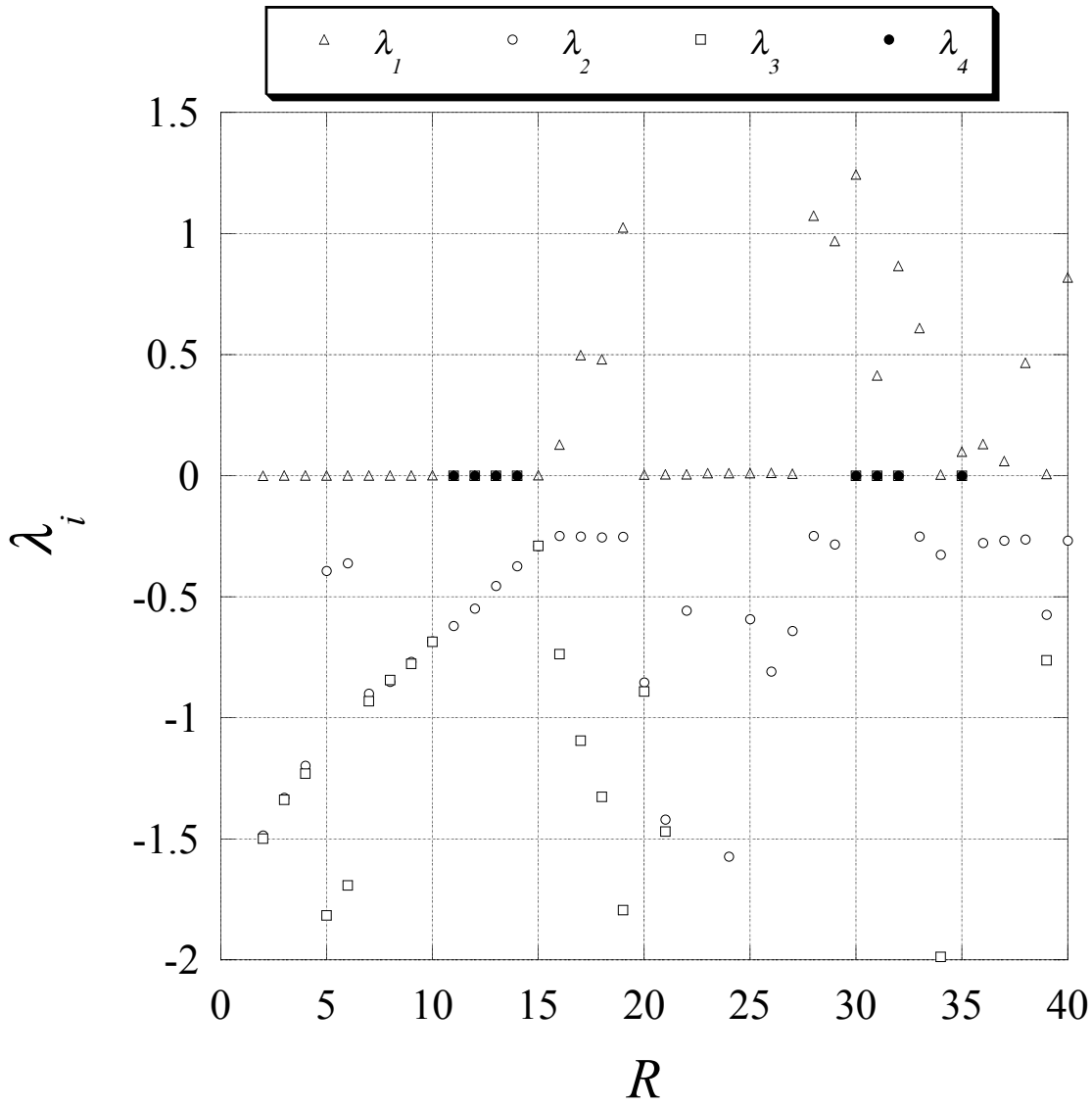

Figure 5.27: Graphical description of the Lyapunov exponents for $\omega = 6.5$.

© University of Pretoria

Figures 5.28 to 5.33 present the values of the Lyapunov exponents as a function of R for different values of ω. The range of R values used in these evaluations were $0 \le R \le 160$. The first graph in each figure shows the results over the whole range of R values. However, in order to zoom into the different sub-domains each figure shows the inset into the following sub-domain: $0 \le R \le 40$, $40 \le R \le 100$ and $100 \le R \le 160$. For reference purposes, the first result presented corresponds to conditions with no forced vibrations, i.e. for a frequency of $\omega = 0$, as observed in Figure 5.28. From Figure 5.28 it is evident that transition to a chaotic (weak turbulent) solution occurs at $R = 25$, a periodic window within the chaotic regime around $R = 75$, and a transition to periodic solutions for $R > 105$.

At a frequency $\omega = 8$, it is expected that the solution is periodic for R = 25 and chaotic for R =75, as seen in Figures 5.7 and 5.15, respectively. The results shown for the Lyapunov exponents at a frequency $\omega = 8$, presented in Figure 5.29, will confirm this. At R = 25 there are no positive Lyapunov exponents and so the solution is indeed periodic, and at R = 75, there is one positive Lyapunov exponent indicating a chaotic solution.

At a frequency $\omega = 26$, it is expected that the solution is periodic for R = 75, as seen in Figure 5.17. The results for the Lyapunov exponents at a frequency $\omega = 26$, presented in Figure 5.30, show one Lyapunov exponent at zero and the other two negative. Therefore, the solution is periodic.

At a frequency $\omega = 28.5$, the solution is chaotic or quasi-periodic for R = 75, as seen in Figure 5.18. The results for the Lyapunov exponents, at a frequency $\omega = 28.5$ are presented in Figure 5.31. Observing the Lyapunov exponents at R = 75, one positive indicating a chaotic solution is shown. As discussed previously, although the solution may seem to be quasi-periodic, only the Lyapunov exponents can confirm the solution. As presented here in Figure 5.31, the solution at R = 75 is chaotic.

For Figures 5.32 and 5.33 with frequencies $\omega = 46$ and $\omega = 100$, respectively, a similar result is observed at R = 75. The results presented in Figures 5.22 and 5.23 were either chaotic or quasi-periodic. Figures 5.32 and 5.33 both show one positive Lyapunov exponent at R = 75 indicating a chaotic solution. Again a solution that may have been thought to be quasi-periodic is shown to be chaotic, as proved by the Lyapunov exponents.

© University of Pretoria

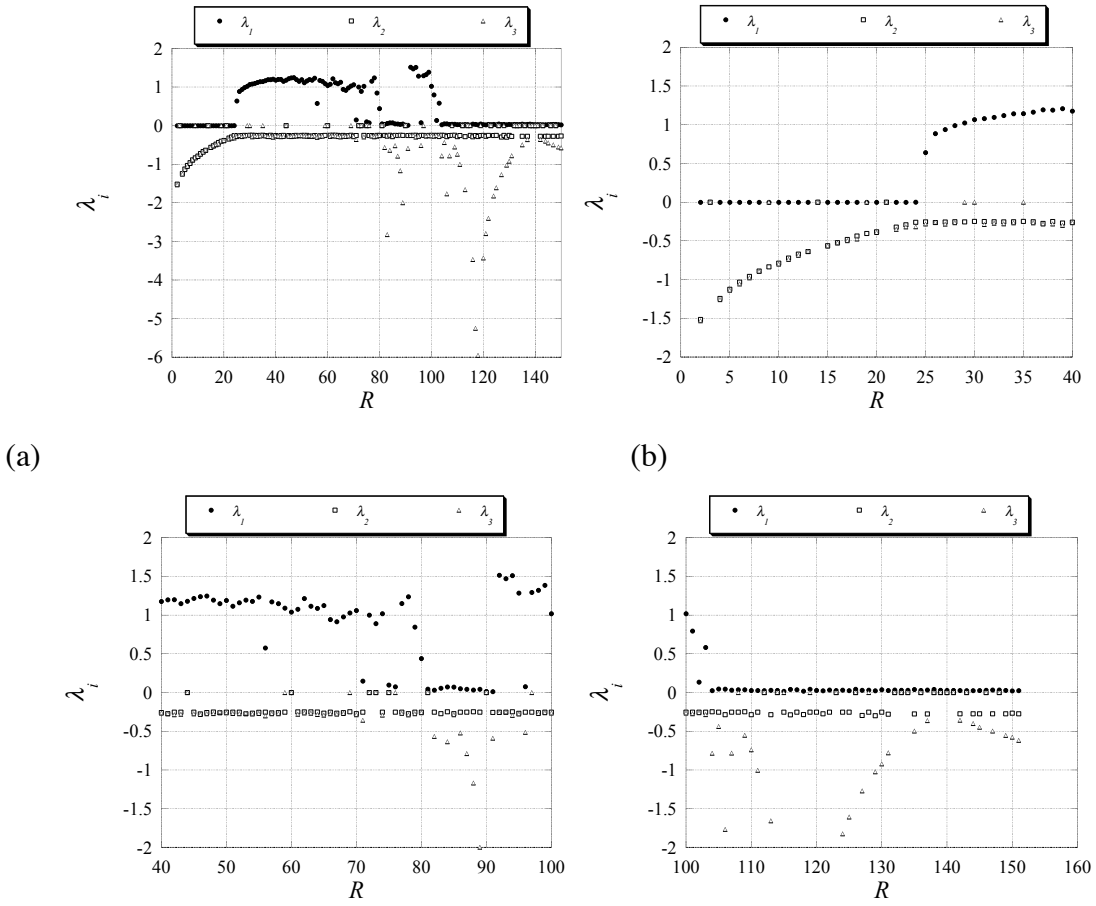

Figure 5.28: Graphical description of the Lyapunov exponents for $\omega = 0$.

© University of Pretoria

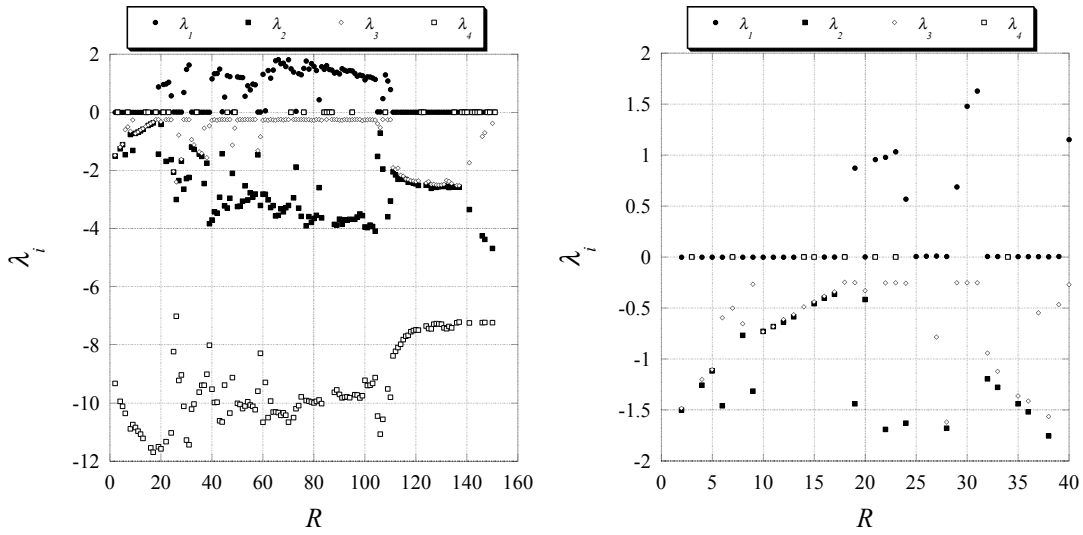

(a) (b)

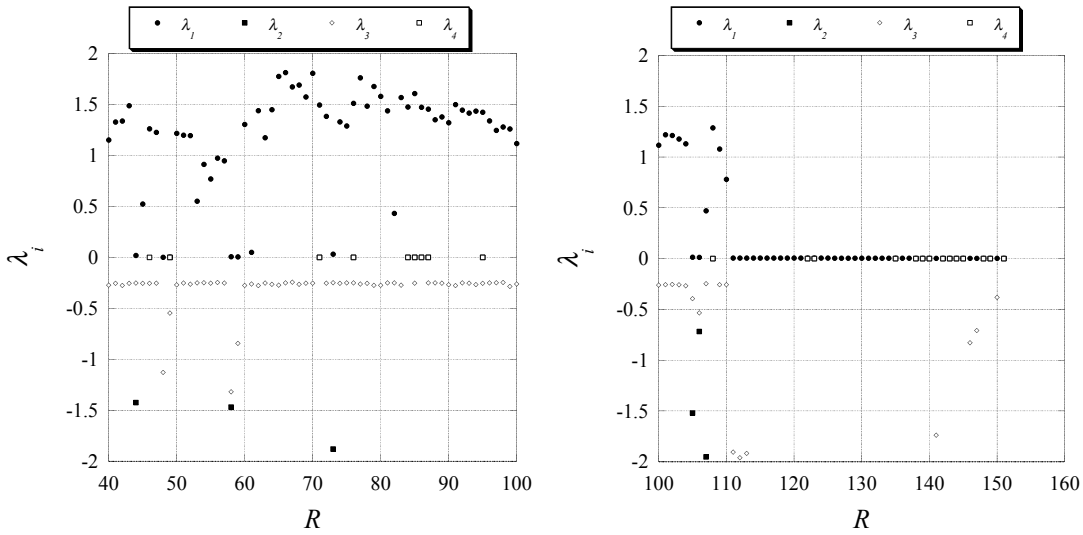

(c) (d)

Figure 5.29: Graphical description of the Lyapunov exponents for $\omega = 8$.

© University of Pretoria

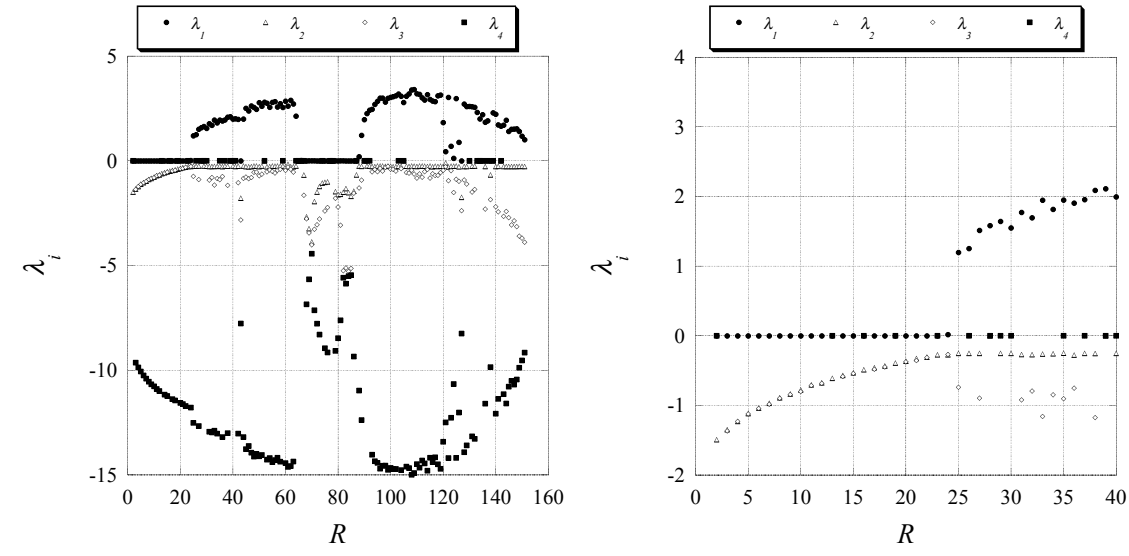

(a)

(b)

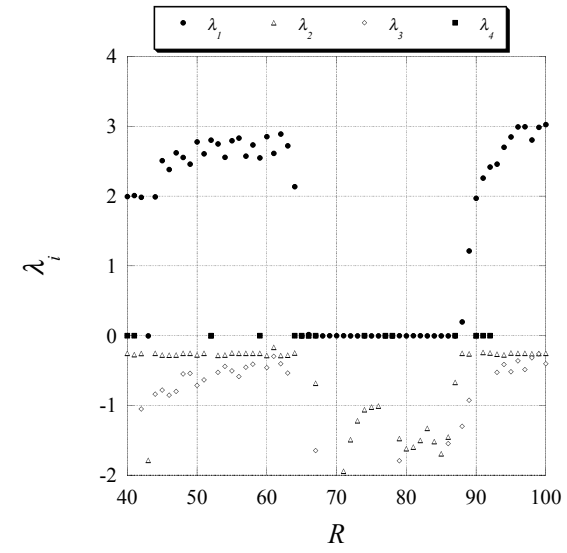

(c)

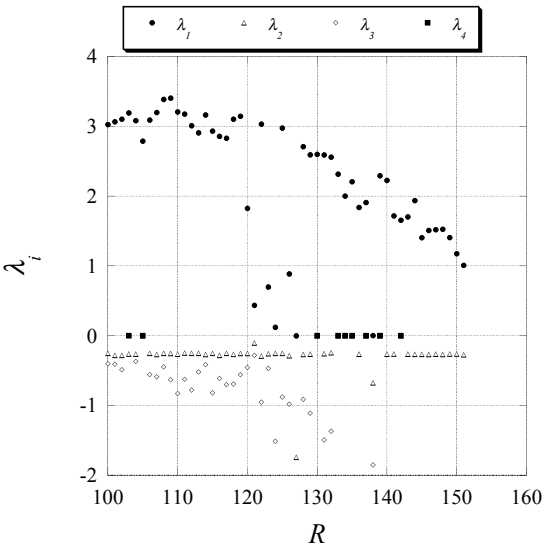

(d)

Figure 5.30: Graphical description of the Lyapunov exponents for $\omega = 26$.

© University of Pretoria

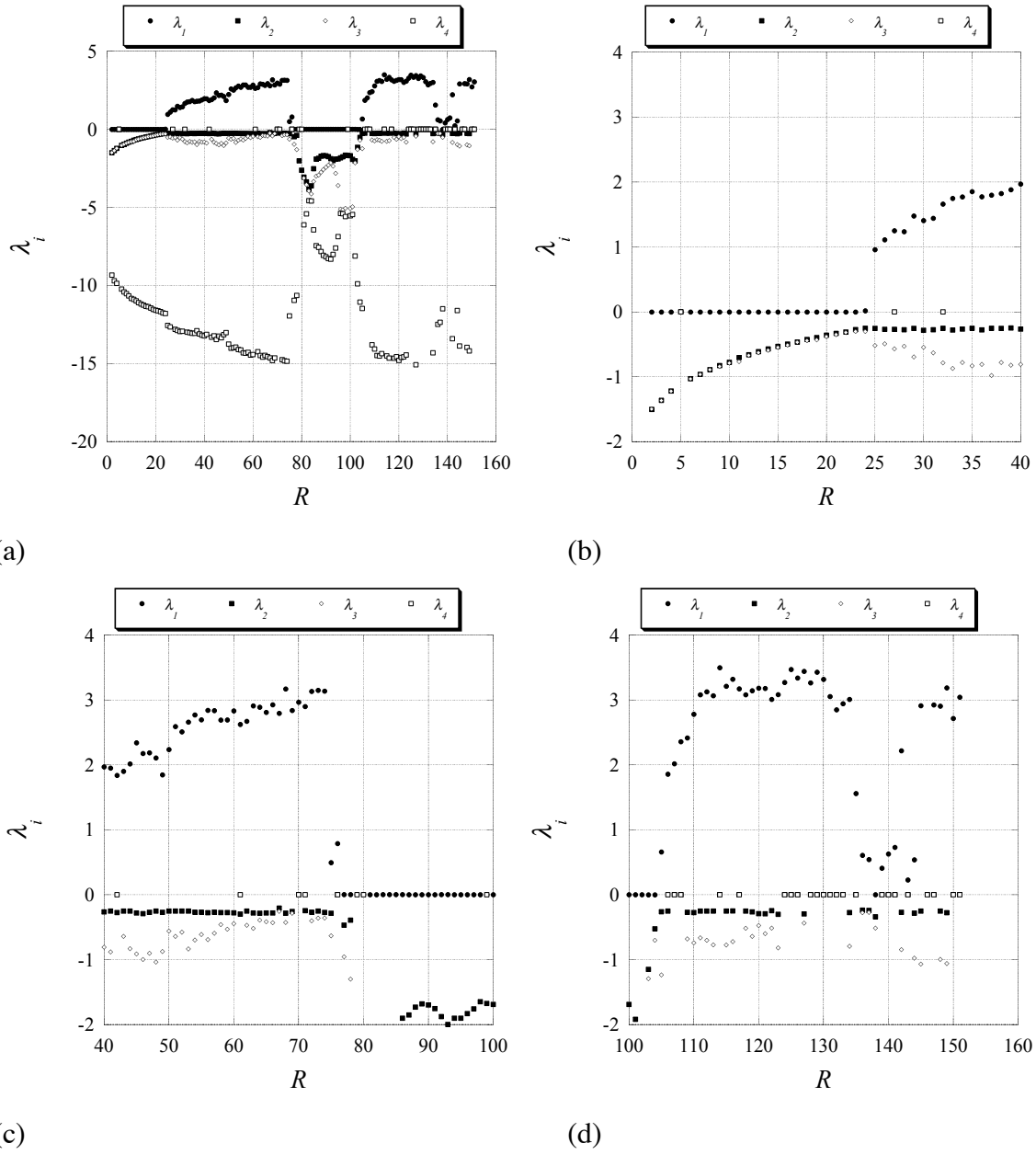

Figure 5.31: Graphical description of the Lyapunov exponents for $\omega = 28.5$.

© University of Pretoria

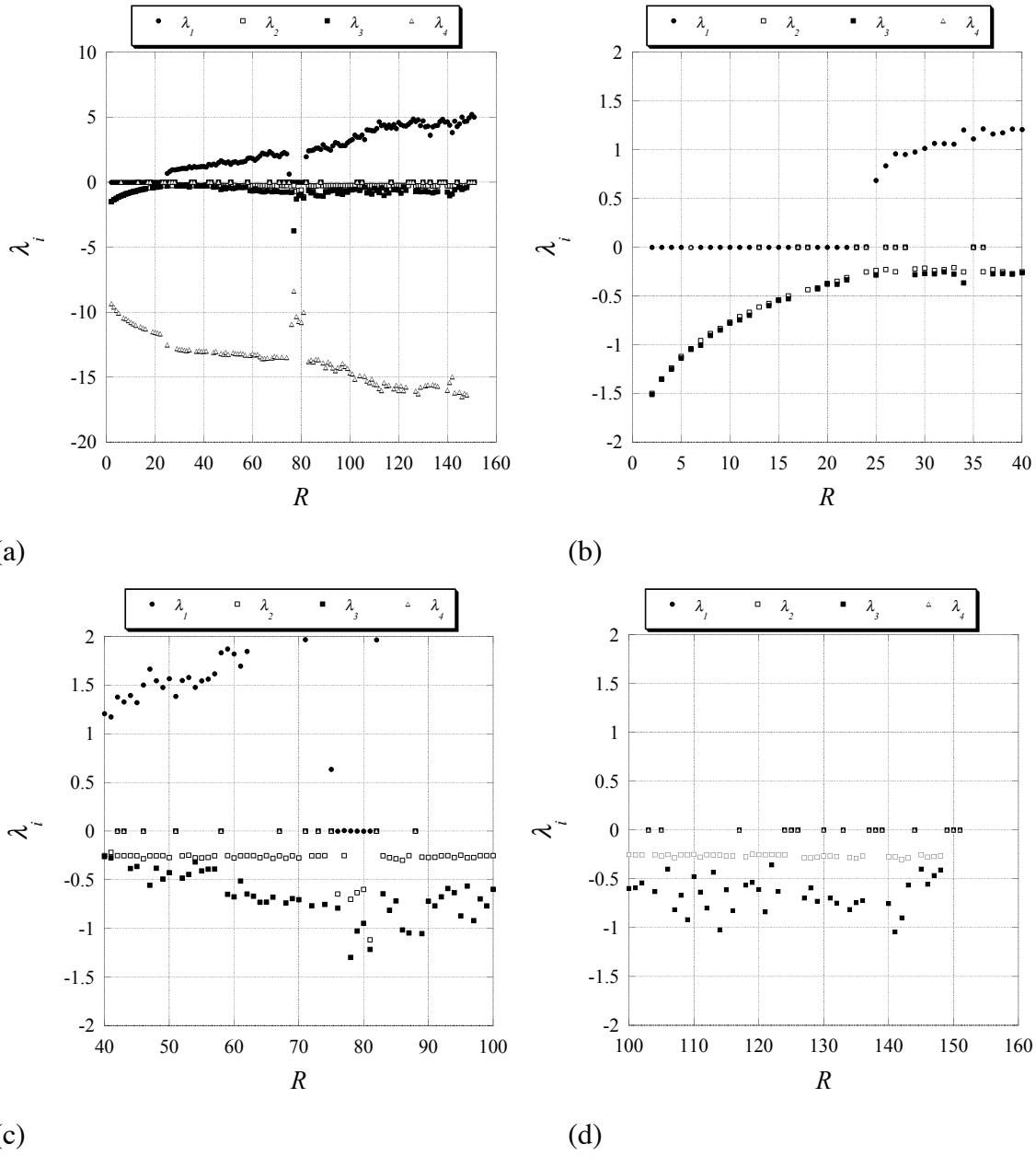

Figure 5.32: Graphical description of the Lyapunov exponents for $\omega = 46$.

© University of Pretoria

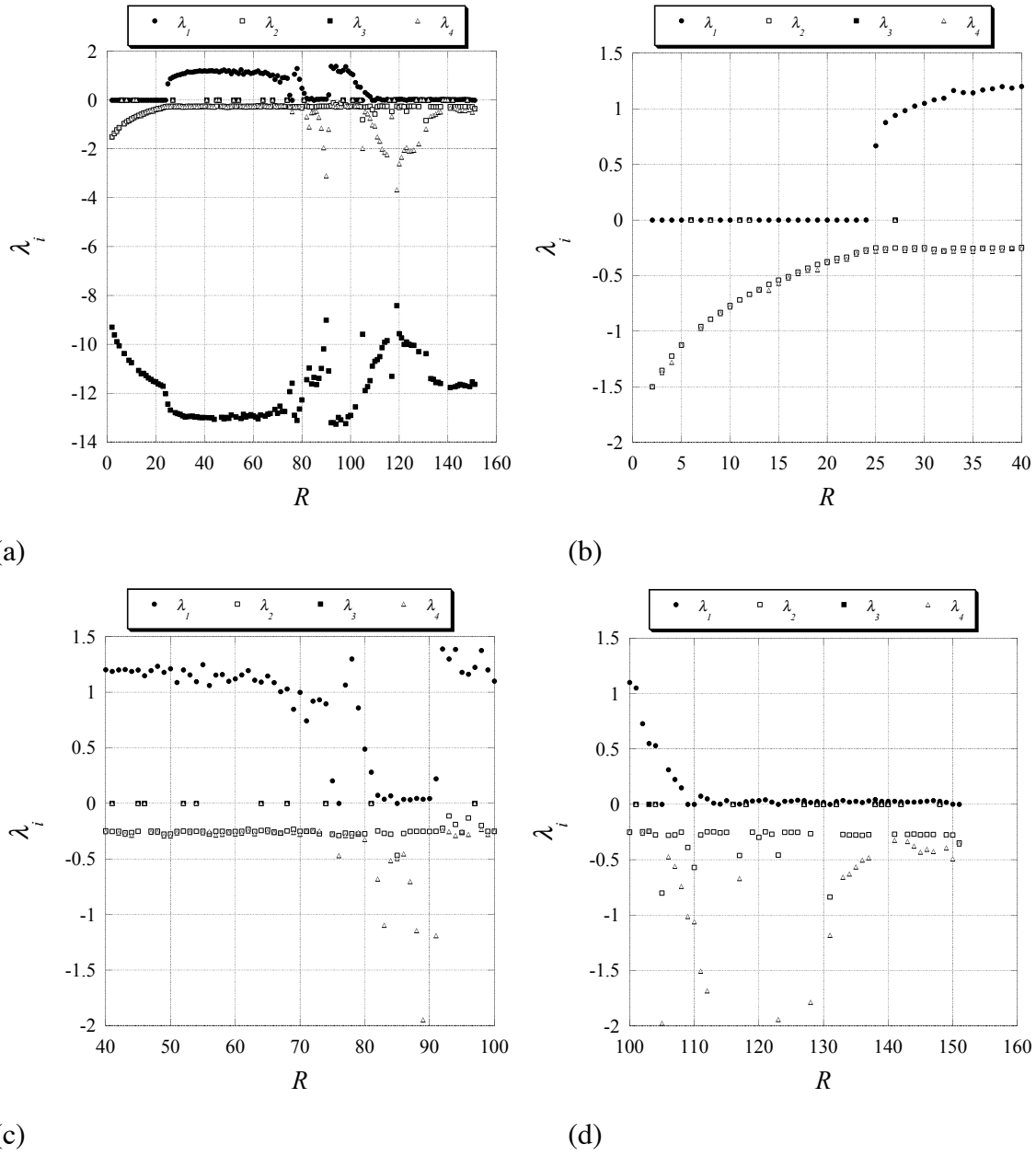

Figure 5.33: Graphical description of the Lyapunov exponents for $\omega = 100$.

© University of Pretoria

5.3 Results for the average heat flux in terms of the Nusselt number

The computed numerical results of the average Nusselt number by using the evaluation method presented in equation (85) is presented in this section. The resulting average values of Nusselt numbers are presented as a function of R for different values of forcing frequencies. In each graph, a reference curve corresponding to the Nusselt number obtained in the absence of vibrations is also presented in order to observe whether the vibrations have an enhancing, retarding or no effect on the resulting convection.

The results for the average Nusselt number corresponding to $\omega = 1$ are presented in Figure 5.34. It is evident from Figure 5.34 that at this small frequency, the vibrations substantially reduce the average heat flux over the whole range of scaled Rayleigh numbers considered. Therefore, this regime of small frequency vibrations may be desirable in cases where reduction of heat transfer (e.g. insulation) is needed. As the frequency of vibrations is increased to $\omega = 6.5$, as presented in Figure 5.35 the average heat flux is increased, but it is still lower than that without vibration initially. However, at an increased value of the scaled Rayleigh number, the average heat flux is increased above that without vibration. Therefore, under certain conditions where the scaled Rayleigh number is higher, this frequency of vibration may be used to increase the heat transfer.

Increasing the frequency to $\omega = 25.2$, as presented in Figure 5.36, shows how the average heat flux follows very closely to that without vibration up to a scaled Rayleigh number of about $R \approx 65$. Past this value, the average heat flux is increased above that without vibration.

The results presented in Figure 5.37 for a frequency of vibration $\omega = 46$ show the average heat flux is almost identical to that without vibration for the entire range of scaled Rayleigh numbers.

© University of Pretoria

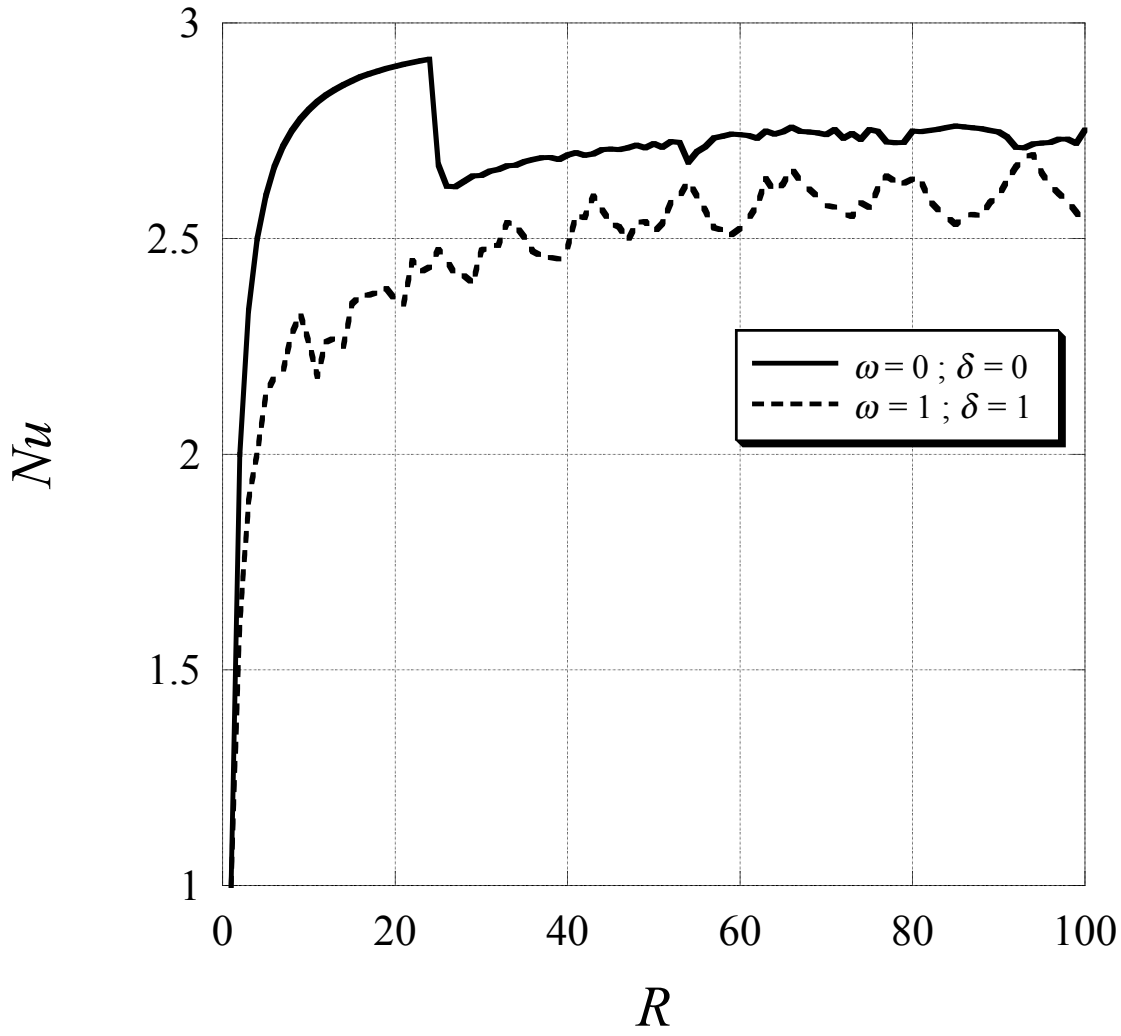

Figure 5.34: Graphical description of the average heat flux in terms of the Nusselt number for forced vibrations at a frequency of $\omega = 1$ (and forcing vibration amplitude $\delta = 1$) in comparison with the average heat flux in the absence of forced vibrations, i.e. $\omega = 0, \delta = 0$.

© University of Pretoria

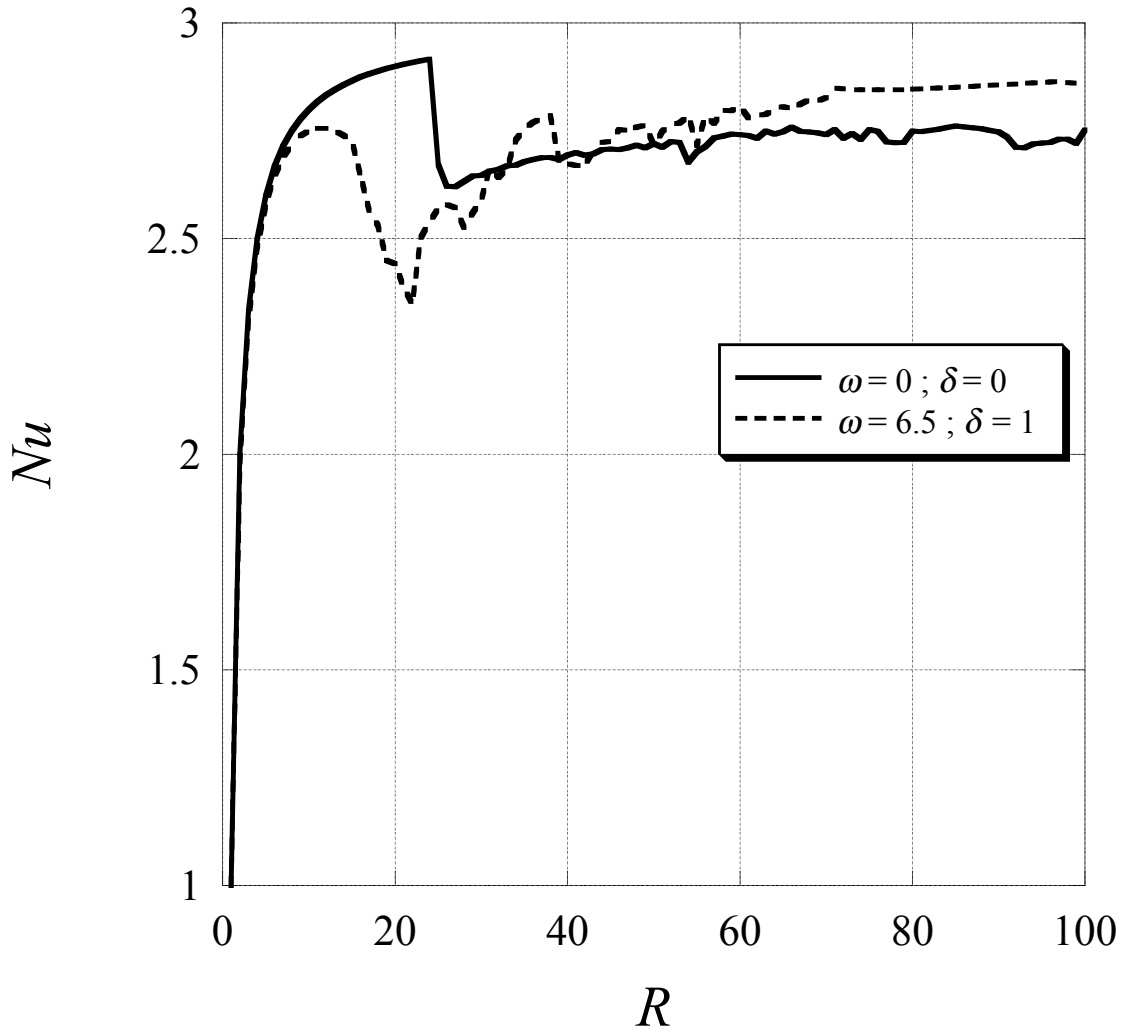

Figure 5.35: Graphical description of the average heat flux in terms of the Nusselt number for forced vibrations at a frequency of $\omega = 6.5$ (and forcing vibration amplitude $\delta = 1$) in comparison with the average heat flux in the absence of forced vibrations, i.e. $\omega = 0, \delta = 0$.

© University of Pretoria

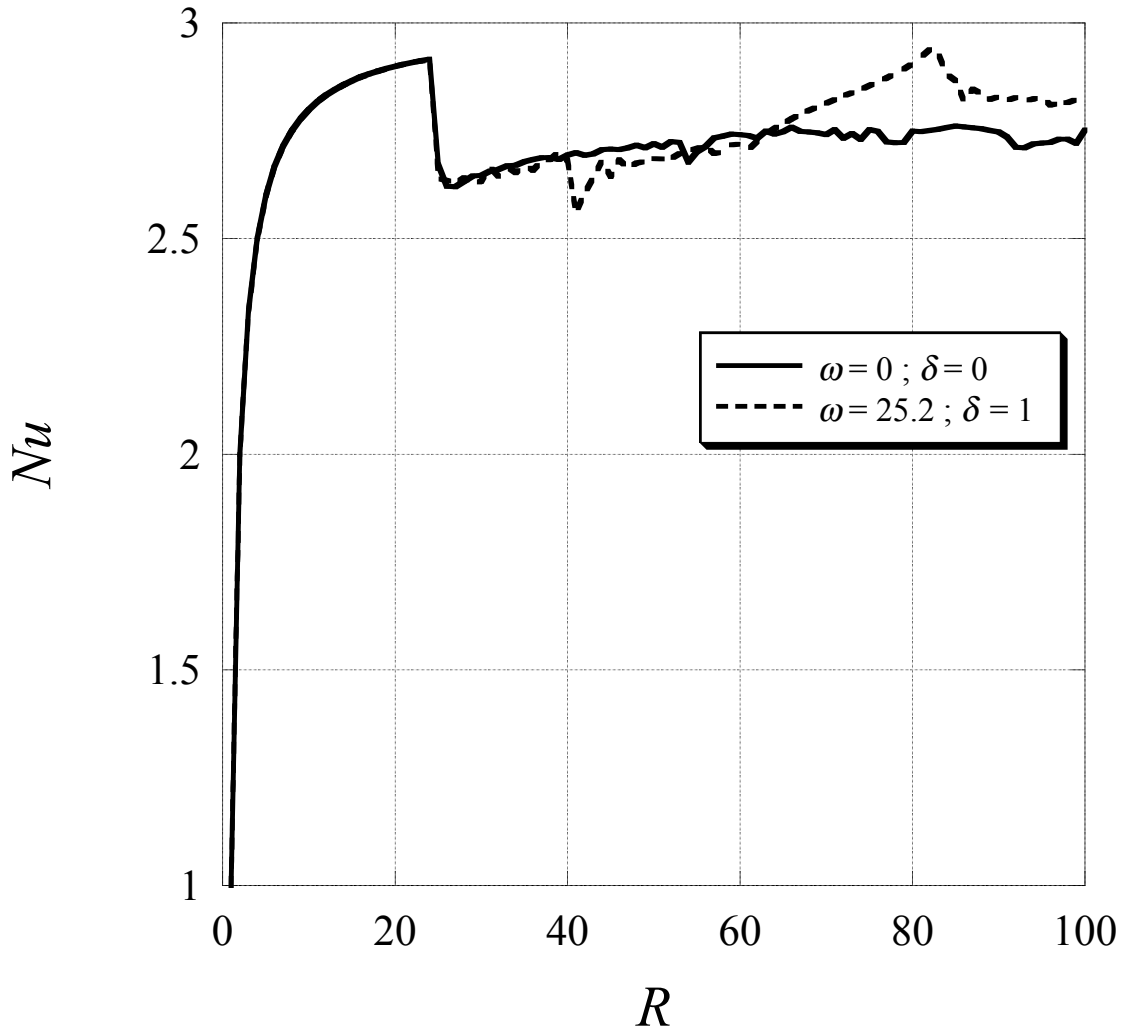

Figure 5.36: Graphical description of the average heat flux in terms of the Nusselt number for forced vibrations at a frequency of $\omega = 25.2$ (and forcing vibration amplitude $\delta = 1$) in comparison with the average heat flux in the absence of forced vibrations, i.e. $\omega = 0, \delta = 0$.

© University of Pretoria

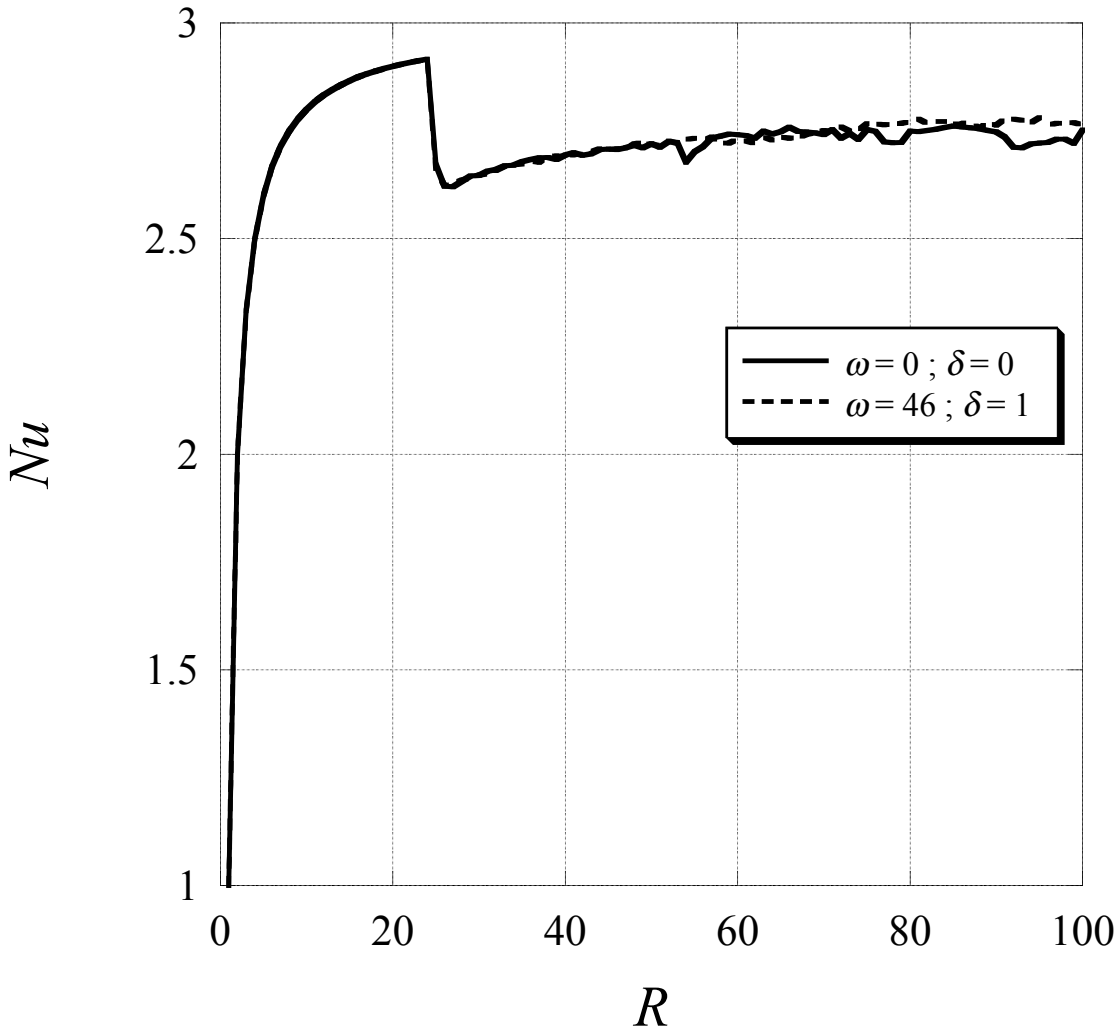

Figure 5.37: Graphical description of the average heat flux in terms of the Nusselt number for forced vibrations at a frequency of $\omega = 46$ (and forcing vibration amplitude $\delta = 1$) in comparison with the average heat flux in the absence of forced vibrations, i.e. $\omega = 0, \delta = 0$.

5.4 Summary

Periodic, quasi-periodic and chaotic results were presented as the outcome of the solution obtained at different values of the scaled Rayleigh number and different forcing frequency. Stationary solutions (fixed points) cannot be obtained when there are forced vibrations. The Lyapunov exponents were evaluated identifying accurately the distinction between periodic, quasi-periodic and chaotic orbits. Therefore the present chapter provides a map in the parameter domain in the form of the variation of the Lyapunov exponents with a change in the scaled Rayleigh number that can be used in the identification of the different dynamical regimes. Then focusing on such regimes

© University of Pretoria

indicate the possibility (or lack) of heat transfer enhancement. The average heat transfer was presented in terms of the average Nusselt number. For periodic regimes this represents the average over the period of oscillations, while for quasi-periodic and chaotic regimes it represents the average over a very large period of time. From the results it was observed that in the small frequency regime vibrations may be desirable in cases where reduction of heat transfer is required because vibrations substantially reduce the average heat flux over the whole range of scaled Rayleigh numbers considered. For large frequency vibrations on the other hand enhancement in heat transfer was obtained sparingly within the chaotic regime, however this enhancement is not as large compared to the non-vibrating convection as one would desire. This limited enhancement may be due to the fact that although resonances exist their corresponding effect on the amplitude of convection becomes reduced when averaging over a period of vibration or over a long period of time.

© University of Pretoria

CHAPTER 6

SUMMARY, CONCLUSIONS AND RECOMMEDATIONS

6.1 Summary

A larger rate of solid production was obtained experimentally in the solidification process of Paraffin subjected to vibrations confirming previous experimental results showing also substantially improved properties of the cast. In the present work void presence was reduced in addition to faster solidification, and consequently the mass of solid produced at a fixed time after starting the solidification process increases due to the imposed vibration. The extremely complex process of solidification and the corresponding variety of coupled mechanisms make the procedure of identifying the precise causes of such improvement extremely difficult. The only way for accomplishing the identification of these causes is to investigate the separate mechanisms first and possibly the interaction between them later, if needed. The theoretical part of the present work focused therefore on one such mechanism, namely the heat convection process in a porous layer subject to vibrations.

A model for the temporal dynamics of the natural convection heat transfer process in a vibrating porous layer was developed in order to investigate the possibility that thermal resonances alone might be the reason for the improved properties in solidification of binary alloys. The model consists of simplifying the governing partial differential equations for natural convection in a vibrating porous layer by using a set of sensible assumptions of two dimensional flow, convection in the form of longitudinal rolls, local thermal equilibrium between the solid and fluid phases in the porous layer, and truncating the spatial modes via a spectral method.

The result of this process lead to a set of four ordinary differential equations for the time variation of the stream function and temperature amplitudes. In addition, based on the developed model the evaluation of the average heat flux was undertaken by deriving an equation for the average Nusselt number. The average was accomplished over a period of oscillations if the solution was periodic, or over large time duration if the solution was quasi-periodic, or chaotic. The analysis and solution to these ordinary differential equations was then undertaken in order to identify convection regimes that can be anticipated to provide enhanced heat transfer. The first task in this process is in

© University of Pretoria

separating the different regimes of convection into periodic, quasi-periodic and chaotic and identifying the parameter window of values of the scaled Rayleigh number and forcing frequency where each of these regimes dominate. The stationary points are not a solution for the present problem of imposed vibrations and therefore a stationary convection regime is excluded. The solution was obtained numerically. For the sake of identification the numerical results were used to evaluate the Lyapunov exponents associated with each set of parameter values. The Lyapunov map in the parameter domain showed the regions of parameter values where periodic, quasi-periodic, or chaotic regimes dominate. A large number of results was obtained and presented in terms of the amplitudes as a function of time, or in terms of phase diagrams (phase portraits) and specifically plotting the projection of the trajectories in the different planes on the phase space. Subcritical periodic convection was obtained due to the imposed vibrations. This means that a periodic convective solution was obtained for values of the scaled Rayleigh number below the critical value associated with convection without vibrations. A transition towards a chaotic regime is then obtained as the scaled Rayleigh number increases. Within this generally chaotic regime windows of periodic and quasi-periodic solutions emerge. The effect of the different regimes on the heat transfer was then evaluated by using the results to calculate the corresponding average Nusselt number, based on the formula that was derived and discussed above. From the results it was observed that in the small frequency regime vibrations may be desirable in cases where reduction of heat transfer is required because vibrations substantially reduce the average heat flux over the whole range of scaled Rayleigh numbers considered. For large frequency vibrations on the other hand enhancement in heat transfer was obtained sparingly within the chaotic regime, however this enhancement is not as large as one would desire, when compared to the non-vibrating convection. This limited enhancement may be due to the fact that although resonances exist their corresponding effect on the amplitude of convection becomes reduced when averaging over a period of vibration or over a long period of time. Therefore, from the theoretical analysis and the results presented vibrations do not enhance the convection heat transfer in general for the parameter ranges considered. While some windows of parameter values where enhancement was observed probably due to nonlinear resonances exist the latter show enhancement within the weak turbulent (chaotic) regime of about 10% that is weaker than the corresponding value in the laminar pre-transition regime.

© University of Pretoria

6.2 Conclusions

It is evident from the literature survey as well as from the present study's experimental results that vibrations improve properties of the cast obtained from the solidification process. The very complex nature of the solidification process that includes a large number of phenomena linking fluid mechanics with heat and mass transfer processes with phase change and transport phenomena in multi-phase media makes it extremely difficult to single out one single process that is affected by vibrations. If such an isolation of the most significant process responsible for improvement of properties of the cast can be accomplished then it becomes possible to develop a consistent procedure to accomplish the latter.

The experimental results presented in Chapter 2 indicate that imposing vibrations causes indeed to a faster solidification, i.e. the mass produced at a fixed time after starting the solidification process increases due to the imposed vibrations. The two possible reasons for this experimental outcome were associated to the mass transfer process by which more nuclei of solid particles are created due to vibrations and they are more homogeneously distributed around the cooling front, or alternatively due to a more efficient convection process in the mushy layer causing possibly "thermal resonances" that might enhance the heat transfer and shorten the solidification time. The objective of this theoretical study was in investigating the second hypothesis, i.e. that the heat transfer enhancement via convection in the mushy layer occurred due to vibrations. Since, even the solidification process that includes coupled heat and mass transfer is also quite complex the approach adopted was in investigating the heat convection in a porous layer subject to vibrations and draw conclusions regarding the possibility of heat transfer enhancement.

A large number of computations were performed by varying the scaled Rayleigh number and the imposed frequency of vibration, and were presented in Chapter 5. A variety of convection regimes were identified, including periodic, quasi-periodic and chaotic (weak turbulent) and their corresponding dimensionless heat transfer coefficient expressed in

© University of Pretoria

terms of Nusselt number was evaluated.

From the theoretical analysis and the results presented it can be concluded that for the parameter ranges considered vibrations do not enhance the convection heat transfer in general. While some windows of parameter values where enhancement was observed probably due to nonlinear resonances exist the latter show enhancement within the weak turbulent (chaotic) regime of about 10% that is weaker than the corresponding value in the laminar pre-transition regime.

Therefore the mechanism of heat convection alone cannot be responsible for the properties improvements in solidification of binary alloys subject to vibrations. This implies that reason behind the substantially improved solidification is linked to the coupled heat and mass transfer process. However the coupled heat and mass transfer process involves also a complex combination of mechanisms. Among these mechanisms the one that seems more likely to have such a substantial impact on the solidification is the formation of freckles that depends strongly on the convection heat and mass transfer. The stronger the convection heat transfer the faster the formation of solid and the larger the convection mass transfer the more homogeneous the distribution of these freckles, and consequently the more homogeneous the distribution of voids. How will these mechanisms develop subject to vibration over a wide range of parameter values is not well known yet.

Therefore, the major conclusions from this study are that

(i) all anticipated regimes of natural convection were indeed obtained, including periodic, quasi-periodic, and chaotic (weak-turbulent) regimes.
(ii) the anticipated nonlinear thermal resonances do not affect substantially the average heat transfer by convection because the solutions seem to behave quite symmetrically around the average values and therefore the averaging process removes any such instantaneous large amplitude effects.

© University of Pretoria

(iii) the combined heat and mass transfer by convection is therefore the remaining reason for the improvement observed experimentally in the solidification process subject to vibrations.

(iv) with hindsight one may be able to anticipate that one of the mass transfer mechanisms, namely the freckles formation, and the consequent variation of solid fraction (or equivalently the porosity) is the probable cause for the improvement in the solidification process when subjected to vibrations. This mechanism is expected to depend strongly on convection heat transfer as well as convection mass transfer in the porous medium (mushy layer).

6.3 Recommendations for future work

Based on the conclusions presented in the previous section a clear course of action can be recommended in terms of follow-up studies having the objective of fully understanding the causes behind the experimentally established improvement of the properties of the cast in the solidification process. It seems that a combination of heat and mass transfer processes might provide the explanation for such improvement. Therefore a substantial further development of the model developed in the present study to include mass transfer is recommended as the next step. Such an extension should include the modeling of the freckles formation within the mushy layer by allowing the porosity (or consequently the solid fraction) within the mushy layer to vary in time as well as in space. Modeling this effect is not a simple task and it is for this reason that it was nowhere attempted before. While models of heat and mass transfer within a mushy layer were derived previously and were presented in the literature survey, they have the limitation of being applied for a very narrow range of thermal and solute Rayleigh numbers, i.e. very close to the critical values of these Rayleigh numbers, making the results and conclusions quite limited. On the other hand, other attempts focused on full numerical simulation which suffers from a too large parameter space, i.e. too large number of parameters and consequently a voluminous number of results and graphs that are difficult to analyse. Therefore, the model presented in this study is a trade-off between the too narrow parameter domain leading to restricted results and a too complex direct numerical simulation that provides results that are difficult to analyse and consequently difficult to use in drawing conclusions. Extending the model proposed in

© University of Pretoria

the present study to include mass transfer and particularly to model the variation of the porosity (or its equivalent solid fraction) in time as well as in space and consequently the freckles formation is a very challenging and possibly extremely time consuming task, but nevertheless it is needed as the next step recommended based on the present study conclusions.

© University of Pretoria

REFERENCES

Abramov, V., Abramov, O., Bulgakov, V. & Sommer, F. Solidification of aluminium alloys under ultrasonic irradiation using water-cooled resonator, *Materials Letters* **37** (1-2), 27-34, 1998.

Amberg, G. & Homsy, G.M. Nonlinear analysis of buoyant convection in binary solidification to channel formation, *J. Fluid Mechanics* **252**, 79-98, 1993.

Anderson, D.M. & Worster, M.G. Weakly nonlinear analysis of convection in mushy layers during solidification of binary alloys, *J. Fluid Mechanics* **302**, 307-331, 1995.

Anderson, D.M. & Worster, M.G. A new oscillatory instability in a mushy layer during the solidification of binary alloys, *J. Fluid Mechanics* **307**, 245-267, 1996.

Assis, E., Ziskind, G., Letan, R. Numerical and Experimental Study of Solidification in a Spherical Shell, *J. of Heat Transfer* **131** (2), 024502, 2008

Bardan, G. & Mojtabi, A. On the Horton-Rogers-Lapwood convective instability with vertical vibration: onset of convection, *Physics of Fluids* **12**, 2723-2731, 2000.

Cao, W.Z. & Poulikakos, D. Solidification of a binary mixture saturating a bed of glass spheres, *Convective Heat and Mass Transfer in Porous Media* (eds. S. Kakaç et al.), Kluwer Academic, Dordrecht, 725-772, 1991a.

Cao, W.Z. & Poulikakos, D. Freezing of a binary alloy saturating a packed bed of spheres, *AIAA J. Thermophysics* **5**, 46-53, 1991b.

Caram, R., Banan, M. & Wilcox, W.R. Directional solidification of Pb-Sn eutectic with vibration, *Journal of Crystal Growth* **114**, 249-254, 1991.

Charrier-Mojtabi, M.C., Elhajjar, B. & Mojtabi, A. Analytical and numerical stability analysis of Soret-driven convection in a horizontal porous layer, *Physics of Fluids* **19**, 124104/1-14, 2007.

Chen, C.F. & Chen, F. Experimental study of the directional solidification of aqueous ammonium chloride solution, *J. Fluid Mechanics* **227**, 567-586, 1991.

© University of Pretoria

Chen, F., Lu, J.W. & Yang, T.L. Convective instabilities in ammonium chloride solution directionally solidified from below, *J. Fluid Mechanics* **276**, 163-187, 1994.

Chirita, G., Stefanescu, I., Soares, D. & Silva, F.S. Influence of vibration on the solidification behaviour and tensile properties of an Al–18 wt%Si alloy, *Materials and Design* **30**, 1575-1580, 2009.

Choi, J. & Viskanta, R. Freezing of aqueous sodium chloride solution saturated packed bed from above, *ASME HTD* **206** (2), 159-166, 1992.

Choi, J. & Viskanta, R. Freezing of aqueous sodium chloride solution saturated packed bed from a vertical wall of a rectangular cavity, *International J. Heat Mass Transfer* **36**, 2805-2813, 1993.

Copey, S.M., Giamei, A.F., Johnson, S.M. & Hornbecker, M.F. The origin of freckles in unidirectional solidified castings, *Metallurgical Transactions* **1**, 2193-2204, 1970.

Elhajjar, B., Mojtabi, A. & Charrier-Mojtabi, M.C. Influence of vertical vibrations on the separation of a binary mixture in a horizontal porous layer heated from below, *International J. Heat Mass Transfer* **52**, 165-172, 2009.

Eskin, G.I. Influence of cavitation treatment of melts on the processes of nucleation and growth of crystals during solidification of ingots and castings from light alloys, *Ultrasonics Sonochemistry* **1** (1), S59-S63, 1994.

Fowler, A.C. The formation of freckles in binary alloys, *IMA J. Applied Mathematics*, **35**, 159-174, 1985.

Govender, S. On the linear stability of large Stefan number convection in rotating mushy layers for a new Darcy equation formulation, *Transport in Porous Media* **51**, 173-189, 2003.

Govender, S. Stability of convection in a gravity modulated porous layer heated from below, *Transport in Porous Media* **57**, 113-123, 2004.

Govender, S. Linear stability and convection in a gravity modulated porous layer heated from below: transition from synchronous to subharmonic solutions, *Transport in Porous Media* **59**, 227-238, 2005a.

© University of Pretoria

Govender, S. Destabilising a fluid saturated gravity modulated porous layer heated from above, *Transport in Porous Media* **59**, 215-225, 2005b.

Govender, S. Stability analysis of a porous layer heated from below and subjected to low frequency vibration: frozen time analysis, *Transport in Porous Media* **59**, 239-247, 2005c.

Govender, S. Weak non-linear analysis of convection in a gravity modulated porous layer, *Transport in Porous Media* **60**, 33-42, 2005d.

Govender, S. Stability of gravity driven convection in cylindrical porous layer subjected to vibration, *Transport in Porous Media* **63**, 489-502, 2006.

Govender, S. Natural convection in gravity-modulated porous layers, in *Emerging topics in heat and mass transfer in porous media - theory and applications of transport in porous media*, (P. Vadasz ed.), **Vol. 22**, 133-148, 2008, DOI: 10.1007/978-1-4020-8178-1_6.

Govender, S. Vadasz number influence on vibration in a rotating porous layer placed far away from the axis of rotation, *ASME Journal of Heat Transfer* **132**, 112601/1-5, 2010.

Govender, S. Stability of moderate Vadasz number solutal Convection in a cylindrical mushy layer subjected to vertical vibration, *Transport in Porous Media* **88**, 225-234, 2011.

Govender, S. & Vadasz, P. Moderate time scale linear stability of moderate Stefan number convection in rotating mushy layers, *Journal of Porous Media* **5** (2), 113-121, 2002a.

Govender, S. & Vadasz, P. Weak non-linear analysis of moderate Stefan number oscillatory convection in rotating mushy layers, *Transport in Porous Media* **48** (3), 353-372, 2002b.

Govender, S. & Vadasz, P. Weak non-linear analysis of moderate Stefan number stationary convection in rotating mushy layers, *Transport in Porous Media* **49** (3), 247-263, 2002c.

© University of Pretoria

Gresho, P.M. & Sani, R.L. The effects of gravity modulation on the stability of a heated fluid layer, *J. Fluid Mechanics* **40**, 783-806, 1970.

Hull, T. E., Enright, W. H., & Jackson, K. R. User's Guide for DVERK: a subroutine for solving non-stiff ODE's, Rept.100, Department of Computer Science, University of Toronto, Canada, 1976.

Jian, X., Xu, H., Meek, T.T. & Han, Q. Effect of power ultrasound on solidification of aluminum A356 alloy, *Materials Letters* **59**, 190-193, 2005.

Jounet, A. & Bardan, G. Onset of thermohaline convection in a rectangular porous cavity in the presence of vertical vibration, *Physics of Fluids* **13** (11), 3234-3246, 2001.

Li, M., Tamura, T. & Miwa, K. Controlling microstructures of AZ31 magnesium alloys by an electromagnetic vibration technique during solidification: from experimental observation to theoretical understanding, *Acta Materialia* **55**, 4635-4643, 2007.

Lorenz, E.N. Deterministic non-periodic flows, *J. Atmospheric Sciences* **20**, 130-141, 1963.

Magyari, E. The "Butterfly Effect" in a porous slab, *Transport in Porous Media* **84** (3), 711-715, 2010a.

Magyari, E. The Vadasz-Olek model regarded as a system of coupled oscillators, *Transport in Porous Media* **85** (2), 415-435, 2010b.

Mahmud, M.N. & Hashim, I. Small and moderate Prandtl number chaotic convection in porous media in the presence of feedback control, *Transport in Porous Media* **84** (2), 432-440, 2010.

Mahmud, M.N. & Hashim, I. Small and moderate Vadasz number chaotic convection in porous media in the presence of non-Boussinesq effects and feedback control, *Physics Letters A* **375**, 2382-2393, 2011.

Matsumoto, K., Okada, M., Murakami, M. & Yabushita, Y. Solidification of porous medium saturated with aqueous solution in a rectangular cell, *International J. Heat Mass Transfer* **36**, 2869-2880, 1993.

© University of Pretoria

Matsumoto, K., Okada, M., Murakami, M. & Yabushita, Y. Solidification of porous medium saturated with aqueous solution in a rectangular cell - II, *International J. Heat Mass Transfer* **38**, 2935-2943, 1995.

Mazumder, P., Trivedi, R., & Karma, A. A Model of Convection-Induced Oscillatory Structure Formation in Peritectic Alloys, *Metallurgical and Materials Transactions A* **31A**, 1233-1246, 2000.

Mladin, E.C., & Zumbrunnen, D.A. Dependence of Heat Transfer to a Pulsating Stagnation Flow on Pulse Characteristics, *Journal of Thermophysics and Heat Transfer* **9** (1), 181-192, 1995.

Moran M. J., Shapiro H. N., Boettner D. D., Bailey M. B., Fundamentals of Engineering Thermodynamics 7th edition, John Wiley& Sons, Inc., 2011.

Nield, D.A. & Bejan, A. *Convection in porous media*, 3rd Edition, Springer, 2006.

Pillay, S.K. & Govender, S. Stability of solutal convection in a gravity modulated mushy layer during the solidification of binary alloys, *Transport in Porous Media* **60**, 183-197, 2005.

Roslan, R., Mahmud, M.N. & Hashim, I. Effects of feedback control on chaotic convection in fluid-saturated porous media, *International J. Heat Mass Transfer* **54** (1-3), 404-412, 2011.

Song, M., Choi, J. & Viskanta, R. Upward solidification of a binary solution saturated porous medium, *International J. Heat Mass Transfer* **36**, 3687-3695, 1993.

Sparrow, C. *The Lorenz equations: bifurcations, chaos, and strange attractors*, Springer-Verlag, New York, 1982.

Tait, S. & Jaupart, C. Compositional convection in a reactive crystalline mush and melt differentiation. *J. Geophysical Research* **97** (B5), 6735-6756, 1992.

Vadasz, P. Coriolis effect on gravity-driven convection in a rotating porous layer heated from below, *J. Fluid Mechanics* **376**, 351-375, 1998.

© University of Pretoria

Vadasz, P. Local and global transitions to chaos and hysteresis in a porous layer heated from below, *Transport in Porous Media* **37** (2), 213-245, 1999a.

Vadasz, P. Subcritical transitions to chaos and hysteresis in a fluid layer heated from below, *International Journal of Heat and Mass Transfer* **43** (5), 705-724, 1999b.

Vadasz, P. Heat transfer regimes and hysteresis in porous media convection, *ASME Journal of Heat Transfer* **123**, 145-156, 2001.

Vadasz, P. Controlling chaos in porous media convection by using feedback control, *Transport in Porous Media* **85** (1), 287-298, 2010.

Vadasz, P. & Olek, S. Weak turbulence and chaos for low Prandtl number gravity driven convection in porous media, *Transport in Porous Media* **37** (1), 69-91, 1999.

Vadasz, P. & Olek, S. Route to chaos for moderate Prandtl number convection in a porous layer heated from below, *Transport in Porous Media* **41** (2), 211-239, 2000.

Vafai, K., & Hadim, H. Overview of current computational studies of heat transfer in porous media and their applications – natural and mixed convection, Ch. 10, in *Advances in Numerical Heat Transfer* (Minkowycz, W.J. Sparrow, E.M. eds.), **Vol. 2**, Taylor & Francis, New York, 2000.

Wadih, M. & Roux, B. Natural convection in a long vertical cylinder under gravity modulation, *J. Fluid Mechanics* **193**, 391-415, 1988.

© University of Pretoria